January 2021

Therapeutic Dual-Targeting Of Cytosolic And Mitochondrial One-Carbon Metabolism

Aamod Sanjeev Dekhne
Wayne State University, adekhne@gmail.com

THERAPEUTIC DUAL-TARGETING OF CYTOSOLIC AND MITOCHONDRIAL ONE-CARBON METABOLISM

by

AAMOD SANJEEV DEKHNE

DISSERTATION

Submitted to the Graduate School

of Wayne State University,

Detroit, Michigan

in partial fulfillment of the requirements

for the degree of

DOCTOR OF PHILOSOPHY

2019

MAJOR: CANCER BIOLOGY

Approved By:

_____

Advisor Date

_____

_____

_____

_____

DEDICATION

This dissertation is dedicated to John and Mary Lulz. They are my inspiration for this work.

ACKNOWLEDGEMENTS

I would like to thank my mentor, Dr. Larry Matherly, for taking me in off the street in 2014 and guiding my development as a scientist. In the last 5 years, I have learned through trial and error (lots of error) that nothing is ever rocket science and experiments can be done passively. I am especially grateful for, he knows what I'm going to say, his incredible drop-in availability to discuss my science despite the many hats that he wears. But most of all, I am indebted to him for sacrificing himself to keep me dry on a tempestuous night in the mountains of Taormina.

I would like to thank my collaborators (and their students/research assistants): Dr. Aleem Gangjee (Khushbu Shah and Md. Junayed Nayeen) for synthesizing the most rationally and empirically designed pyrrolo[3,2-*d*]pyrimidines for my studies, Dr. Maik Hüttemann (Hasini Kalpage and Jenney Liu) for interrogating every means of oxygen consumption under the sun, Dr. Lisa Polin (Juiwanna Kushner and Kathryn White) for taking the best possible care of our mice survivors, Dr. Seongho Kim for dealing with all of my dynamite plots, Dr. Greg Ducker for processing all of my metabolomics extracts and generating exceptional diagrams, Dr. Jing Li (Xun Bao) for teaching me the nuances of different LC-MS instrumentation, and Dr. Izabela Podgorski (Mackenzie Herroon and Erandi Rajagurubandara) for allowing me to live rent-free in her hypoxia chamber room for 6 months. Oh, and Dr. Charles Dann III (Jennifer Wong and Jade Katinas) for making sure I learned how to assay SHMT *in vitro*.

A special thanks to the members of the Matherly Lab for helping me keep my project on track: Dr. Zhanjun Hou, for being my guiding beacon in experimental techniques. Knee-deep in experiments, I would always ask myself , "What would Zhanjun do?", and instantly, I would know the best method for any given situation. Carrie O'Connor, for enabling me to buy the best

Secret Santa presents and teaching me how to run Western Blots. Without her, I would have had no one to quote “Officespace” to, and lab life would have been dreadful indeed. I forgive her constant singing. Adrianne Wallace-Povirk, for her empathy as we have progressed on our grad student journey together. From commiserating about grad school classes and fellowship grants, to always reminding me to remain thankful I did not have Tet-On in my project, Adrianne’s advice has always been welcome. Changwen Ning, for running most of the Western Blots that counted and for always reminding me to smile. And Nadia Daniel, for her immeasurable help in negotiating the administrative obstacle course at Wayne State University.

On the MD/PhD side, I want to thank Deanna Doña for always knowing and revealing the next step of the journey. Without her administrative acumen in particular, I am certain the med school would have Wayned me into oblivion. Also, I want to thank Dr. Dan Walz for his unwavering belief in my progress towards my degrees and for helping keep the med school accredited for just a while longer.

Finally, I would like to thank my funding, T32 CA009531 and F30 CA228221 from the NCI, without which I would not have been able to sleep easy on Tuesday nights.

TABLE OF CONTENTS

LIST OF TABLES

LIST OF FIGURES

LIST OF ABBREVIATIONS

3PG	3-phosphoglycerate
3PS	3-phosphoserine
3PHP	3-phosphohydroxypyruvate
5,10-meTHF	5,10-methyleneTHF
5-FU	5-fluorouracil
6-MP	6-mercaptopurine
AICA	5-aminoimidazole-4-carboxamide
AICAR	AICA ribonucleotide
AICARFTase	AICAR formyltransferase
ALDH1L2	aldehyde dehydrogenase 1 family member L2
ALL	acute lymphoblastic leukemia
αMEM	α-minimal essential medium
AML	acute myeloid leukemia
AMPK	AMP-activated kinase
ATIC	AICARFTase/IMP cyclohydrolase
β-Me	β-mercaptoethanol
C1	one-carbon
CHO	Chinese hamster ovary
DCPIP	2,6-dichlorophenolindophenol
DHF	dihydrofolate
DHFR	dihydrofolate reductase
EC_{50}	half-maximal effective concentration

FCCP	carbonyl cyanide-4-(trifluoromethoxy)phenylhydrazone
FLT3-ITD	FMS-like tyrosine kinase 3 internal tandem duplication
FPGS	folylpoly-γ-glutamate synthetase
FR	folate receptors
FRα/β/γ	folate receptor alpha/beta/gamma
GAPDH	glyceraldehyde-3-phosphate dehydrogenase
GAR	glycinamide ribonucleotide
GARFTase	glycinamide ribonucleotide formyltransferase
GPI	glycosyl phosphatidylinositol
GSH	glutathione
GSSG	glutathione disulfide
Hcy	homocysteine
HEPES	4-(2-hydroxyethyl)-1-piperazineethanesulfonic acid
HPLC	high performance liquid chromatography
IC	IMP cyclohydrolase
IMP	inosine monophosphate
IPTG	β-D-1-thiogalactopyranoside
IV	intravenously
KD	knockdown
KO	knockout
LC-MS	liquid chromatography - mass spectrometry
LDH	lactate dehydrogenase
LMX	lometrexol

MES	2-(N-morpholino)ethanesulfonic acid
MFS	Major Facilitator Superfamily
MFT	Mitochondrial folate transporter
MS	mannitol-sucrose
MTAP	methylthioadenosine phosphorylase
MTD	maximum tolerated dose
MTHFD	methyleneTHF dehydrogenase
MTHFD1L/2L	MTHFD1-like/2-like
MTHFR	methyleneTHF reductase
mTOR	mammalian target of rapamycin
MTR	methionine synthetase
MTX	methotrexate
NTC	non-targeted shRNA-transduced control
OCR	oxygen consumption rate
PBS	Dulbecco’s phosphate-buffered saline
PCFT	proton-coupled folate transporter
PHGDH	phosphoglycerate dehydrogenase
PKM2	pyruvate kinase isoform M2
PLP	pyridoxal 5'-phosphate
PMX	Pemetrexed
PRPP	phosphoribosyl pyrophosphate
PSAT1	phosphoserine aminotransferase1
PSPH	phosphoserine phosphatase

PTX	pralatrexate
QDPR	quinoid dihydropteridine reductase
Raptor	regulatory associated protein of mTOR
RFC	reduced folate carrier
ROS	reactive oxygen species
RSB	resuspension buffer
RT-PCR	reverse transcriptase polymerase chain reaction
RTX	raltitrexed
SAMe	S-adenosylnmethionine
SCID	severe combined immunodeficient
SDH	succinate dehydrogenase
SHIN1	serine hydroxymethyltransferase inhibitor 1
SHMT	serine hydroxymethyltransferase
shRNA	small hairpin RNA
SLC	solute carrier
SUMO	small ubiquitin-like modifier
THF	tetrahydrofolate
TS/TYMS	thymidylate synthase
UHPLC	ultra-high performance liquid chromatograph
WT	wild-type

CHAPTER 1- INTRODUCTION

1.1 One-Carbon Metabolism

One-carbon (C1) metabolism encompasses a series of anabolic reactions that transfer species containing a single carbon atom (i.e. "C1" units). The enzymes catalyzing these reactions are mediated by folate cofactors (i.e. vitamin B9 family members) and serve multiple foundational cellular roles including generation of nucleotides for DNA and RNA synthesis, preservation of amino acid homeostasis, and maintenance of redox balance (Ducker and Rabinowitz, 2017). These reactions are compartmentalized primarily into the mitochondria and the cytosol (Tibbetts and Appling, 2010) (**Figure 1.1**) with a minor pool in the nucleus (Field et al., 2018). Ultimately, the grand majority of C1 units in most cancer cells is derived from serine catabolism in the mitochondria in the form of formate (Labuschagne et al., 2014). Formate then enters the cytosol and is attached to the reduced folate cofactor tetrahydrofolate (THF) to produce activated C1 units such as 10-formylTHF and 5,10-methyleneTHF (5,10-meTHF), which ultimately transfer the C1 unit to intermediates in *de novo* purine biosynthesis and thymidylate biosynthesis, respectively (Appling, 1991). While the reactions in each compartment are generally reversible, the directionality of each pathway is driven by the differing expression of the enzymes in different tissues (Girgis et al., 1998), the NAD(P)H/NAD(P)$^+$ ratios in the cytosol (high) and mitochondria (low) which drive the methyleneTHF dehydrogenase (MTHFD) reaction in opposite directions (Ducker et al., 2016), and the availability of folate cofactors such as 10-formylTHF in the cytosol which can reverse the serine hydroxymethyltransferase(SHMT)1 and MTHFD1 reactions to meet demand (Ducker et al., 2016).

1.1.1 Cytosolic One-Carbon Metabolism

Net outputs of cytosolic C1 metabolism primarily include thymidylate, purines,

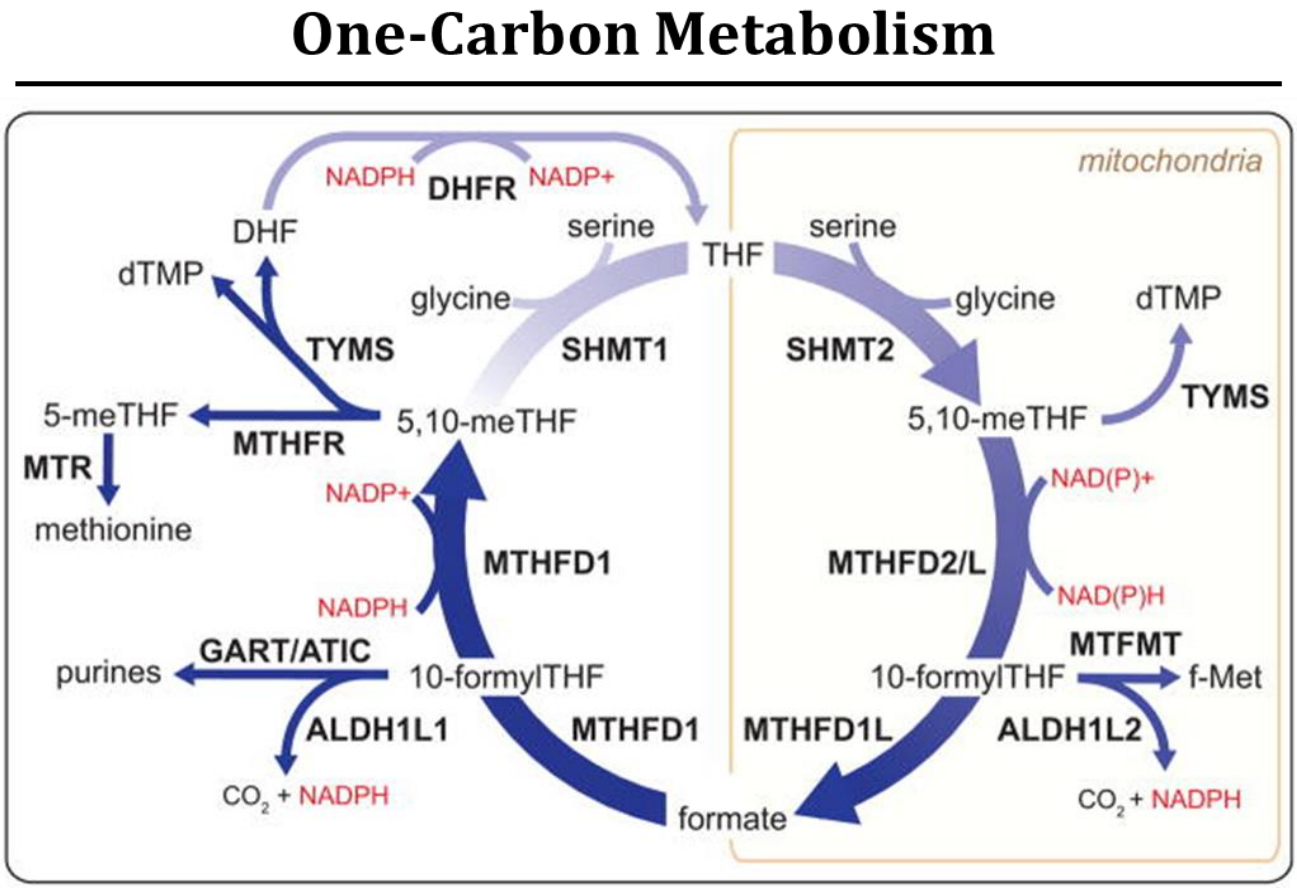

Figure 1.1 Overview of One-Carbon Metabolism. One-carbon metabolism is compartmentalized primarily into the mitochondria and cytosol. Mitochondrial enzymes include serine hydroxymethyltransferase2 (SHMT2), methyleneTHF dehydrogenase 2/2-like (MTHFD2/L), MTHFD1L, aldehyde dehydrogenase 1 family member L2 (ALDH1L2), methionyl-tRNA-formyltransferase (MTFMT), and thymidylate synthase (TYMS or TS). Cytosolic enzymes include MTHFD1, ALDH1L1, TYMS, the purine biosynthetis enzymes glycinamide ribonucleotide formyltransferase (GART or GARFTase) and 5-aminoimidazole-4-carboxamide ribonucleotide formyltransferase/inosine monophosphate cyclohydrolase (ATIC – AICARFTase/IMP cyclohydrolase), methyleneTHF reductase (MTHFR), TYMS, dihydrofolate reductase (DHFR), and methionine synthase (MTR). Adapted from (Ducker and Rabinowitz, 2017)

methionine, and serine (**Figure 1.1**). In the cytosol, thymidylate can be salvaged from thymidine via phosphorylation by thymidine kinase (Munch-Petersen et al., 1995), or can be formed *de novo* from dUMP by the direct action of the folate-dependent enzyme thymidylate synthase (TYMS or TS) (Newman and Maddocks, 2017). The specific folate cofactor, 5,10-meTHF, is generated in the cytosol from formate by MTHFD1 (Field et al., 2016) and is converted into dihydrofolate (DHF) in the TS reaction. Dihydrofolate reductase (DHFR) then regenerates the reduced active form THF from DHF by oxidizing NADPH into $NADP^+$ (Ducker and Rabinowitz, 2017). Indeed, TS and DHFR are likely to "substrate channel" by binding together to essentially generate a bifunctional enzyme complex (Wang and McCammon, 2016). Thymidylate synthesis also takes place in the nuclear and mitochondrial compartments to prevent uracil misincorporation into DNA by generating sufficient dTMP for DNA replication (Anderson et al., 2011; Field et al., 2018).

De novo purine biosynthesis, however, is a 10-step process that takes place exclusively in the cytosol (**Figure 1.2**). To facilitate efficient metabolic flux, these enzymes assemble into a transient structure known as a purinosome (Pedley and Benkovic, 2017), which sequesters pathway intermediates and colocalizes with mitochondria to provide the 5 moles of ATP necessary to generate 1 mole of inosine monophosphate (IMP) *de novo*. Of these enzymes, two require folate cofactors, glycinamide ribonucleotide (GAR) formyltransferase (GARFTase) and 5-aminoimidazole-4-carboxamide ribonucleotide (AICAR) formyltransferase (AICARFTase) (Mitchell-Ryan et al., 2013). The latter enzyme is part of the bifunctional enzyme complex AICARFTase/IMP cyclohydrolase (ATIC) which also catalyzes the last step in *de novo* purine biosynthesis to generate IMP. Surprisingly, the presence of both AICARFTase and IMP cyclohydrolase (IC) activities on one ATIC protein does not enable substrate channeling as seen

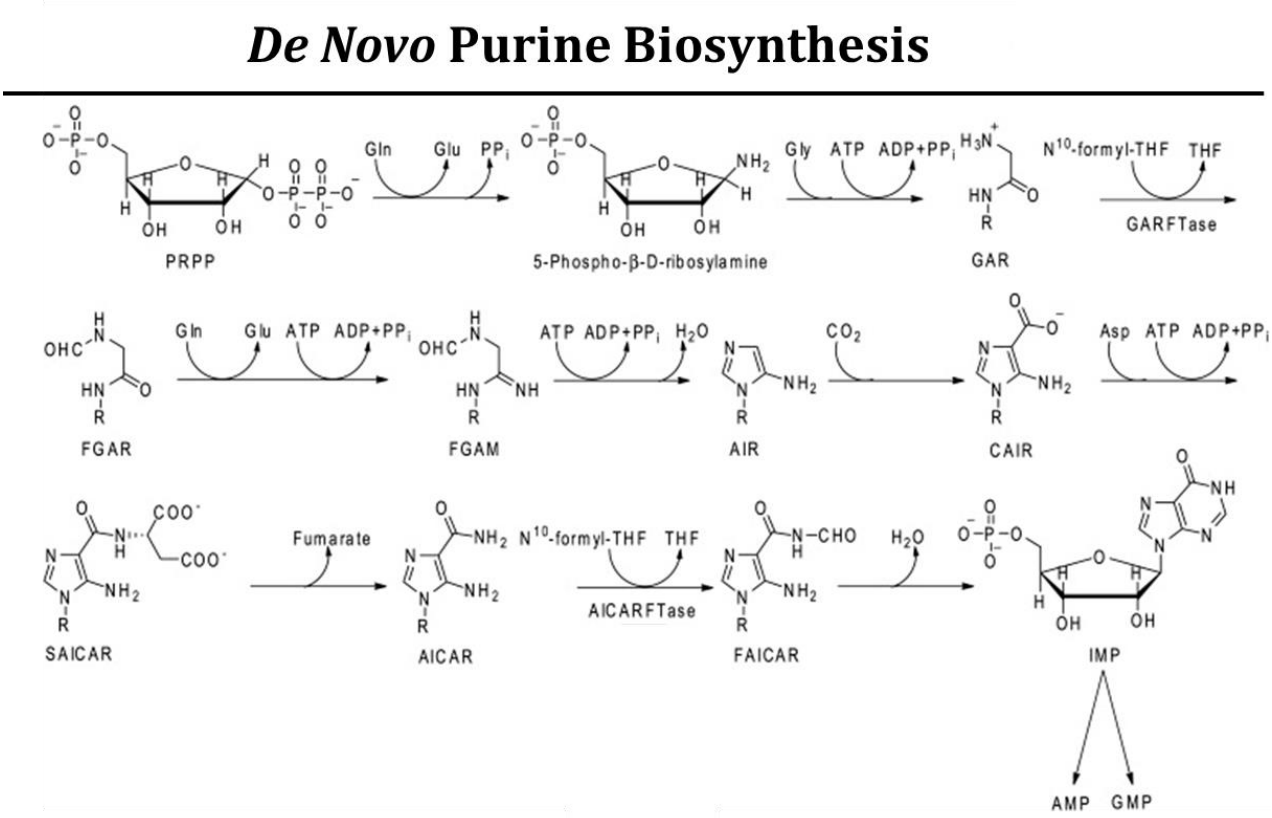

Figure 1.2 *De Novo* Purine Biosynthesis. The 10-step *de novo* purine biosynthesis pathway from phosphoribosyl pyrophosphate (PRPP) to inosine monophosphate (IMP) is shown above. Folate-dependent enzymes include glycinamide ribonucleotide formyltransferase (GARFTase) and 5-aminoimidazole-4-carboxamide formyltransferase (AICARFTase). Intermediates include GAR, formyl-GAR (FGAR), N-formylglycinamide ribonucleotide (FGAM), aminoimidazole ribonucleotide (AIR), carboxy-AIR (CAIR), 5-aminoimidazole-4-(N-succinylcarboxamide) (SAICAR), AICAR, and formyl-AICAR (FAICAR). Adapted from (Matherly et al., 2014)

with TS and DHFR (Bulock et al., 2002). Rather, ATIC combines the energetically unfavorable formylation of AICAR with the highly favorable cyclization reaction to make the overall reaction favorable (Wall et al., 2000). Like GARFTase, AICARFTase requires 10-formyl THF as a cofactor (Ducker and Rabinowitz, 2017), which, like 5,10-meTHF, is also generated in the cytosol from formate by MTHFD1 (Field et al., 2016). Additionally, purine nucleotides can also be salvaged from purine bases by adenine phosphoribosyltransferase or hypoxanthine-guanine phosphoribosyltransferase (Bertino et al., 2011).

In addition to nucleotide biosynthesis, cytosolic C1 metabolism also includes the methionine cycle, in which methionine is converted by methionine adenosyltransferase into S-adenosylmethionine (SAMe) (Miller, 2003). SAMe is a critical methyl donor playing a vital role in stabilizing both proteins and DNA, as well as in hepatic phase II detoxification (Miller, 2003). However, after donating its methyl group, SAMe becomes S-adenosylhomocysteine, which is consequently hydrolyzed into adenosine and the toxic amino acid intermediate homocysteine (Hcy) (Miller, 2003). Hcy then accepts a methyl group from 5-methylTHF (derived from 5,10-meTHF by methyleneTHF reductase (MTHFR) (Levin and Varga, 2016)) to generate methionine in a reaction catalyzed by the vitamin B12-dependent enzyme methionine synthetase (MTR) (Miller, 2003) **(Figure 1.1)**. The flux of cytosolic 5,10-meTHF into either the methionine cycle or thymidylate synthesis is controlled by SHMT1, a pyridoxal 5'-phosphate- (PLP) dependent (Renwick et al., 1998) enzyme distinct from although 66% homologous to the mitochondrial isoform SHMT2. SHMT1 primarily catalyzes the glycine-to-serine reaction, regenerating THF from 5,10-meTHF.

1.1.2 Nuclear One-Carbon Metabolism

While the thymidylate biosynthetic enzyme TS is found in the cytosol during all stages of

the cell cycle, it is only active during S-phase when it translocates (**Figure 1.3**) into the nucleus (Prem veer Reddy, 1982). TS, in addition to SHMT1, MTHFD1, and DHFR, undergo posttranslational covalent small ubiquitin-like modifier (SUMO) modification and translate to the nucleus at the onset of S-phase where they, along with SHMT2α (an SHMT2 isoform lacking the mitochondrial targeting sequence), associate with DNA repair/replication machinery (including DNA polymerases) to form the replitase complex (Murthy and Reddy, 2006). The replitase functions to synthesize DNA for repair or replication while concurrently generating thymidylate to limit uracil misincorporation (Field et al., 2018). Interestingly, both SHMT1 and SHMT2α are thought to act predominantly as non-catalytic scaffold proteins that are essential for formation of the replitase complex, meaning the actual 5,10-meTHF required for thymidylate biosynthesis is likely provided by formate flux through MTHFD1 (Anderson et al., 2012). However, the importance of SHMT1 catalytic activity in the nucleus remains controversial (Giardina et al., 2018).

1.1.3 Mitochondrial One-Carbon Metabolism

The formylTHF and methylTHF cofactors used in cytosolic and nuclear C1 metabolism are generated primarily from mitochondrially-derived formate (Ducker and Rabinowitz, 2017). In the mitochondria, serine donates a methyl group to THF to generate glycine and 5,10-meTHF in a reaction catalyzed by SHMT2. 5,10-meTHF is then converted into 10-formylTHF by MTHFD2 or MTHFD2L with the former expressed only in transformed and embryonic or undifferentiated adult cells and the latter expressed in adult normal cells (Shin et al., 2017). 10-formylTHF is then converted into formate by MTHFD1-like (MTHFD1L) and exported into the cytosol where it is the primary source of C1units for cytosolic C1 metabolism (Ducker et al., 2016; Ducker and Rabinowitz, 2017). Moreover, formate is produced in excess of cytosolic C1

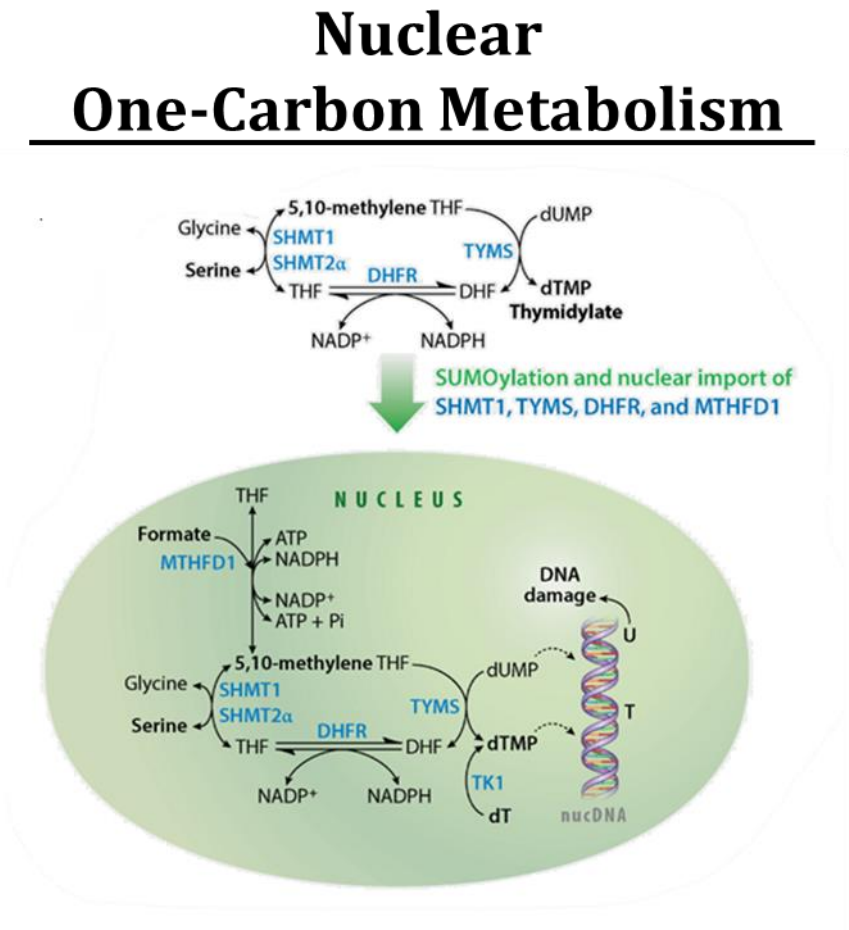

Figure 1.3 Nuclear One-Carbon Metabolism. Enzymes involved in thymidylate biosynthesis, including serine hydroxymethyltransferase1 (SHMT1), thymidylate synthase (TYMS or TS), dihydrofolate reductase (DHFR), and methyleneTHF dehydrogenase1 (MTHFD1) are modified by small ubiquitin-like modifier (SUMO) ligases and translocate into the nucleus at the onset of S-phase, where they provide dTMP locally to prevent uracil misincorporation into DNA. Adapted from (Field et al., 2018)

metabolism need by the mitochondria (Ducker et al., 2016) as formate depletion leads to accumulation and consequent degradation of cytosolic THF due to insufficient activity of the tetrahydrobiopterin metabolism enzyme quinoid dihydropteridine reductase (QDPR), which moonlights to repair oxidative damage to THF (Zheng et al., 2018). While the dehydrogenase (MTHFD2/MTHFD2L), cyclohydrolase (MTHFD2/MTHFD2L), and 10-formyl-synthetase (MTHFD1L) activities are performed by different enzymes in the mitochondria, all three are performed by the trifunctional MTHFD1 in the cytosol (Gustafsson et al., 2017).

Beyond their roles in C1 metabolism, these enzymes and intermediates also play critical roles in "non C1" pathways as well. For instance, MTHFD2, along with aldehyde dehydrogenase 1 family member L2 (ALDH1L2), generates NAD(P)H, critical for resistance to oxidative stress (Fan et al., 2014; Shin et al., 2017). Perturbation of the cellular NADPH/$NADP^+$ ratio due to loss of the mitochondrial C1 pathway, particularly under hypoxia, has been shown (Ye et al., 2014) to increase cell death and is rescuable by N-acetylcysteine, confirming the importance of this pathway to maintaining redox balance. In fact, NADPH production by cytosolic and mitochondrial MTHFD isoforms contributes to roughly 40% of total cellular NADPH production from glucose, with the remaining 60% primarily from the pentose phosphate pathway and malic acid enzyme (Fan et al., 2014). Moreover, high energy electrons from NADH drive 75% of oxidative phosphorylation and NADH production by MTHFD2 generates 7% of total mitochondrial NADH (Ducker et al., 2016) (with the remainder primarily generated by the Krebs cycle and cytosolic import (Fan et al., 2013)).

Additionally, the 10-formylTHF and 5,10-meTHF synthesized by MTHFD2 and SHMT2 respectively (**Figure 1.1**), play critical roles in local translation of mitochondrial proteins (Minton et al., 2018; Morscher et al., 2018). 10-formylTHF is required for generating N-

formylmethionine-tRNAs which are required for initiation of translation of mitochondrially-translated proteins (Tucker et al., 2011) whereas 5,10-meTHF is necessary for producing the taurinomethyluridine base on certain tRNAs critical for translation of electron transport chain enzymes (Morscher et al., 2018). Thus, mitochondrial C1 metabolism plays several critical roles in cellular survival and propagation.

1.1.4 Serine Biosynthesis

As most cancer cells preferentially utilize C1 units generated by the mitochondrial C1 pathway (Ducker et al., 2016), serine is the primary C1 unit donor in most cancer cells. Serine itself can be derived through glycolytic flux (**Figure 1.4**). The glycolytic intermediate 3-phosphoglycerate (3PG) can be shunted toward serine biosynthesis via the enzyme phosphoglycerate dehydrogenase (PHGDH), which is the first committed step in this process and converts 3PG into 3-phosphohydroxypyruvate (3PHP) (Amelio et al., 2014). 3PHP is then transaminated by phosphoserine aminotransferase1 (PSAT1) into 3-phosphoserine (3PS), which is subsequently converted into serine by phosphate ester hydrolysis via phosphoserine phosphatase (PSPH) (Amelio et al., 2014). Direction of the glycolytic flux towards either pyruvate or serine biosynthesis is mediated through allosteric activation of PHGDH by 2PG (driving flux towards serine when pyruvate is plentiful). This, in turn, results in allosteric activation of pyruvate kinase isoform M2 (PKM2) by serine (driving the flux towards pyruvate in conditions with plentiful serine) (Amelio et al., 2014). PKM2, the characteristic pyruvate kinase isoenzyme in rapidly proliferating cells such as embryonic cells and tumor cells, drives Warburg metabolism (Mazurek, 2011), highlighting the central importance of serine in cancer beyond feeding C1 metabolism. Additionally, PHGDH is upregulated in triple-negative breast cancer and melanoma (Amelio et al., 2014; Possemato et al., 2011) and its genetic locus on

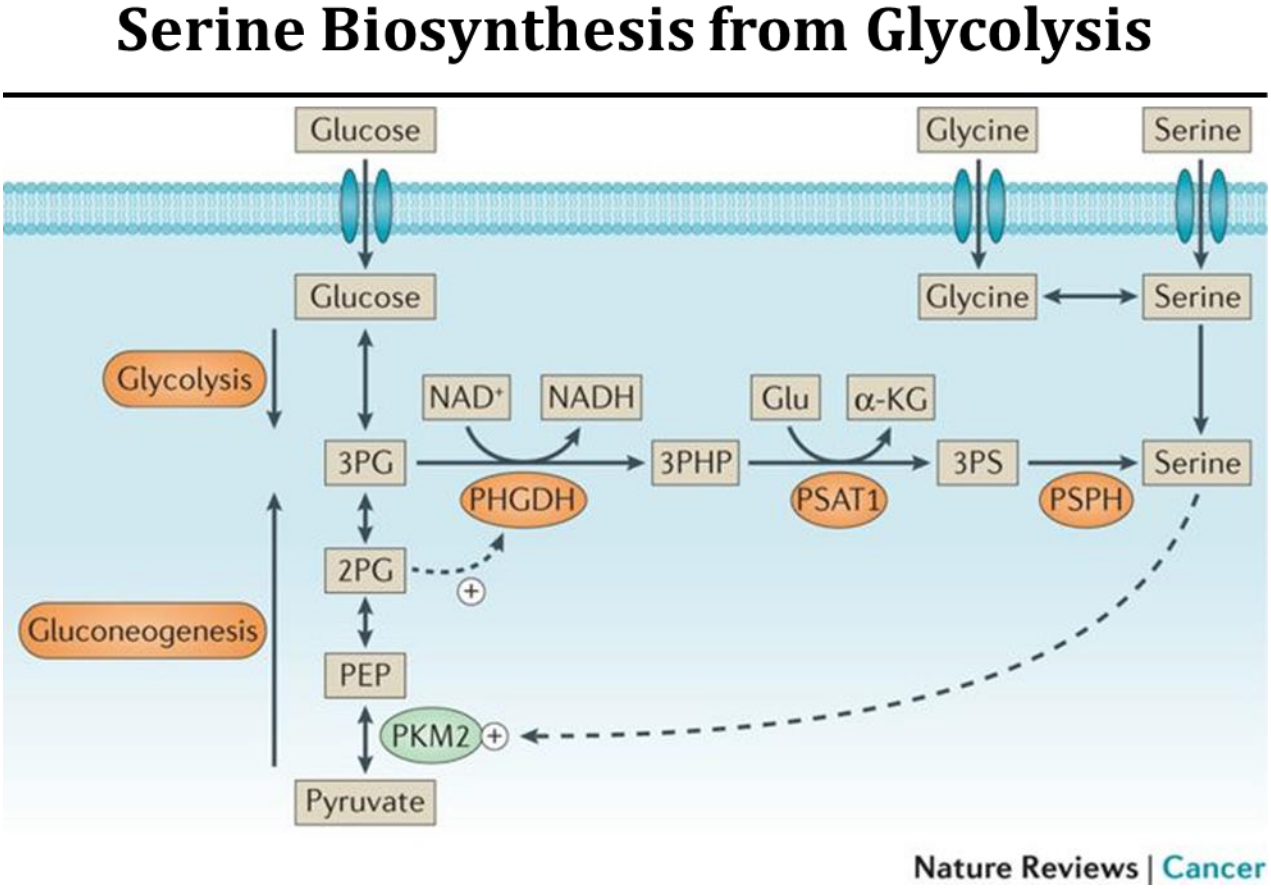

Figure 1.4 Serine Biosynthesis from Glycolysis. Glycolytic intermediates include 3-phosphoglycerate (3PG), 2PG and phosphoenolpyruvate (PEP). Phosphoglycerate dehydrogenase (PHGDH) can convert 3PG into 3-phosphohydroxypyruvate (3PHP), which is subsequently converted to 3-phosphoserine (3PS) by phosphoserine aminotransferase1 (PSAT1) and ultimately into serine by phosphoserine phosphatase (PSPH). Serine can allosterically activate pyruvate kinase isoform M2 (PKM2), diverting glycolytic flux towards pyruvate. In the absence of serine, PKM2 is downregulated, diverting the glycolytic flux towards serine biosynthesis. Accumulation of 2PG, indicating sufficient glycolytic end-products, can allosterically activate PHGDH to divert glycolytic flux towards serine biosynthesis. Adapted from (Yang and Vousden, 2016).

chromosome 1p12 is often amplified in these cancers even though the locus contains no oncogenes (Beroukhim et al., 2010), suggesting serine biosynthesis may drive these tumors. Indeed, ectopic expression of PHGDH in MCF10A mammary epithelial cells induced proto-oncogenic changes including loss of polarity, disrupted morphogenesis, and survival outside of the extracellular matrix (Locasale et al., 2011). Moreover, suppression of PHGDH in PHGDH-amplified cell lines suppressed growth (Locasale et al., 2011), confirming the necessity of PHGDH upregulation in driving these cancers.

1.1.5 Therapeutic Targeting of One-Carbon Metabolism

The challenge in developing effective therapeutics against cancer is designing agents that will selectively kill cancer cells while sparing normal tissues (or as Siddhartha Mukherjee so elegantly stated in The Emperor of All Maladies, "dissolve away the left ear… and leave the right ear unharmed") (Mukherjee, 2010). Naturally, rapidly proliferating cells such as cancer cells require far more nucleotides than mostly senescent normal tissue (Locasale, 2013). This dichotomy initially provided a rationale and therapeutic window for targeting of nucleotide biosynthesis within C1 metabolism as a cancer treatment modality.

1.2 Folates and Antifolates

C1 metabolism is driven by folates, which encompass a group of water-soluble compounds within the vitamin B9 family (Naderi and House, 2018) that consist of linked pterin, p-aminobenzoic acid, and L-glutamate moieties (**Figure 1.5**). Folate deficiency in adults and children results in pathologies secondary to perturbed C1 metabolism including insufficient nucleotide biosynthesis for faithful cellular replication (such as megaloblastic anemia or cancer) or secondary to Hcy accumulation (hyperhomocysteinemia leading to cardiovascular disease) (Bailey et al., 2015). In the developing fetus, folate deficiency can, by the same etiology, lead to

Folic Acid

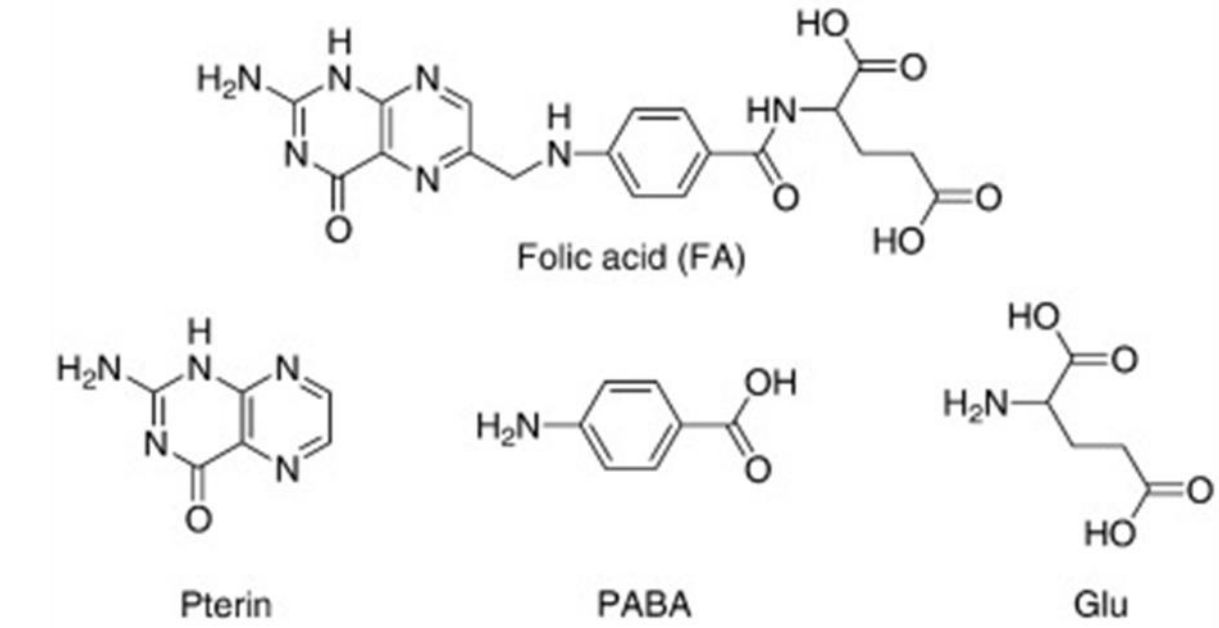

Figure 1.5 Structure of Folic Acid and Moieties. Folic acid is composed of three structural moieties, a pterin, p-aminobenzoic acid (PABA), and one or more glutamates. Adapted from (Gazzali et al., 2016)

a set of disorders known as “neural tube defects” wherein nervous tissue herniates through the cranial region (e.g. anencephaly) or spinal region (spina bifida) (Beaudin and Stover, 2009).

While many species from bacteria to plants synthesize folate *de novo*, humans and animals cannot (Ducker and Rabinowitz, 2017) and therefore, folates must be taken in through the diet as reduced THF derivatives from leafy green vegetables and/or as folic acid in fortified foods (Martiniak et al., 2015). As biological folate cofactors are all THF derivatives, dietary folic acid must be sequentially reduced to DHF and then to THF (**Figure 1.6**). The most common THF derivative naturally found in food is 5-methylTHF (also the predominant form found in the circulation) followed by 5- and 10-formylTHF and their interconversion intermediates (Jägerstad and Jastrebova, 2013). As described previously, 5,10-meTHF, 5-methylTHF, and 10-formylTHF are critical cofactors in C1 metabolism with 5-formylTHF (i.e. leucovorin) acting as a C1 unit reserve (Ducker and Rabinowitz, 2017). 5,10-methenylTHF plays no cofactor role, but is an intermediate between the dehydrogenase and cyclohydrolase conversions of MTHFD1 in the cytosol and MTHFD2/MTHFD2L in mitochondria (Ducker and Rabinowitz, 2017).

Since the discovery that folate supplementation could accelerate acute lymphoblastic leukemia (ALL) in children, folate-based inhibitors of C1 metabolism (“antifolates”) have played a critical role in chemotherapeutic regimens (Farber et al., 1947; Farber and Diamond, 1948). With these agents, aminopterin and amethopterin, Farber and his contemporaries achieved selective cytotoxicity of ALL cells, and remarkably, the latter, now known as methotrexate (MTX), continues to be a mainstay in regimens for treating ALL and solid tumors as well (Mager, 2015). Both MTX and aminopterin, as well as next-generation antifolates, are reviewed in detail in section 1.4

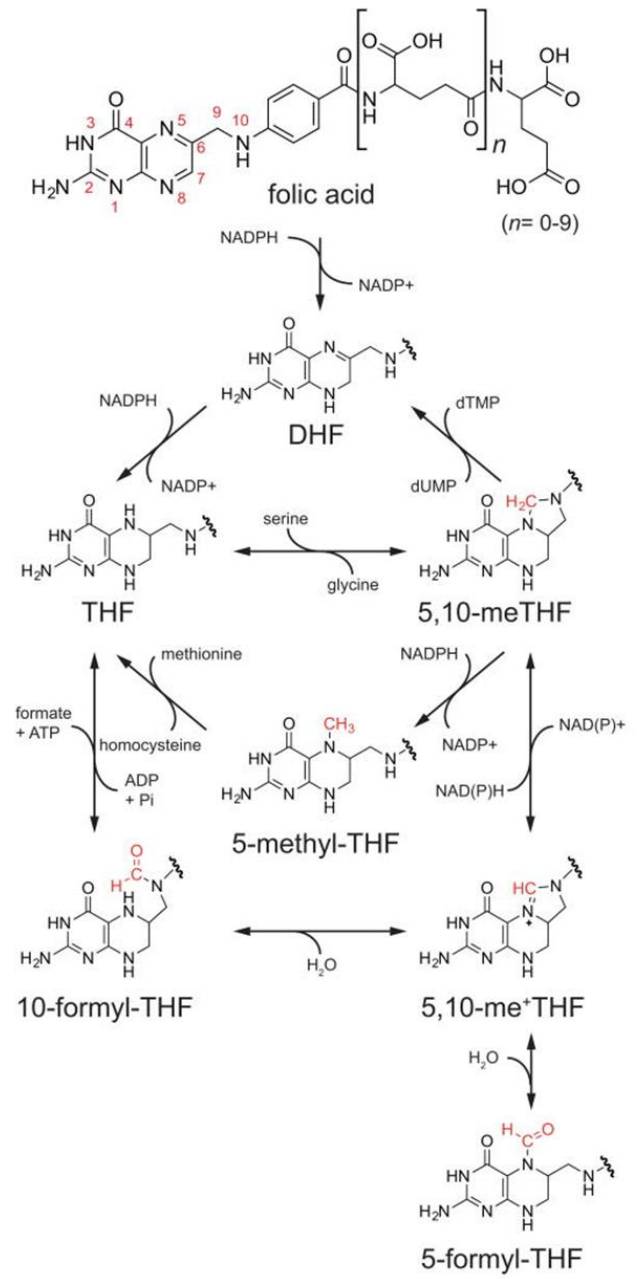

Figure 1.6 Forms of Folic Acid. Folic acid in its native form appears as a supplement in foods such as bread. The various folate forms below represent different biologically active cofactors which mediate one-carbon metabolism. DHF: Dihydrofolate, THF: Tetrahydrofolate, 5,10-meTHF: 5,10-methyleneTHF, 5,10-me^{+}THF: 5,10-methenylTHF. Adapted from (Ducker et al., 2017)

1.3 Folate Transport and Compartmentation

Due to their hydrophilic nature, circulating folates (and antifolates) have limited capacity to diffuse across cellular and mitochondrial membranes (Hou and Matherly, 2014). Therefore, mammalian cells have evolved three distinct uptake systems (**Figure 1.7**) to facilitate folate transport across the plasma membrane: the reduced folate carrier (RFC – SLC19A1), the proton-coupled folate transporter (PCFT- SLC46A1), and folate receptors (FR) (Zhao, 2011). While the mechanism for folate uptake into the nucleus is poorly understood (Scotti et al., 2013), the mitochondrial folate transporter (MFT – SLC25A32) is the only known transporter of folates from the cytosol into the mitochondrial matrix (McCarthy et al., 2004). Notably, only monoglutamate folates are transported across membranes and accumulation of folates in either the cytosolic or mitochondrial compartments requires the successive addition of multiple glutamate moieties (i.e. polyglutamylation) to the γ-carboxylate group of glutmatate linked to the p-aminobenzoic acid moiety in a reaction catalyzed by compartment-specific isoforms of folylpoly-γ-glutamate synthetase (FPGS) (Lawrence et al., 2014; Shane, 1989). These polyglutamatyl folate forms are sequestered in their respective subcellular compartments and are not substrates for transmembrane transport, meaning the folate pools in the mitochondria and cytosol are essentially distinct and not in equilibrium (Lawrence et al., 2014). Moreover, polyglutamylation of folates also enhances their enzyme affinity (Raz et al., 2016). The reverse reaction (reversion of polyglutamatyl derivatives to the monoglutamate form) is catalyzed by conjugases which are located in the intestinal brush border (where they revert the predominantly polyglutamate dietary folates to monoglutamates for intestinal absorption) and in the lysosome (where they regulate intracellular levels of polyglutamyl folates) (Wang et al., 1986).

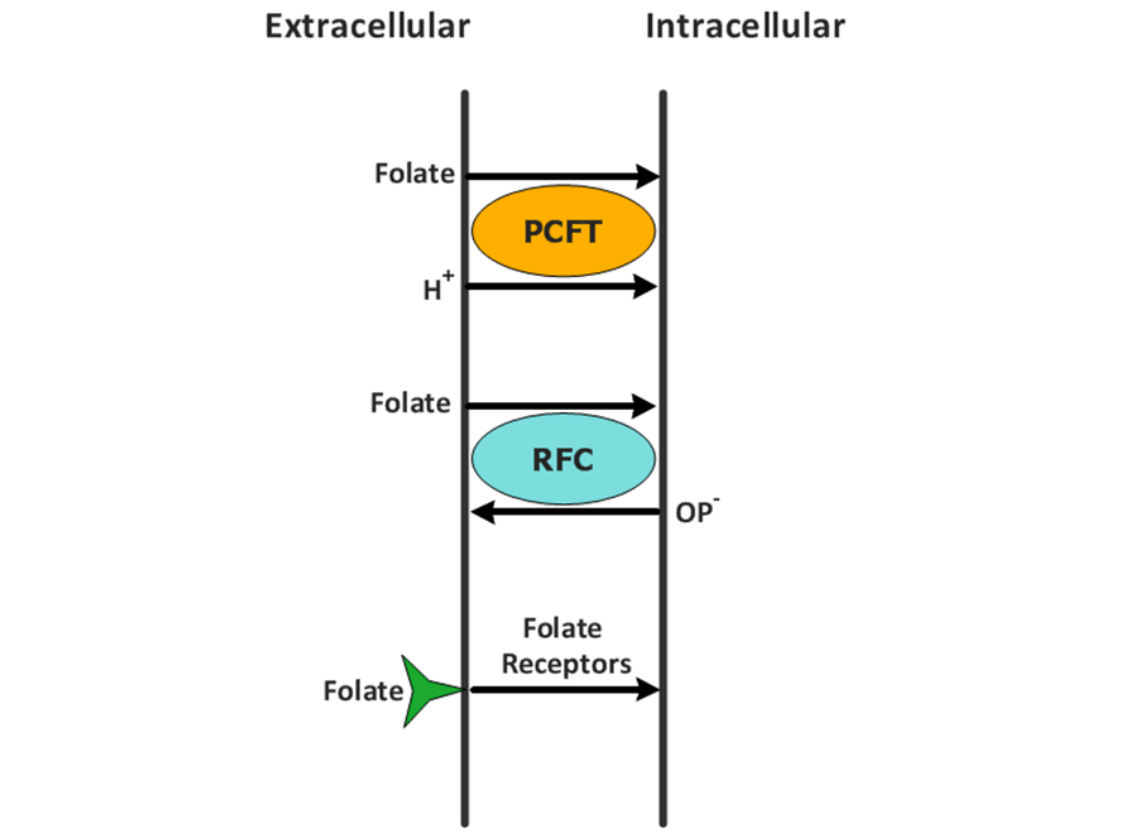

Figure 1.7 Plasma Membrane Folate Transporters. Folates are transported across the plasma membrane by three major transporters: the proton-coupled folate transporter (PCFT – a proton/folate symporter), the reduced folate carrier (RFC- an organic phosphate (OP^-)/folate antiporter), and the folate receptors (FR).

1.3.1 Reduced Folate Carrier

RFC is a member of the solute carrier (SLC) group within the Major Facilitator Superfamily (MFS) of transporters, the latter of which includes the mammalian glucose transporters, drug efflux pumps, as well as amino acid transporters (Hou and Matherly, 2014; Matherly et al., 2007). Containing 591 residues, RFC is a homo-oligomeric integral membrane protein with twelve membrane-spanning transmembrane domains and both carboxy- and amino-termini oriented towards the cytoplasm (Matherly et al., 2007). RFC transports reduced folates by exchanging them with organic anions such as phosphates (**Figure 1.7**) and is the major transporter for reduced folates in mammalian cells, where its physiological substrate is 5-methylTHF and knockout (KO) of RFC is embryonic lethal (Matherly et al., 2007; Matherly et al., 2014; Zhao et al., 2001). Due to the ubiquitous expression of RFC in both normal and tumor tissues, antifolates which are substrates for RFC carry significant dose-limiting toxicities in normal tissues, making RFC uptake of antifolates undesirable (Matherly et al., 2007; Matherly et al., 2014; Zhao et al., 2001). As influx of folates is coupled to efflux of anions, RFC activity is potentiated by relatively low concentrations of anions in the extracellular compartment (Henderson and Zevely, 1983). Of note, RFC transport maintains a neutral pH optimum with significantly diminished transport activity below pH 7 (Matherly et al., 2007; Sierra et al., 1997; Zhao, 2011). Transport is generally saturable at low micromolar concentrations of reduced folates (K_m = 1-2 μM) with extremely low affinity for folic acid (K_m = 50-200 μM) (Sirotnak and Tolner, 1999). The best known substrate for RFC is the δ-hemiphthaloylorinithine antifolate PT523 which has submicromolar K_m (Rosowsky et al., 1994) and is discussed in further detail in section 1.4.1 .

1.3.2 Proton Coupled Folate Transporter

PCFT is another SLC/MFS member discovered in 2006 (Qiu et al., 2006). Containing 459 residues, PCFT also likely contains twelve transmembrane domains with both termini oriented towards the cytoplasm (Desmoulin et al., 2012a). A proton/folate symporter (**Figure 1.7**), PCFT unsurprisingly functions optimally at an acidic pH (optimum ~ pH 5.5). PCFT is expressed physiologically primarily in the acidic apical brush-border of the proximal duodenum and jejunum (where its primary role is the uptake of folates from the diet), as well as in the kidney, liver, and choroid plexus (Desmoulin et al., 2012a). In the latter tissues, however, RFC is the predominant folate uptake mechanism as PCFT-mediated uptake is minimal at the physiological pH of 7.4 (Zhao et al., 2008). Loss-of-function of PCFT leads to hereditary folate malabsorption, which results in symptoms secondary to folate deficiency including megaloblastic anemia, immune deficiency, and neurological dysfunction (Zhao et al., 2007). Notably, PCFT is expressed in a variety of solid tumors including colorectal adenocarcinoma, ovarian cancer, hepatocellular carcinoma, and lung adenocarcinoma (Kugel Desmoulin et al., 2011; Wilson et al., 2016). The extracellular pH of these tumors is often acidic (pH ~ 6.7-7.1) due to Warburg metabolism and poor perfusion (Webb et al., 2011), meaning PCFT is functionally active in these cells. Therefore, selective uptake of antifolates by PCFT over RFC would be desirable as PCFT has relatively minimal physiological activity in normal tissues. At pH 5.5, PCFT-mediated transport of both reduced folates and folic acid is generally saturable at low micromolar concentrations (K_m = 1-5 μM) (Zhao, 2011). The best known substrates for PCFT are the 5-substituted pyrrolo[2,3-*d*]pyrimidine antifolate pemetrexed (PMX - K_m = 30-90 nM) (Desmoulin et al., 2012b; Zhao and Goldman, 2007) and the 6-substituted pyrrolo[2,3-

d]pyrimidine antifolate AGF94 (K_m = 20 nM) (Desmoulin et al., 2012b). These antifolates are discussed in further detail in sections 1.4.2 and 1.4.4 respectively.

1.3.3 Folate Receptors

The last major plasma membrane folate transporters, the FRs, have homologous alpha (FRα), beta (FRβ), and gamma (FRγ) isoforms (Elnakat and Ratnam, 2004). The former two are cell surface glycosyl phosphatidylinositol (GPI)-anchored glycoproteins and effect folate uptake, whereas the latter has no GPI-anchor and is a secretory protein with unknown function (Elnakat and Ratnam, 2004). FRα, the more widely physiologically expressed isoform, is generally expressed on the apical surface of epithelial cells, including the choroid plexus, proximal kidney tubules (where it reabsorbs filtered folates), and placenta (Weitman et al., 1992) while FRβ is expressed in hematopoietic cells and in the placenta (Ratnam et al., 1989; Reddy et al., 1999). Folate uptake by FR is mediated by endocytosis followed by acidification of the endosome, which allows PCFT-mediated export into the cytosol (**Figure 1.7**) (Zhao et al., 2009). As with PCFT, FRs in general and FRα in particular have limited physiological expression with the latter predominantly expressed on the apical surfaces of epithelium and consequently out of contact of antifolates in the circulation (Elnakat and Ratnam, 2004). In addition, a subset of cancers including breast, ovarian, and lung have been shown to overexpress FRα and loss of cellular polarity in these cells means the receptor comes in contact with the circulation and may be used as a tumor-selective drug transporter (Cheung et al., 2016; Low and Antony, 2004). FRα is saturable at extremely low (1-10 nM) concentrations of both folic acid and reduced folates (Kamen and Smith, 2004). As folic acid itself is an extremely potent FRα substrate, small-molecule drugs (such as *Vinca* alkaloids) conjugated to folic acid (e.g. Vintafolide) (Assaraf et al., 2014; Vergote and Leamon, 2015) and FRα-targeted antibodies (e.g. Farletuzumab) (Sato

and Itamochi, 2016) have been developed as drugs to selectively target tumors. In addition, development of FRα-selective antifolates began with the discovery of BGC945 (ONX0801) (Gibbs et al., 2005), which successfully demonstrated efficacy in a Phase I trial (Banerji et al., 2017). Moreover, development of pyrrolopyrimidine FRα-selective antifolates remains ongoing as well (Hou et al., 2017; Ravindra et al., 2018; Wang et al., 2012; Wang et al., 2011; Wang et al., 2015; Wang et al., 2013).

1.3.4 Mitochondrial Folate Transporter

While there are three separate plasma membrane folate transporters, MFT is the only known transporter of folates from the cytosol into the mitochondrial matrix (McCarthy et al., 2004). Discovered in 2000 (Titus and Moran, 2000), MFT is a member of the mitochondrial carrier family (which includes mammalian ATP/ADP exchange carriers, phosphate carriers, and uncoupling carriers) (Kuan and Saier, 1993). MFT has six transmembrane domains consisting of three tandem repeats of 100 amino acids and transports THF from the cytosol into the mitochondrial matrix (Lawrence et al., 2011). Notably, MFT KO prevents mitochondrial accumulation of folates and consequently, induces glycine auxotrophy in cells secondary to insufficient mitochondrial THF as a cofactor for the SHMT2 reaction (**Figure 1.1**) (McCarthy et al., 2004). As no previously reported folate analogs target mitochondrial C1 metabolic enzymes, the importance of MFT in antifolate efficacy is unclear.

1.4 Therapeutic Targeting of Cytosolic One-Carbon Metabolism

All clinically used antifolates currently target nucleotide biosynthetic enzymes in cytosolic C1 metabolism. The earliest such enzyme targets included DHFR (by MTX) (Farber et al., 1947; Farber and Diamond, 1948) and TS (by the suicide inhibitor 5-fluorouracil (5-FU)) (Rich et al., 1958). While current clinically used antifolates continue to target DHFR and TS,

development of antifolates targeting alternate enzymes such as GARFTase and AICARFTase in *de novo* purine biosynthesis remains ongoing (Deis et al., 2016; Deng et al., 2008; Golani et al., 2016; Mitchell-Ryan et al., 2013; Xing et al., 2017).

1.4.1 Targeting DHFR

Since the discovery of aminopterin and amethopterin (i.e. MTX) (**Figure 1.8**) by Farber and colleagues in the late 1940s, DHFR inhibitors have played a key role in chemotherapeutic arsenals (Farber et al., 1947; Farber and Diamond, 1948). Despite their longstanding success, DHFR inhibitors face two major, intrinsic hurdles to efficacy: first, that inhibition of greater than 95% of cellular DHFR is required to suppress cellular THF pools and second, that DHF accumulates behind a DHFR block and can compete with the inhibitor for binding the enzyme (Visentin et al., 2012). Despite these drawbacks, MTX remains incredibly successful for a 70 year old agent, as it is widely used not only in treating solid and hematological tumors (including leukemias, lymphomas, and osteosarcomas) (Jaffe, 2009; Matloub et al., 2011), but also in nonmalignant diseases like Crohn's disease and rheumatoid arthritis (Abolmaali et al., 2013). MTX overcomes these hurdles by achieving micromolar intracellular concentrations through polyglutamylation by FPGS, which simultaneously effects drug retention while enhancing affinity for DHFR (Fabre et al., 1984). However, the dependence of MTX on polyglutamylation is its Achilles' heel as impaired MTX polyglutamylation due to decreased affinity for or expression of FPGS can drive MTX resistance (Longo et al., 1997; Pizzorno et al., 1988). To circumvent MTX resistance stemming from impaired polyglutamate formation, research drove towards two divergent schools of thought: either (1) generating DHFR inhiibtors which did not require polyglutamylation (which resulted in the development of PT523 (Rosowsky, 1999)); or (2) generating DHFR inhibitors with enhanced affinity for FPGS (leading to pralatrexate (PTX))

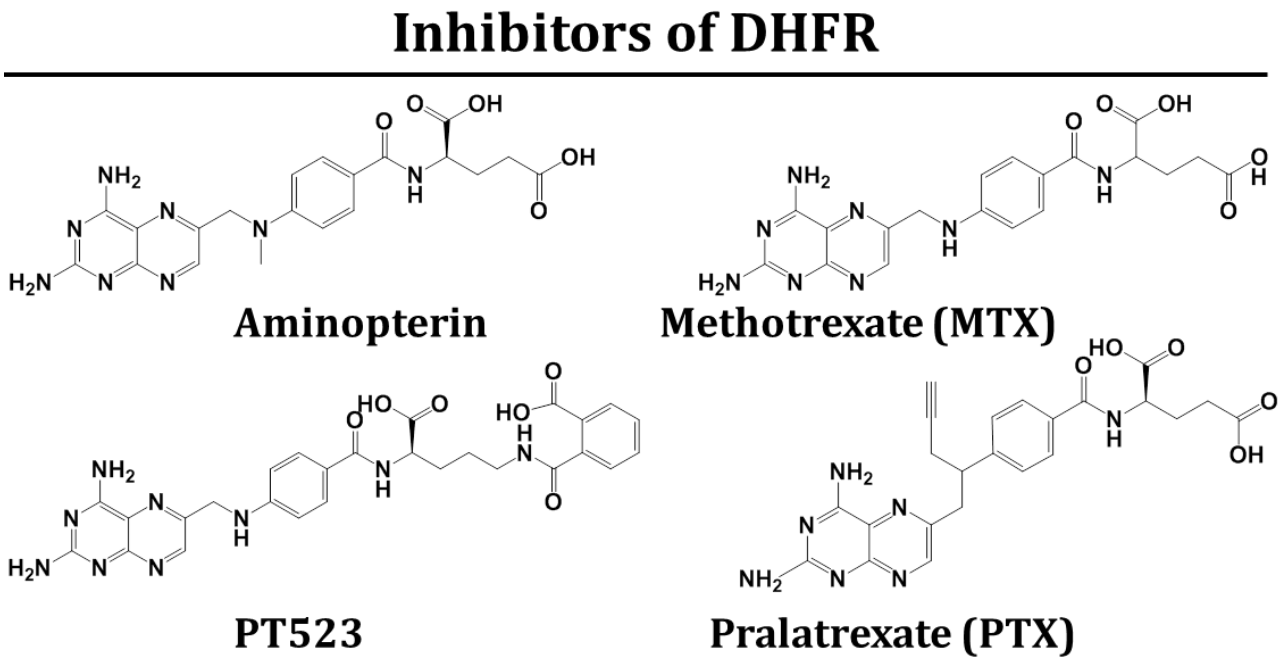

Figure 1.8 Antifolate Inhibitors of DHFR. Aminopterin and methotrexate (MTX) were among the first chemotherapeutic agents discovered by Sidney Farber and colleagues in the late 1940s. PT523 substituted a hemiphthaloylornithine moiety for the glutamate in MTX, preventing the need for polyglutamylation whereas pralatrexate (PTX) featured a C in place of the N at the 10-position of MTX as well as a terminal alkyne group.

(O'Connor et al., 2017) (**Figure 1.8**). PT523 featured a hemiphthaloylornithine moiety in place of the glutamate moiety on MTX (and most folate analogs) that prohibited its polyglutamylation (Rosowsky, 1999). Consequently, in order to accumulate in sufficient amounts to therapeutically inhibit DHFR, PT523 had to be an excellent substrate for RFC and indeed, PT523 is the best known substrate for this transporter (Matherly et al., 2007). Similarly, PTX also featured much more rapid cellular uptake and polyglutamylation than MTX (Visentin et al., 2013). Further, due to efficient retention of PTX polyglutamyl derivatives in cancer cells, PTX could be dosed weekly (O'Connor et al., 2011) whereas MTX must be dosed daily (Mager, 2015). However, both PT523 and PTX, along with MTX, rely heavily on RFC-mediated uptake for efficacy and as RFC is ubiquitously expressed in normal tissues, dose-limiting toxicities are to be expected. Consequently, clinical use for PTX is limited to cutaneous T-cell lymphoma (Foss et al., 2018) and PT523 actually featured excessive hematological toxicity, prohibiting its clinical use (Rosowsky, 1999).

1.4.2 Targeting TS

Along with DHFR, inhibitors of TS (**Figure 1.9**) make up a significant portion of the classical antifolates. The first TS inhibitors were not folate analogs, but pyrimidine analogs such as 5-FU (Rich et al., 1958). In the cell, 5-FU is converted into F-dUMP which binds the nucleotide binding site of TS and, with 5,10-meTHF, forms a ternary complex that prevents formation of thymidylate (Longley et al., 2003). Thymidylate depletion then leads to perturbations of the other dNTP pools (Aherne et al., 1996; Yoshioka et al., 1987) as well as misincorporation of dUMP into DNA, which are lethal (Longley et al., 2003). 5-FU and its prodrug capecitabine (Walko and Lindley, 2005) are used in treatment of colorectal and breast cancers, but response rates as a colon cancer monotherapy were dismal (11%)

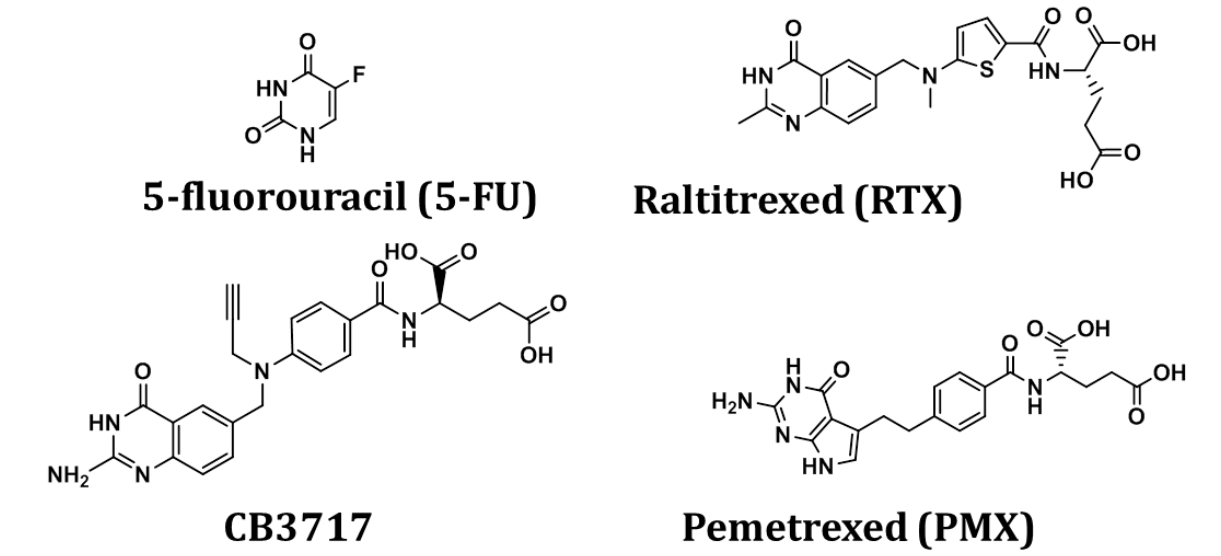

Figure 1.9 Inhibitors of TS. 5-fluorouracil (5-FU) was the first synthesized inhibitor of thymidylate synthase (TYMS or TS). As inhibition of TS at the dUMP binding site was less advantageous compared to inhibition at the folate binding site, folate analog TS inhibitors were synthesized, including CB3717. Due to the nephrotoxicity of CB3717, raltitrexed (RTX) was designed to improve the solubilitiy of CB3717. Further optimization yielded pemetrexed (PMX), which is still used in clinic today.

(Thirion et al., 2004). Surprisingly, supplementation with leucovorin actually potentiates 5-FU activity (doubling response rate) (Thirion et al., 2004) by increasing 5,10-meTHF levels (Chu et al., 2003) whereas it generally eases side-effects of other antifolates such as MTX (Howard et al., 2016). The development of 5-FU validated TS as a *bona fide* chemotherapeutic target, but the clinical results were disappointing, leading to the development of novel, folate-based TS inhibitors as it was believed the folate binding site of TS offered better design opportunities than the nucleotide binding site (Jackman and Calvert, 1995). As with inhibition of DHFR by MTX, inhibition of TS by 5-FU leads to a buildup of the substrate (up to millimolar concentrations of dUMP) behind the enzyme block (Jackson et al., 1983; Mitrovski et al., 1994) which can competitively inhibit 5-FU binding to TS, self-limiting the effect of the drug (Myers et al., 1975). Folate-based inhibitors of TS, however, would bind at the folate-binding site of TS rather than the dUMP site and would be unaffected (Chattopadhyay et al., 2004).

Although initial efforts resulted in the synthesis of a clinically efficacious quinazoline-based antifolate in CB3717, it induced life-threatening nephrotoxicity in patients due to drug precipitation in the renal tubules (Calvert et al., 1986). To overcome this dose-limiting toxicity, the next-generation quinazoline compound ZD1694 (Raltitrexed or RTX) demonstrated increased water-solubility (Jackman and Calvert, 1995). Like MTX, RTX uptake into the cell was found to be mediated by RFC and it was an excellent substrate for polyglutamylation by FPGS (Touroutoglou and Pazdur, 1996), which allowed for dosing once every three weeks (Chu et al., 2003). Two phase III trials comparing RTX monotherapy to 5-FU/leucovorin combination therapy in untreated, advanced colorectal cancer were conducted. In the European study, response rates, time to progression, and median survival were similar between treatment arms although RTX featured significantly lower incidence and severity of toxicity (Cunningham et al.,

1996), leading to approval of RTX as a first-line colorectal cancer agent in Europe, Japan, Canada, and Australia (Chu et al., 2003). In the North American trial, the RTX treatment arm also showed similar response rates to the 5-FU/leucovorin treatment arm. However, time to progression and overall survival were significantly increased in the latter arm (Pazdur, 1997) and RTX was not approved by the FDA (Chu et al., 2003). Interestingly, the difference in efficacy of RTX between Europe and the US could reflect the latter's mandatory fortification of foods with folic acid (Mills and Dimopoulos, 2015), which would increase serum folate levels, leading to increased competition for antifolate uptake.

Efforts to further improve the potency of RTX resulted in the development of PMX, which substituted the 6-5-fused pyrrolo[2,3-*d*]pyrimidine nucleus for the 6-6 fused quinazoline ring structure of RTX (Shih et al., 1997). Like RTX, PMX featured high affinity for RFC and was a very potent substrate for FPGS as well, resulting in rapid and long-lasting accumulation in cancer cells (Goldman and Zhao, 2002) and effecting an every three week dosing schedule (Chu et al., 2003). Unlike RTX, though, PMX also featured potent uptake by PCFT, leading to enhanced rather than muted efficacy in cells with loss-of-function of RFC (Desmoulin et al., 2012b). Moreover, PMX was the first successful multitargeted folate agent, inhibiting primarily TS, but also DHFR and the purine biosynthetic enzymes GARFTase and AICARFTase (Adjei, 2004). In fact, PMX's inhibition of AICARFTase triggered an entirely different mechanism of efficacy by inducing accumulation of AICAR (ZMP), leading to activation of AMP-activated kinase (AMPK) and consequent downregulation of mammalian target of rapamycin (mTOR) (Racanelli et al., 2009; Rothbart et al., 2010). While secondary to its effects at TS, PMX's inhibition of these secondary drug targets effected its potency in cell lines resistant to the single-target TS inhibitors like 5-FU and RTX (Hanauske et al., 2001). However, TS expression still

remained the primary determinant of PMX resistance (Zhang et al., 2011) Ultimately, PMX was, and remains today, the most successful TS inhibitor discovered. It is currently approved to treat mesothelioma and non-small cell lung cancer in combination therapy with a platinum agent as first- and second-line therapy (Cohen et al., 2009; Esteban et al., 2009) and as a monotherapy for maintentance (Ciuleanu et al., 2009).

1.4.3 Targeting *De Novo* Purine Biosynthesis

Since inhibition of DHFR by agents such as MTX was shown to be self-limiting (due to competitive inhibition of these drugs by the accumulated DHF as discussed in section 1.4.1), subsequent research approaches focused on generating inhibitors of alternate pathways, such as thymidylate synthesis. Another such alternate pathway was *de novo* purine biosynthesis, which contains two folate-dependent targetable enzymes, GARFTase and AICARFTase (Appling, 1991). The first inhibitor of *de novo* purine biosynthesis was the purine antimetabolite, 6-mercaptopurine (6-MP - **Figure 1.10**) (Hitchings and Elion, 1954) which is used in maintenance therapies for pediatric ALL (Stork et al., 2010) and inhibits phosphoribosyl pyrophosphate (PRPP) amidotransferase, the first enzyme in *de novo* purine biosynthesis (Nelson et al., 1975). The first folate-based inhibitor of *de novo* purine biosynthesis was the GARFTase inhibitor lometrexol (LMX – **Figure 1.10**), which was designed to be structurally identical to THF (**Figure 1.6**) except for the substitution of non- reactive carbon atoms for the nitrogen atoms at the 5 and 10 positions, preventing the acceptance of C1 units (Beardsley et al., 1989). Moreover, inhibition of GARFTase by LMX was found to be cytotoxic independent of p53 mutation status (Bronder and Moran, 2002) and as a whole, many cancer cells are overly reliant on the *de novo* purine biosynthesis pathway as they are methylthioadenosine phosphorylase (MTAP)-deficient and cannot salvage adenine (Bertino et al., 2011). Like many other classical antifolates discussed

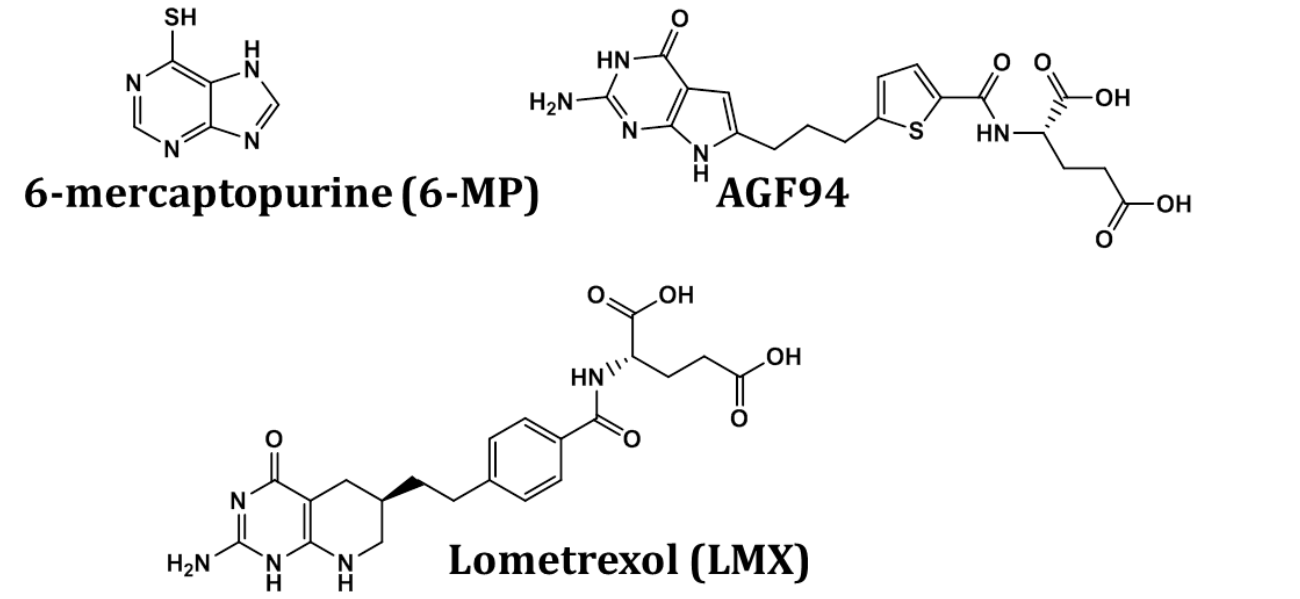

Figure 1.10 Inhibitors of *De Novo* Purine Biosynthesis. 6-mercaptopurine (6-MP) was the first inhibitor of *de novo* purine biosynthesis, inhibiting the enzyme PRPP (phosphoribosyl-pyrophosphate) amidotransferase, the first enzyme in the pathway. Lometrexol (LMX) was the first folate-based inhibitor of this pathway, targeting GARFTase, the first folate-dependent enzyme. AGF94 is a next-generation GARFTase inhibitor which carries much improved selectivity for PCFT versus RFC as compared to LMX.

previously, though, LMX featured RFC-mediated uptake and a strong dependence on FPGS-mediated polyglutamylation, which ultimately allowed for development of resistance (Tse and Moran, 1998). Notably, mutations in RFC resulted in decreased affinity for LMX and increased affinity for folic acid and leucovorin (Tse et al., 1998). This, in turn, increased intracellular folate pools which competed against LMX for polyglutamylation by FPGS (Tse et al., 1998). Ultimately, while LMX was potent against leukemia cells *in vitro* and clinical activity was investigated in a phase I trial (Ray et al., 1993; Sessa et al., 1996), further development of this drug was abandoned, likely due to dose limiting toxicities. Interestingly, though, refinement of the structure-activity relationship of LMX directly led to the development of PMX (Chattopadhyay et al., 2007).

1.4.4 Limitations of Classical Antifolates

While roughly 60 years of antifolate research led to the development of the classical antifolates described above, these agents (and indeed, chemotherapeutics in general) must overcome two main hurdles: tumor selectivity and the development of drug resistance. All classical antifolates discussed above are substrates for the ubiquitously expressed RFC, meaning these drugs are nonselectively transported into both normal tissues and cancer cells. The selectivity of these agents, then, is limited to their targeting of nucleotide biosynthesis, which is critical to cancer cells, but also to other rapidly proliferating tissues such as hematological cells. Indeed, the dose-limiting toxicities of both PMX (Cohen et al., 2009) and MTX (Hansen et al., 1971) are neutropenia or thrombocytopenia. Moreover, loss-of-function of RFC is a common means of resistance to antifolates reliant solely on RFC-mediated uptake (Matherly et al., 2007). However, the efficacy of antifolates such as PMX, which have significant PCFT-mediated

uptake, is unaffected and, indeed, may actually increase (Chattopadhyay et al., 2006; Desmoulin et al., 2012b).

The other major hurdle antifolates must overcome is the development of drug resistance, which often results from alterations in the primary enzyme target (Zhao and Goldman, 2003). For MTX, amplification of (Schimke, 1988) or mutations in (Jackson et al., 1976) DHFR can lead to resistance whereas for PMX, resistance is usually secondary only to increased expression of TS (Shimizu et al., 2016). However, resistance to LMX, the GARFTase inhibitor, is due to mutations in FPGS or decreased RFC-mediated uptake (Zhao and Goldman, 2003). The lack of resistance due to mutations in GARFTase suggests a PCFT-selective GARFTase inhibitor (which would theoretically circumvent the RFC-mediated toxicity of LMX) would be a more robust drug than either MTX or PMX. Indeed, AGF94 (**Figure 1.10**), a 6-substituted pyrrolo[2,3-*d*]pyrimidine with a thiophene heterocyclic group is an incredibly potent inhibitor of GARFTase (K_i = 68 nM relative to 10-formyl-dideazafolic acid, a 10-formylTHF analog) (Deis et al., 2016) with 30-fold selectivity for PCFT over RFC (Wang et al., 2015). Due to its potential selectivity and efficacy in targeting mesothelioma (Cherian et al., 2013), further clinical testing of AGF94 is ongoing (unpublished observations).

As for the classical antifolates, despite being nonselectively transported by RFC and primarily targeting only TS, PMX remains the most clinically successful of these agents discovered to date. Unlike the others, though, PMX has extremely potent PCFT-mediated uptake (which circumvents resistance due to loss-of-RFC) and it is, nominally, a multitargeted agent which enables its efficacy in RTX- and 5-FU-resistant tumors. Moreover, its high affinity for FPGS enhances its intracellular retention, allowing for an advantageous once-every-three-week dosing scheme as discussed previously in section 1.4.2. Therefore, it is likely that PCFT-

selective multitargeted agents in the mold of PMX will be highly promising drugs. As PMX already inhibits multiple different cytosolic C1 metabolism enzymes, these novel drugs would have to target alternate C1 metabolism enzymes, such as those in the mitochondria.

1.5 Therapeutic Targeting of Mitochondrial One-Carbon Metabolism

Beyond generating formate for downstream cytosolic nucleotide biosynthesis, mitochondrial C1 metabolism enzymes, particularly MTHFD2 and SHMT2 (**Figure 1.1**), play a multitude of additional critical roles in cancer cells as discussed previously in section 1.1.3. Moreover, a survey of nearly 1500 metabolic enzymes across ~2000 tumors of 19 different cancer types identified MTHFD2 and SHMT2 as, respectively, the first and fourth most differentially expressed metabolic enzymes in normal tissues versus cancer cells (Nilsson et al., 2014). Indeed, the glycine biosynthetic pathway as a whole is strongly correlated with cancer cell proliferation rate (Jain et al., 2012). As these enzymes are significantly more expressed in cancer cells rather than normal tissues (even moreso than the classical antifolate enzyme targets TS (tied sixth) and DHFR (tied 32nd) (Nilsson et al., 2014)), targeting these enzymes would confer additional tumor selectivity independent of plasma membrane folate transporter specificity.

1.5.1 Targeting MTHFD2

MTHFD2 is a Myc- and mTOR -regulated enzyme (Ben-Sahra et al., 2016; Pikman et al., 2016) with dehydrogenase and cyclohydrolase activity (Allaire et al., 1998). As discussed previously in section 1.1.3, the NADPH generated by the MTHFD2 reaction is critical for maintaining cellular redox balance and the 10-formylTHF is used to generate formylmethionine-tRNAs for translation of mitochondrial proteins (Minton et al., 2018). As both these functions of MTHFD2 are carried out by MTHFD2L in normal tissues, selective inhibition of MTHFD2 would offer an unprecedented level of tumor selectivity (Tedeschi et al., 2016; Tedeschi et al.,

2015) and research into MTHFD2 as a chemotherapeutic target is ongoing with early positive results in acute myeloid leukemia (AML) and breast cancer models.

In AML, the Stegmaier group demonstrated that downregulation of MTHFD2 is a common mechanism of several AML treatments (Pikman et al., 2016). Suppression of MTHFD2 in AML cell lines yielded increased dependence on extracellular glycine along with G0/G1 cell cycle arrest with minimal effects on non-cancer cell lines. *In vivo*, MTHFD2-targeting small hairpin RNA (shRNA)-transduced U937 AML cells decreased leukemia burden and prolonged survival in nude mice as compared to non-targeted shRNA-transduced controls (NTC). Moreover, a doxycycline-inducible MTHFD2 knockdown (KD) model simulating the effects of inhibiting MTHFD2 after an established AML diagnosis yielded similar results, highlighting the therapeutic potential of MTHFD2 in AML. This effect was particularly pronounced in AML cell lines with FMS-like tyrosine kinase 3 internal tandem duplication (FLT3-ITD) mutations, which are associated with poorer prognosis than FLT3-ITD WT cancers (Badar et al., 2015). This suggests that inhibitors of MTHFD2 could fill a particularly important niche in the treatment of AML.

MTHFD2 overexpression positively correlates with metastasis and invasion (Lehtinen et al., 2013), as well as poor prognosis (Liu et al., 2014) in breast cancer. As with the AML cell lines, KD of MTHFD2 in breast cancer cell lines (Koufaris et al., 2016) increased dependence on extracellular glycine and was not rescuable supplementation with formate, the end-product of mitochondrial C1 metabolism. Metabolomics analysis in the MTHFD2 KD cell lines also demonstrated decreased mitochondrial metabolism coupled with increased glycolytic and glutaminolytic flux, suggesting inhibition of mitochondrial oxidative phosphorylation potentially due to serine modulation of PKM2 (**Figure 1.4**).

Even though the early crystallization of the cytosolic isoform MTHFD1 in complex with inhibitors (Schmidt et al., 2000) identified critical catalytic residues such as Lys56, the development of small molecule inhibitors of MTHFD2 has remained challenging. Initial efforts to drug target MTHFD2 focused on the antibacterial benefits of inhibiting the bacterial ortholog FolD. A high-throughput screening enzyme assay with the intent of inhibiting FolD in *Pseudomonas aeruginosa* identified several lead compounds (Eadsforth et al., 2012), but these showed weak enzyme inhibition and were not used as scaffolds for further drug development. The macrolide keto-carboxylic acid carolacton (**Figure 1.11**), produced by the myxobacterium *Sorangium cellulosum*, was initially shown to inhibit biofilm production in *Streptococcus mutans* and was studied as a potential inhibitor of dental caries (Kunze et al., 2010). Later efforts (Fu et al., 2017) revealed that carolacton inhibited FolD, as well as MTHFD2, in the low nM range, suggesting potential therapeutic efficacy. However, carolacton was a much less potent inhibitor of tumor growth as the half-maximal effective concentration (EC_{50}) values against human tumor cell lines *in vitro* were in excess of 10 μM with cellular export by efflux pumps cited as the main hurdle. Later studies (Gustafsson et al., 2017) with an Eli Lilly compound (LY345899 - **Figure 1.11**) yielded the first crystal structure of an inhibitor complexed with MTHFD2, but LY345899 was unable to cross the plasma membrane, rendering it unsuitable for therapeutic use. Currently, there are no small molecule inhibitors of MTHFD2 with therapeutic potential.

1.5.2 Targeting SHMT2

Like MTHFD2, SHMT2 is also a Myc-regulated enzyme (Ye et al., 2014) and has been found to be critical to cell survival in hypoxic (Ye et al., 2014) or ischemic (Kim et al., 2015) conditions under which it is upregulated by HIF-1α in a Myc-dependent manner (Ye et al., 2014). As only Myc-transformed (i.e. tumor) cells rely on SHMT2 to maintain a sufficient

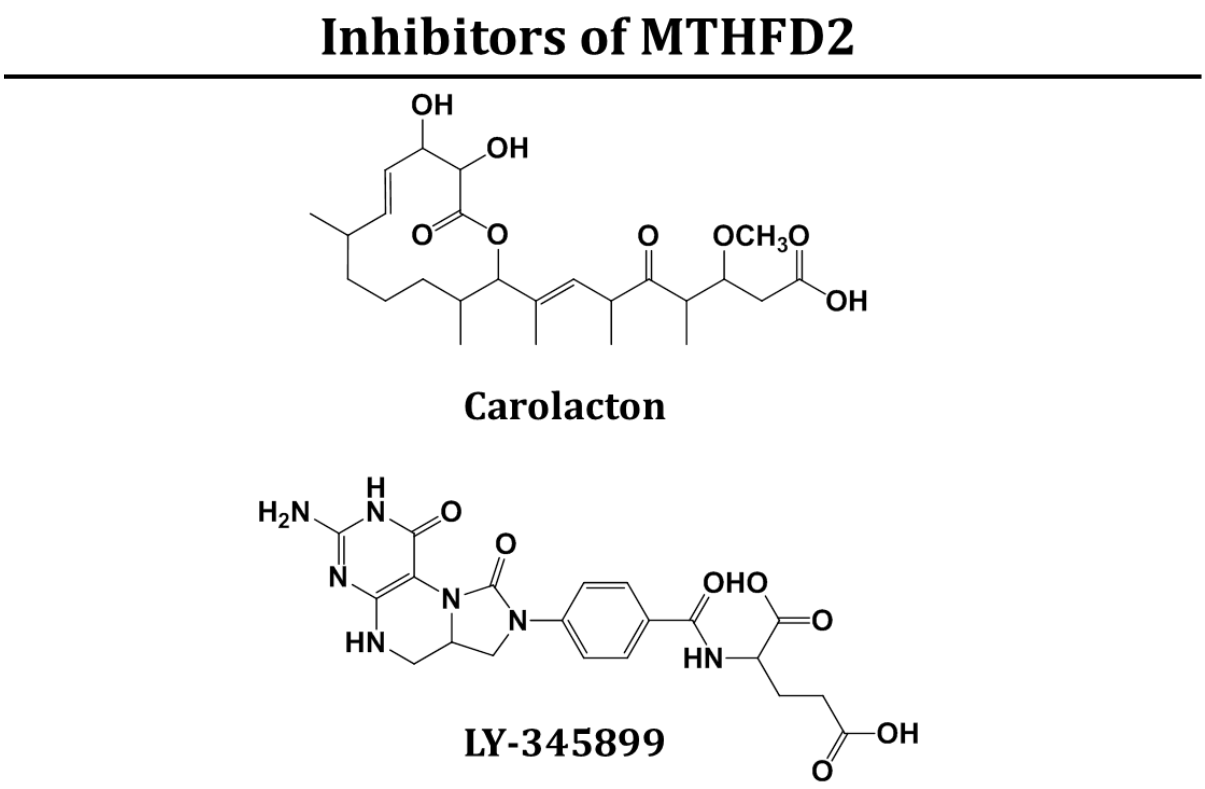

Figure 1.11 Inhibitors of MTHFD2. Carolacton is a macrolide keto-carboxylic acid produced by the myxobacterium *Sorangium cellulosum* that inhibits *Streptococcus mutans* biofilm formation as well as MTHFD2 and the bacterial ortholog FoID, but is rapidly pumped out of human tumor cells. LY-345899 is an Eli Lilly compound that potently inhibits MTHFD2 *in vitro*, but is unable to cross the plasma membrane.

NADPH/$NADP^+$ ratio to ensure cellular survival under hypoxia (Ye et al., 2014), therapeutic targeting of SHMT2 would be particularly tumor-selective against hypoxic Myc-transformed tumors which are resistant to other treatment modalities such as radiation (Horsman and Overgaard, 2016).

Moreover, overexpression of SHMT2 in general is associated with poor prognosis in a variety of cancers including breast cancer (Yin, 2015; Zhang et al., 2016), pancreatic cancer (Noguchi et al., 2018), glioma (Wu et al., 2017), and cholangiocarcinoma (Ning et al., 2018). This suggests that SHMT2 is a highly promising drug target.

Initial efforts to generate small-molecule inhibitors of SHMT focused on herbicidal pyrazolopyran compounds described as inhibitors of plant SHMT (Witschel et al., 2013) (**Figure 1.12).** Optimization of these compounds first yielded molecules with antimalarial activity (Witschel et al., 2015) (**Figure 1.12**). Although potent inhibitors of *Plasmodium falciparum* SHMT *in vitro* (submicromolar IC_{50} values), these compounds suffered from extraordinarily poor pharmacokinetics and their lack of stability rendered them unsuitable for further evaluation (Witschel et al., 2015). Molecules of this series were initially tested against human lung cancer cells (Marani et al., 2016), which yielded poor potency (IC_{50} values in the double-digit micromolar range) with preferential inhibition of SHMT1 over SHMT2. As most cancer cells primarily derive the C1 units necessary for cytosolic purine and thymidylate biosynthesis from the mitochondrial pathway (i.e. from SHMT2) (Ducker et al., 2016) rather than from SHMT1, it is likely that the therapeutic inefficacy of these compounds stemmed at least partially from their preferential inhibition of the latter enzyme Although impractical for targeting human tumor cells in their then-current forms, the herbicidal pyrazolopyran compounds were later optimized for activity against human SHMT1 and SHMT2 (Rabinowitz et al., 2018) (**Figure 1.12**). The first

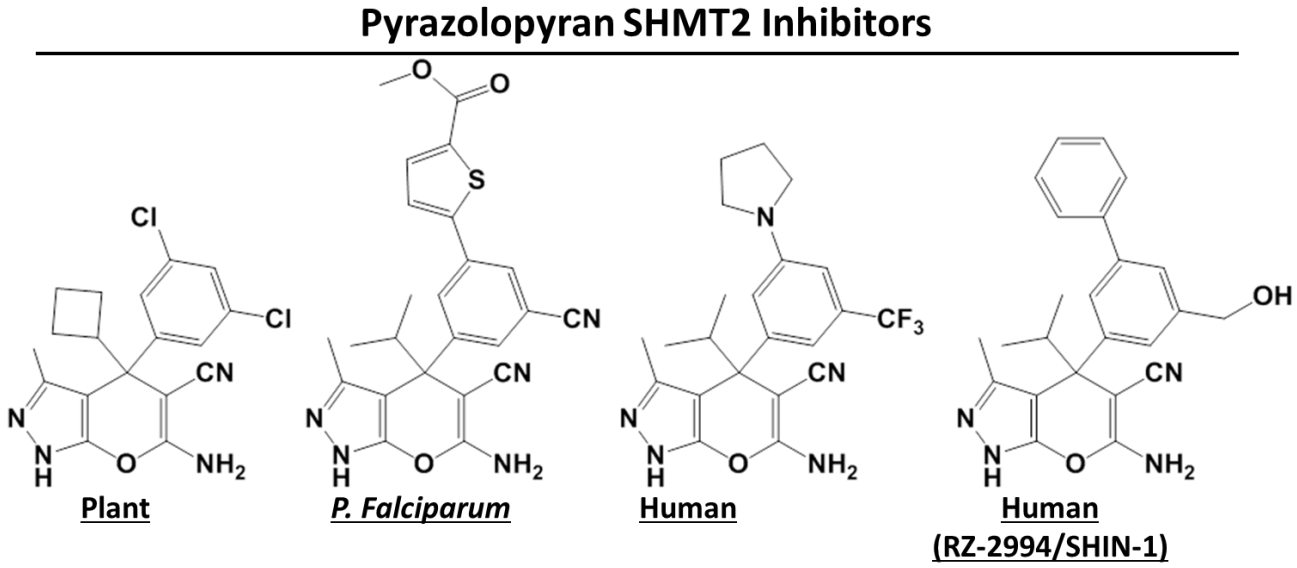

Figure 1.12 Pyrazolopyran Inhibitors of SHMT2. Pyrazolopyran inhibitors were initially described as herbicidal inhibitors of plant SHMT2 (left) and optimized for inhibition of *Plasmodium falciparum* and human SHMT2.

study using these optimized compounds (Ma et al., 2017) identified another pyrazolopyran (RZ-2994) as an extremely potent inhibitor of both human SHMT1 and SHMT2 (IC_{50} values of 5 and 13 nM against isolated SHMT1 and SHMT2, respectively). Moreover, RZ-2994 was significantly more potent against human cells (IC_{50} value in the low single-digit micromolar range against T effector cells) than the non-optimized pyrazolopyran compounds, suggesting potential therapeutic efficacy. Although not an analog of folic acid, a crystal structure of a prazolopyran compound in complex with SHMT2 (Ducker et al., 2017) revealed that these compounds bound at the folate binding site of SHMT2.

The first studies directly assessing these optimized pyrazolopyran SHMT inhibitors against human tumor cell lines were performed by Ducker, Rabinowitz, and colleagues (Ducker et al., 2017). Against wild-type (WT) HCT116 colon cancer cells, RZ-2994 (i.e. serine hydroxymethyltransferase inhibitor 1 – SHIN1) featured sub-micromolar potency (IC_{50} value of 870 nM) with complete rescue by formate and glycine, suggesting efficacy due to on-target inhibition of SHMT1 and SHMT2. Moreover, the IC_{50} value for SHIN1 with SHMT2 KO HCT116 cells decreased by nearly two orders of magnitude to 10 nM (due to potent inhibition of SHMT1), whereas the IC_{50} in SHMT1 KO cells was indistinguishable from that in WT cells. This confirms that the efficacy of the compound was limited by inhibition of SHMT2. Notably, the enhanced potency of SHIN1 in 8988T pancreatic cancer cells and diffuse large B-cell lymphoma revealed distinct metabolic vulnerabilities of these cancer types that could be exploited by SHMT1 and SHMT2 inhibition. The former cell line featured intrinsic defects in mitochondrial C1 metabolism, meaning cells were overly reliant on SHMT1 (the more robust target of SHIN1) for C1 units. In contrast, the latter cell lines were shown to have intrinsic defects in glycine uptake, meaning they were overly reliant on glycine synthesis from serine by

SHMT1 and SHMT2. Moreover, the addition of formate to these cells did not rescue the effects of SHIN1 as it had in HCT116 cells, but instead potentiated SHIN1 efficacy. Cytotoxicity in these cells, then, was due not to C1 unit depletion, but glycine deficiency exacerbated by excess formate, which drives the SHMT reaction in the glycine-consuming direction. Despite the promising effects *in vitro* of SHIN1, it featured poor *in vivo* pharmacokinetics with a lack of *in vivo* antitumor efficacy, likely due to microsomal inactivation. Pyrazolopyran inhibitors of SHMT1 and SHMT2 like SHIN1, while potent *in vitro* and useful as tools for interrogation of C1 metabolism, are not currently candidates for further clinical development.

1.5.3 Concurrent Targeting of Cytosolic One-Carbon Metabolism: Strategies for Optimal Drug Design

While SHMT2 and MTHFD2 are unequivocally associated with the oncogenic phenotype in a variety of cancers, CRISPR/Cas9 KO of either enzyme results in viable and tumorigenic (albeit slower-growing) cells under nutrient-rich conditions due to compensation by the cytosolic isoform, SHMT1 which reverses flux (i.e. serine to glycine) when SHMT2 is lost (Ducker et al., 2016). Therefore, an ideal drug would, in addition to inhibiting SHMT2/MTHFD2, also inhibit SHMT1 to prevent cellular compensation. Moreover, although the compensatory flux through SHMT1 provides sufficient 10-formylTHF to ensure a subsistence level of purine biosynthesis, formate-rescuable elevations in AICAR (Ducker et al., 2016) persist in SHMT2 KO cells and confirm that the cytosolic C1 pools remain depleted. As cytosolic depletion of 10-formylTHF in particular would diminish competition for antifolate binding at both GARFTase and AICARFTase, direct inhibition of these enzymes by an inhibitor of mitochondrial C1 metabolism would likely be highly synergistic.Therefore, the ideal agent would dual-target both mitochondrial and cytosolic C1 metabolism, the former at SHMT2 and/or MTHFD2 and the

latter at SHMT1 and the purine biosynthetic enzymes GARFTase and AICARFTase. Moreover, due to the more tumor selective function and distribution of PCFT versus RFC (discussed previously in section 1.3.2), it would be advantageous to feature selective uptake by PCFT.

CHAPTER 2- DESIGN, SYNTHESIS, AND VALIDATION OF NOVEL 5-SUBSTITUTED PYRROLO[3,2-*d*]PYRIMIDINES DUAL-TARGETING CYTOSOLIC AND MITOCHONDRIAL ONE-CARBON METABOLISM

2.1 Introduction

As existing inhibitors of MTHFD2 and SHMT2 proved insufficient for clinical use (as discussed in section 1.5.1 and 1.5.2), these structures could not be used as drug design scaffolds and the development of entirely novel drugs was necessary. Moreover, for optimal antitumor efficacy (as discussed in section 1.5.3), these agents would have to simultaneously target SHMT2/MTHFD2, SHMT1, and GARFTase/AICARFTase and ideally, they would also be selectively transported by PCFT versus RFC.

In this chapter, we describe the rational design and synthesis of a series of 5-substituted pyrrolo[3,2-*d*]pyrimidine analogs (**Figure 2.1**) with potent inhibition of SHMT2, SHMT1, and GARFTase/AICARFTase as demonstrated both through targeted metabolomics in several human tumor cell lines (H460 – large cell lung carcinoma, HCT116 – colon adenocarcinoma, and MIA PaCa-2 – pancreatic adenocarcinoma), as well as in cell-free enzyme assays with recombinant enzymes. Our unprecedented results establish the lead molecules of this series **AGF291** and **AGF347** as "first-in-class" multitargeted inhibitors of mitochondrial and cytosolic C1 metabolism with *bona fide in vivo* efficacy established in a MIA PaCa-2 tumor xenograft model in severe combined immunodeficient (SCID) mice. The work described in this chapter has been submitted for publication.

2.2 Materials and Methods

2.2.1 Chemicals

[2,3,3-^{2}H, 98%]L-Serine was purchased from Cambridge Isotope Laboratories, Inc. (Andover, MA). Leucovorin [(6R,S) 5-formylTHF] was provided by the Drug Development

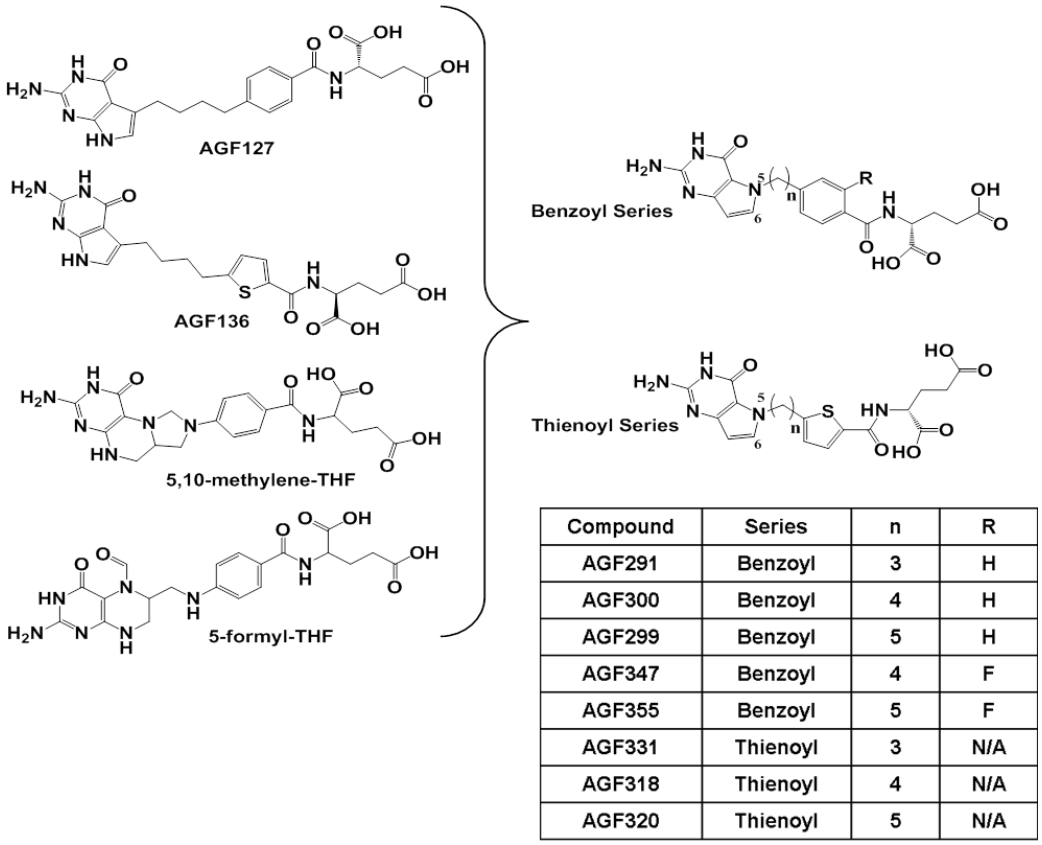

Compound	Series	n	R
AGF291	Benzoyl	3	H
AGF300	Benzoyl	4	H
AGF299	Benzoyl	5	H
AGF347	Benzoyl	4	F
AGF355	Benzoyl	5	F
AGF331	Thienoyl	3	N/A
AGF318	Thienoyl	4	N/A
AGF320	Thienoyl	5	N/A

Figure 2.1 Rational design of novel 5-substituted pyrrolo[3,2-d]pyrimidine benzoyl and thienoyl analogs. Key structural features of the 5-subsituted pyrrolo[2,3-d]pyrimidines AGF127 and AGF136 (28, 32) were merged with the SHMT2 product 5,10-methylene-THF and SHMT2 inhibitor 5-formylTHF (leucovorin) to generate the novel analogs. In the table are summarized key structural features for the various compounds including the bridge lengths (3 -5 carbons), thienoyl or benzoyl side-chains, and for the latter, the 2' ring substituent (F or H). N/A, not applicable.

Branch, National Cancer Institute (Bethesda, MD). **PMX** was purchased from LC Laboratories (Woburn, MA). Gemcitabine (Gemzar) was purchased from Pfizer (New York City, NY). Serine-, glycine- and folate-free RPMI 1640 media was custom-ordered from ThermoFisher (Waltham, MA) and supplemented with tissue-culture grade glycine (ThermoFisher) or serine (Sigma-Aldrich), as needed. **AGF94** was synthesized as previously described (Wang et al., 2011). Novel 5-substituted pyrrolo[3,2-*d*]pyrmidine compounds were synthesized by Dr. Aleem Gangjee (Duquesne University) and his students.

2.2.2 Cell Culture and Proliferation/Protection Assays

The HCT116 cell lines including the SHMT1, SHMT2, and MTHFD2 KO cells were a generous gift of Drs. Gregory Ducker (University of Utah) and Joshua Rabinowitz (Princeton University) and were previously described (Ducker et al., 2016; Ducker et al., 2017). The H460 cell line was obtained from the American Type Culture Collection (Manassas, VA), whereas the MIA PaCa-2 cells were provided by Dr. Yubin Ge (Karmanos Cancer Institute). Cell lines were verified by short tandem repeat analysis by Genetica DNA Laboratories (Burlington, NC). MTXRIIOua^{R}2-4 (i.e. R2) Chinese hamster ovary (CHO) cells were generously provided by Dr. Wayne Flintoff (University of Western Ontario) (Flintoff et al., 1976). From this parental R2 cell line, human RFC and PCFT were individually transfected to generate the isogenic CHO cell lines designated PC43-10 (RFC) and R2/PCFT4 (PCFT) (Deng et al., 2008; Deng et al., 2009; Wong et al., 1995). Human tumor cell lines were cultured in folate-free RPMI supplemented with 10% dialyzed fetal bovine serum (Sigma-Aldrich), 1% penicillin/streptomycin solution, 2 mM L-glutamine, and 25 nM leucovorin (approximating human serum folate levels (Laposata, 2019)) in a humidified atmosphere at 37°C in the presence of 5% CO_2 and 95% air. The CHO cell lines were cultured in α-minimal essential medium (αMEM) supplemented with 10% bovine

calf serum, 1% penicillin/streptomycin solution, and 2 mM L-glutamine. The transfected CHO cell lines (i.e. R2/PCFT4 and PC43-10) were maintained under continuous selection with 1 mg/ml of G418.

For proliferation assays with the CHO cell lines, cells were treated with the inhibitors (0-1 μM) in a 96-well plate (seeding density of 2000 cells/well) in *glycine-free, nucleoside-free* folate-free RPMI supplemented with 10% dialyzed fetal bovine serum, 1% penicillin/streptomycin, 2 mM L-glutamine, and 25 nM leucovorin (final volume 200 μL) over a 96 hour incubation period at 37^{o}C with 5% CO_2. The inhibitors were dissolved in DMSO; an equivalent amount of DMSO was added to the control (no addition) samples. To quantify viable cells, the media was removed and plates were washed once with 100 μL Dulbecco's phosphate-buffered saline (PBS), after which 100 μL PBS and 20 μL Cell Titer-blue reagent (Promega) were added. Relative cell numbers were proportional to the fluorescence measured with a fluorescence plate reader (590 nm emission, 560 nm excitation). Background fluorescence (i.e. that from cell-free wells treated with Cell Titer-blue) was subtracted and these corrected values were normalized to results for cells treated in an identical manner without inhibitors. IC_{50} values, corresponding to the drug concentrations that inhibit growth by 50% relative to untreated controls, were generated by fitting a 4-parameter logistic regression in Excel.

For proliferation assays of the HCT116, H460, and MIA PaCa-2 tumor cell lines, the cells were plated in 96-well plates in an identical manner to that in the CHO experiments, except that the maximal drug concentration was increased to 10 μM. For the HCT116 SHMT2 KO cells, glycine (130 μM) was included as these cells are glycine auxotrophs (Ducker et al., 2016).

Glycine/nucleoside protection experiments in CHO and human tumor cell lines were performed in folate- and glycine-free RPMI 1640 with 10% dialyzed fetal bovine serum and

supplemented with 25 nM leucovorin without additions, or in the presence of adenosine (60 μM), thymidine (10 μM), glycine (130 μM) and/or 5-aminoimidazole-4-carboxamide (AICA) (320 μM). Growth of metabolite-treated cells was normalized to controls treated with metabolites and vehicle (i.e., DMSO) both singly and in combination. Treatments with all metabolites were performed in parallel on the same plate for a given drug.

2.2.3 Generation of H460 SHMT2 knockdown (H460 SHMT2 KD) cell line

H460 cells were seeded (2 x 10^5 cells/well) in 24 well plates containing 1 ml of culture medium (i.e. folate-free RPMI 1640 supplemented with 10% dialyzed fetal bovine serum, 1% penicillin/streptomycin, 2 mM L-glutamine, and 25 nM leucovorin). Cells were treated with 4 μg/ml polybrene and 10^5 transducing units of MISSION Lentiviral particles (Sigma-Aldrich) containing shRNA targeting SHMT2 (TRCN0000034805). An additional well contained H460 cells without shRNA particles. After 24 h, the media was replaced with fresh culture media including 2 μg/ml puromycin (Wilson et al., 2016) as a selection marker. Once cells were confluent (and non-transduced cells had died), cells were harvested, passaged 3-4 times, and assayed by reverse transcriptase – polymerase chain reaction (RT-PCR) for SHMT2 expression relative to that in NTC H460 cells (Golani et al., 2016). To isolate single clones, cells were plated in 100 mm dishes (200 cells/dish) in the presence of 2 μg/ml puromycin. Colonies were isolated, and expanded and clonal cultures were assayed for SHMT2 KD via RT-PCR. SHMT2 KD was confirmed via Western blotting (**Figure 2.2**).

2.2.4 RT-PCR

Cells were harvested from either 60 mm dishes or T25 flasks at ~80% confluence and RNAs extracted using TRIzol reagent (Invitrogen, Carlsbad, CA). cDNAs were synthesized with

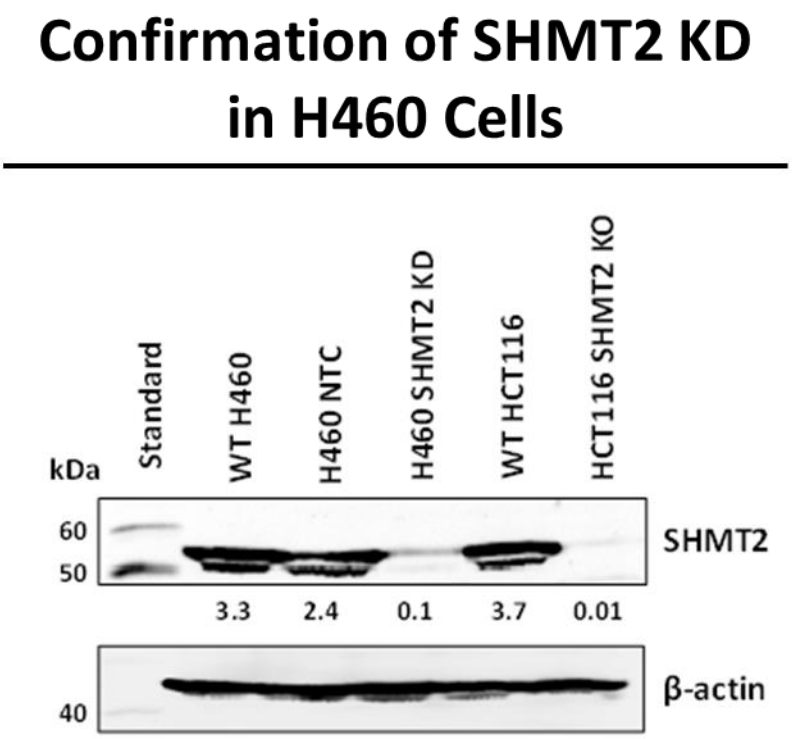

Figure 2.2 Western Blot confirming knockdown of SHMT2 in H460 cells Whole-cell lysates of wild-type (WT), non-targeted control shRNA-transduced (NTC), and clonal SHMT2 knockdown (SHMT2 KD) H460 cells, along with HCT116 WT and SHMT2 CRISPR/Cas9 knockout (KO) cells were resolved on 10% polyacrylamide gel with SDS and probed with monoclonal rabbit anti-SHMT2 antibody (#12762; Cell Signaling Technology, Danvers, MA). The blot was stripped and reprobed with mouse anti-β-actin antibody (Sigma-Aldrich) as a loading control. Experimental details are described in section 2.2.3 and 2.2.5. The blots were scanned with an Odyssey infrared imaging system (LICOR Biosciences). Densitometry analysis (values given are SHMT2 band intensities normalized to β-actin band intensities) revealed SHMT2 protein expression of H460 SHMT2 KD to be 5.3% of that of H460 NTC, and HCT116 SHMT2 KO expression to be <1% of that of HCT116 WT.

random hexamers, MuLV reverse transcriptase, and RNase inhibitor (Applied Biosystems, Waltham, MA), and purified with a QIAquick PCR Purification Kit (QIAGEN, Valencia, CA).Quantitative RT-PCR was performed using a Roche LightCycler 480 (Roche Diagnostics, Indianapolis, IN) with gene-specific primers and Universal Probe Library probes (SHMT2-#83, RFC-#32, PCFT-#89, FRα-#65 (Roche Diagnostics)). Transcript levels were normalized to transcript levels of β-actin and glyceraldehyde-3-phosphate dehydrogenase (GAPDH).

2.2.5 Gel Electrophoresis and Western Blots

H460 WT, H460 NTC, H460 SHMT2 KD, HCT116 WT, and HCT116 SHMT2 KO cell lines were plated (1 x 10^6 cells/dish) in 60 mm dishes and harvested when the cells were ~80% confluent. Cells were disrupted by sonication with cell debris removed by centrifugation. The soluble cell fraction was assayed for protein concentration (Lowry et al., 1951) and equal amounts of protein (37 µg) from each sample were electrophoresed on 10% polyacrylamide gels with SDS (Laemmli, 1970) and transferred to polyvinylidene difluoride membranes (ThermoFisher) (Matsudaira, 1987). To detect SHMT2, membranes were incubated for 72 hours with rabbit anti-SHMT2 primary antibody (#12762 (Ducker et al., 2016); Cell Signaling Technology, Danvers, MA). The blots were developed by incubating in IRDye800CW-conjugated goat anti-rabbit IgG secondary antibody (LICOR Biosciences, Omaha, NE) for 90 min and scanning with an Odyssey infrared imaging system (LICOR Biosciences). Protein loading was normalized to β-actin using anti-β-actin mouse antibody (Sigma-Aldrich).

2.2.6 Targeted Metabolomics

Targeted metabolomics was performed essentially as previously described (Ducker et al., 2016; Ducker et al., 2017). Briefly, cells (H460, HCT116, MIA PaCa-2) (1 x 10^6 cells /dish for

vehicle-treated samples, 1.5 x 10^6 cells/dish for drug-treated samples) were seeded in triplicate 60 mm dishes in 5 ml of folate-free RPMI (contains glycine and unlabeled serine) supplemented with 10% dialyzed fetal bovine serum, 1% penicillin/streptomycin, 2 mM L-glutamine, and 25 nM leucovorin. The cells were allowed to adhere for 24 h. The media were aspirated and replaced with culture media (contains 25 nM leucovorin, glycine, and unlabeled serine) and 10 µM **AGF291**, **AGF320** or **AGF347**, or a comparable volume of vehicle (DMSO) (with or without 1 mM formate (final concentration)). After 16 h, the cells were washed with PBS (3x), the media were replaced with folate- and serine-free culture media (containing glycine) supplemented with 10% dialyzed fetal bovine serine, 25 nM leucovorin, and [2,3,3-^{2}H]-serine (250 µM), including 10 µM drug or DMSO vehicle. The cells were incubated for 24 h. All incubations were at 37^{o}C with 5% CO_2. The media were aspirated, and cells were washed (3x) rapidly (< 30 s) with 5 mL ice-cold PBS; metabolism was quickly quenched with methanol:water (80:20) at -80^{o}C. Cells were allowed to rock on dry ice for 10 min to cover the entire dish with 80:20 methanol:water (at -80^{o}C), then harvested by scraping and pipetting into 1.5 mL Eppendorf tubes. The tubes were centrifuged to fully extract metabolites into the methanol:water supernatant. The protein pellet was used for normalization. The supernatants were collected and analyzed by reverse-phase ion-pairing chromatography coupled with negative-mode electrospray-ionization high-resolution mass spectrometry on a stand-alone Orbitrap (ThermoFisher Exactive) (Lu et al., 2010). The metabolites were identified and quantified from collected mass spectra using MAVEN software. Raw metabolite values were adjusted to correct for normal ion distributions and normalized to total proteins from the post-extraction pellet by solubilizing with 0.5 N NaOH and using the Folin-phenol protein method (Lowry et al., 1951). Values below the limit of detection were assigned a value of 100 for normalization. Results for

drug-treated and SHMT2 KD cells were normalized to vehicle-treated WT ± formate or NTC ± formate samples, as appropriate. Drug treatment and metabolite extraction were done in our lab while Drs. Gregory Ducker (Princeton University/University of Utah) and Drs. Jing Li and Xun Bao (Karmanos Cancer Institute) performed the liquid chromatography – mass spectrometry (LC-MS) analysis.

2.2.7 Enzyme Expression and Purification

His-GARFTase was expressed and purified as described previously (Deis et al., 2016). To express full-length human ATIC with an N-terminal, cleavable hexahistidine tag, ATIC cDNA was cloned into pHis-parallel via Gibson assembly with subsequent confirmation by DNA sequencing prior to enzymatic studies (Gibson et al., 2009). The resulting plasmid, pSD001, was transformed and expressed in Rosetta (DE3) pLysS cells. Cultures (1 L) were grown in LB media containing 100 μg/mL ampicillin and 34 μg/mL chloramphenicol at 37°C until OD_{600} reached 0.6. Expression was induced with the addition of 500 μM isopropyl *β*-D-1-thiogalactopyranoside (IPTG) and incubated at 20°C for 16-18 h. Cultures were pelleted and resuspended in 40 mL 25 mM Tris pH 7.5, 300 mM NaCl, 5 mM *β*-mercaptoethanol (*β*-Me), 10 mM $CaCl_2$, 10 mM $MgCl_2$, 40 mg lysozyme, and 8 U DNAse I (Sigma) before cell lysis by emulsification. His-ATIC was purified from the lysate by immobilized metal affinity chromatography over a 4 mL nickel-nitrilo-triacetic acid column (Gold Biotechnology). The lysate was passed over the 4 mL column, washed with 5 column volumes (CV) of 25 mM Tris pH 7.5, 300 mM NaCl, 10 mM imidazole, and 5 mM *β*-Me (wash buffer) and 5 CV of wash buffer with 25 mM imidazole. Protein was eluted with 5 CV (1 CV fractions) of elution buffer containing components of wash buffer and 300 mM imidazole. Purity of samples was checked by SDS PAGE. Samples were further purified on ÄKTA FPLC (GE Healthcare) via Superdex

200 16/60 (GE Healthcare) column, equilibrated with 20 mM Tris pH 7.5, 150 mM NaCl, 50 mM KCl, 5 mM EDTA, and 5 mM dithiothreitol. His-ATIC was stored at 150 μM at 4°C in this buffer for up to six months, or at 100 μM with 20% glycerol at -80°C for long-term storage. Plasmids to express human cytosolic SHMT1 (residues 7-478, Uniprot ID P34896) and mitochondrial SHMT2 (residues 42-504, Uniprot ID 34897), both with cleavable N-terminal His_6-tags, were inserted into pHis-parallel and expressed in Rosetta^{TM} (DE3) pLysS cells. Expression was induced with 1 mM IPTG when the OD_{600} = 0.6, and induction continued at 20° C for 18-20 hours before cell harvesting. Cells were lysed by emulsification and nickel-nitrilo-triacetic acid chromatography (Gold Biotechnology) was used for initial purification, as described for His-ATIC. PLP was added in 3-fold molar excess to SHMT samples and allowed to incubate for 24 h. Size exclusion chromatography was employed using on a Superdex 200 16/60 column (GE Healthcare) while monitoring absorbance at 435 nm for final purification of proteins with PLP bound. SHMT enzymes were stored in 20 mM sodium phosphate buffer pH 7.5, 100 mM potassium chloride, 0.2 mM EDTA, and 5 mM β-Me. For MTHFD2 expression, cDNA encoding the bifunctional human mitochondrial MTHFD2 (residues 36-333, Uniprot ID P13995) was inserted into a pHis-parallel vector for expression in Rosetta^{TM} (DE3)pLysS cells as a fusion protein with a cleavable N-terminal His_6-tag. After cell lysis by emulsification, nickel nitrilo-triacetic acid chromatography and size exclusion chromatography (Superdex 200 16/60 column) were used for purification, as described for His-ATIC. Purified His-MTHFD2 was stored in 50 mM Tris buffer pH 7.5, 250 mM sodium chloride, 5% glycerol, and 0.5 mM TCEP. Expression and purification of these recombinant human enzymes were carried out by Dr. Charles Dann III (Indiana University) and his graduate students (Jennifer Wong and Jade Katinas).

2.2.8 *In Vitro* Enzymatic Assays and K_i Determinations

For *in vitro* enzymatic assays of AICARFTase with 5-substituted pyrrolo[3,2-*d*]pyrimidine inhibitors, His-ATIC, containing an N-terminal cleavable hexahistidine tag, was purified. AICARFTase catalytic activity was measured by monitoring the formation of THF spectrophotometrically from 10-formylTHF in the presence of various concentrations of inhibitor (Shih et al., 1997). Assays included a final concentration of 50 μM 10-formylTHF, 100 nM ATIC, and a range of inhibitors in 32.6 mM Tris-HCl pH 7.4, 25 mM KCl, and 5 mM *β*-Me. Reactions were pre-incubated at 25°C in a UV-transparent 96-well plate (Costar 3635) for 90 seconds, with measurements at 298 nm every 6 seconds. Reactions were then initiated by adding 10 μL 500 μM AICAR or buffer (control wells) for a final reaction volume of 100 μL. Measurements were recorded in triplicate at 298 nm every 6 seconds over 10 min using a BioTek Synergy Neo2 Plate Reader. To determine the initial rate for each inhibitor concentration, absorbances of the preincubation period were averaged and subtracted from all measurements in that well. Initial rate changes in absorbance at 298 nm were determined for regions of linear absorbance increases in all replicates. Initial slopes were graphed against inhibitor concentrations and fit to a hyperbolic curve [$y = (-a*x/(IC_{50} + x)) + b$, where **"a"** is the amplitude and **"b"** is the y-intercept] to calculate the IC_{50} value for each compound (GraphPad Prism 7.0). The K_i was then calculated from the IC_{50} value [$K_i = IC_{50}/([S]/K_M+1)$], using K_m and substrate values for 10-formylTHF. The calculated K_m for 10-formylTHF with His-ATIC, determined as a function of initial velocity versus 10-formylTHF concentration, was 100 μM.

In vitro enzymatic assays of GARFTase with 5-substituted pyrrolo[3,2-*d*]pyrimidine inhibitors were carried out with His-GARFTase containing an N-terminal cleavable

hexahistidine tag. GARFTase catalytic activity was measured by monitoring the formation of THF spectrophotometrically from 10-formylTHF in the presence of a range of inhibitor concentrations. Assays included final concentrations of 40 μM 10-formylTHF, 50 nM GARFTase, and a range of inhibitors in 0.1 M HEPES ((4-(2-hydroxyethyl)-1-piperazineethanesulfonic acid)-buffered saline) at pH 7.5 (Wang et al., 2015). Reactions were pre-incubated at 37°C in a UV-transparent 96-well plate (Costar) for 90 seconds, with measurements at 298 nm every 5 seconds. Reactions were then initiated by adding 10 μL 150 μM α,β-GAR or buffer (control wells) for a final reaction volume of 100 μL. Measurements were recorded at 298 nm every 5 seconds for 15 min using a BioTek Synergy Neo2 Plate Reader in triplicate. Procedures for data fitting and determination of K_i values for His-GARFTase were as described for His-ATIC. The calculated K_m for 10-formylTHF with His-GARFTase, determined as a function of initial velocity versus 10-formylTHF concentration, was 84.8 μM.

In vitro activities of His-SHMT1 and His-SHMT2 were assayed by a coupled reaction with His-MTHFD2 in 200-fold molar excess, and NADH production was monitored by fluorescence at 470 nm with excitation at 360 nm (Synergy Neo2 Biotek plate reader) using a black well, black bottom 96-well plate (Corning #3916) in triplicate. The reaction volume was 100 μL with final concentrations of 50 nM SHMT enzyme, 10 μM MTHFD2, 50 μM THF, 2.5 mM NAD^+, and 20 mM serine. Serine was added to initiate the reaction and data were acquired every 19 seconds over 15 min. Linear initial velocities were determined and data fitting, IC50 and Ki calculations were performed as described for His-ATIC. The calculated K_m for THF with His-SMHT1 and His-SHMT2, determined as a function of initial velocity versus THF concentration, are 62.8 μM and 108 μM, respectively.

To confirm that MTHFD2 was not inhibited by the AGF molecules, MTHFD2 activity was evaluated with an NAD(P)H-Glo^{TM} Detection System Kit (Promega, Ref G9061). Final concentrations for the reactions were 100 nM MTHFD2, 100 μM NAD^+, 100 μM methyleneTHF, with reaction initiation with NAD^+. Reactions were performed for 10 min at room temperature. To stop the reaction, the temperature was increased to 100 ºC for 30 min and 1 μL of 1 M hydrochloric acid was added. Thereafter, 1 μL of 1 M sodium hydroxide was added to neutralize the acid. From this reaction, 12.5 μL was transferred to each of 3 wells of a white 96-well plate (Corning #3917) containing 12.5 μL luciferase reagents (as specified by the kit). Luminescence was allowed to develop in the dark for 55 min, and samples were read with a Synergy Neo2 Biotek plate reader using the Biotek Lum 1536 filter cube for 10 min. Luminescence data for the last 5 min were averaged for final endpoint measurements. These experiments were performed by Dr. Charles Dann III (Indiana University) and his graduate students, Jennifer Wong and Jade Katinas.

2.2.9 *In Vivo* Efficacy Trial with MIA PaCa-2 Tumor Xenografts

Methods for *in vivo* maintenance of MIA PaCa-2 tumor xenografts and drug efficacy evaluations are analogous to those previously described (Cherian et al., 2013; Golani et al., 2016; Ravindra et al., 2018; Wang et al., 2010; Wang et al., 2011). MIA PaCa-2 human pancreatic cancer cells (5 x 10^6 cells/flank) were bilaterally implanted subcutaneously with tumor fragments (30-60 mg) with a 12-gauge trocar in female NCR SCID mice (NCI Animal Production Program). The mice were 9 and 11 weeks old on day 0 (tumor implant) with an average body weight of 19.8 g and 20.2 g for the **AGF291** and **AGF347** trials, respectively. One cohort of mice was maintained on a folate-deficient diet from Harlan-Teklad (TD.00434) starting 14 days before subcutaneous tumor implant to ensure serum folate levels would approximate those of

humans. A separate cohort of mice was fed a folate-replete control diet from Lab Diet (5021). Mice were supplied with food and water *ad libitum*. Serum folate concentrations were monitored prior to tumor implant and post study by *Lactobacillus casei* bioassay (Varela-Moreiras and Selhub, 1992). The mice within each group (folate-deficient and standard diet) were pooled before non-selective distribution to each group's respective treatment and control arms. Chemotherapy was begun 1 or 3 days (for **AGF347** and **AGF291**, respectively) post-tumor implantation with **AGF291** (7.75 mg/kg/injection every 6 days; total dose of 23.25 mg/kg), **AGF347** (15 mg/kg/injection every 2 days; total dose of 120 mg/kg), or gemcitabine (120 mg/kg/injection every 4 days; total dose of 480 mg/kg). The inhibitors were dissolved in 5% ethanol (v/v), 1% Tween-80 (v/v), and 0.5% $NaHCO_3$ and were administered intravenously (IV - 0.2 ml/injection). The mice were weighed and tumors were measured with a caliper two-to-three times weekly; mice were euthanized when the cumulative tumor burden reached 1500 mg. Tumor weights were estimated from two-dimensional measurements, where tumor mass (in mg) = $(a \times b^2)/2$, and a and b are the tumor length and width in mm, respectively. The tumor masses from both tumors on each mouse were added together, and the total mass per mouse was used for calculations of anti-tumor activity. Quantitative end-points include: (i) tumor growth delay [T-C, where T is the median time in days required for the treatment group tumors to reach a predetermined size (e.g., 1000 mg), and C is the median time in days for the control group tumors to reach the same size; tumor-free survivors are excluded from these calculations]; and (ii) T/C (in percent) when treatment (T) and control (C) groups for the control groups reached 700 mg in size (exponential growth phase). As appropriate, the median value of each group was determined (including zeros). Mouse weights were monitored as a gauge of drug toxicity.

2.2.10 Statistics

All data shown reflect at least three biological replicates unless noted otherwise (e.g. targeted metabolomics data, which reflect three technical triplicates measured in single experiments). All statistical analyses were performed by Dr. Seongho Kim at the Karmanos Cancer Institute Biostatistics Core. The expression levels were assessed for the normality assumption. The $\log_2$ transformation was used as all values were positive. The statistical tests were carried out using an unpaired t-test. P-values were not adjusted for multiple comparisons.

2.3 Results

2.3.1 Design of Novel 5-substituted Pyrrolo[3,2-*d*]pyrimidines

The lack of any suitable drug design scaffolds for SHMT2 inhibitors led us to design our own molecules. As a design platform, we merged structural features of our previous 5-substituted pyrrolo[2,3-*d*]pyrimidine benzoyl and thienoyl compounds (inhibitors of GARFTase and/or AICARFTase with *in vivo* efficacy) (Mitchell-Ryan et al., 2013; Wang et al., 2015) with those of 5,10-meTHF (SHMT2 product) and 5-formylTHF (leucovorin, an SHMT inhibitor) (Fu et al., 2003) (**Figure 2.1**). We hypothesized that combining the structural characteristics of these different agents would combine their enzyme targets, yielding molecules that would bind and inhibit both SHMT1 and SHMT2, as well as GARFTase and/or AICARFTase. The resulting 5-substituted pyrrolo[3,2-*d*]pyrimidine analogs included 3-5 bridge carbons linked to benzoyl (i.e., **AGF291**, **AGF300,** and **AGF299**) or thienoyl (i.e., **AGF331**, **AGF318**, and **AGF320**) moieties. Based on the reported impact of 2'-fluorine substitutions in increasing the inhibitory potencies of pyrrolo[2,3-*d*]pyrimidine compounds (Ravindra et al., 2018), we designed and synthesized 2'-fluorinated analogs of **AGF300** and **AGF299**, as well (**AGF347** and **AGF355**, respectively) (**Figure 2.1**). The 2'-fluorinated analog of **AGF291**, **AGF359**, was synthesized after these

studies were completed and so, is not presented in this work. Ultimately, we generated 8 analogs (**Figure 2.1**) which advanced to the screening stage.

2.3.2 Screening of Novel 5-Substituted Pyrrolo[3,2-*d*]pyrimidines Yields Three Lead Compounds: AGF291, AGF320, and AGF347

As we reasoned that PCFT-selective uptake would be ideal for any novel antifolates (see section 1.3.2), we initially assessed inhibition by these compounds (from 0 to 1000 nM) toward PCFT-expressing R2/PCFT4 CHO cells and an isogenic CHO subline engineered to express human RFC (PC43-10) (Deng et al., 2008; Deng et al., 2009). Results were compared to those for folate transporter-null R2 CHO cells as a negative control. IC_{50} values are shown in **Table 2.1** for each of the analogs, along with those for **AGF94** (Wang et al., 2011) and **PMX**. Active compounds (denoting an IC_{50} < 1000 nM) toward R2/PCFT4 and/or PC43-10 cells included **AGF291**, **AGF320**, **AGF331** and **AGF347**, with **AGF291** showing mild preference (~1.6-fold) toward PCFT over RFC. However, this difference was minor compared to **PMX**, which showed a 5-fold preference for PCFT over RFC and **AGF94**, a 6-substituted pyrrolo[2,3-*d*]pyrimidine inhibitor (Wang et al., 2011) which showed ~30-fold selectivity. To confirm the activity of these compounds in human tumor cells, these analogs were further tested in the H460 large cell lung carcinoma, HCT116 colon adenocarcinoma, and MIA PaCa-2 pancreatic adenocarcinoma cell lines, characterized by expression of PCFT and RFC, but not FRα (**Figure 2.3**). IC_{50} values for growth inhibition are in **Table 2.1**. Although there were notable differences in drug sensitivities among the assorted tumor models, **AGF291**, **AGF320** and **AGF347** were consistently the most active of the series and so, were advanced to determinations of the enzyme target(s). We used glycine/nucleoside protection studies (**Figure 2.4 -** see section 2.2.2 for methods) in H460, HCT116, and MIA PaCa-2 cells treated with **AGF291**, **AGF320**, or **AGF347** to identify likely

targeted pathways. The results were compared to those for **AGF94,** an established GARFTase inhibitor (Wang et al., 2011). Adenosine (60 μM) was fully protective up to 10 μM

Table 2.1 IC_{50} values (nM) for antifolate inhibition of CHO and human tumor cell lines.

Compound	Series	n (bridge length)	R	IC_{50} (nM)						
				R2	PC43-10 (RFC)	R2/PCFT4 (PCFT)	HCT116 WT	HCT116 SHMT2 KO	H460	MIA PaCa-2
AGF94	NA	NA	NA	136.1 (3.6)	110.5 (15.6)	3.0 (0.6)	191.0 (62.1)	294.7 (59.1)^	166.5 (59.4)	1924.8 (539.4)
PMX	NA	NA	NA	395.8 (83.6)	124.5 (39.5)	24.1 (5.3)	293.2 (81.5)	333.3 (39.7)	165.2 (59.1)	281.7 (23.9)
AGF291	Benzoyl	3	H	>1000	454.5 (87.2)	282.0 (22.6)	2266.5 (450.4)	108.1 (66.2)^{VVV}	461.1 (163.5)	3664.0 (721.3)
AGF300	Benzoyl	4	H	>1000	>1000	>1000	NA	N/A	NA	NA
AGF299	Benzoyl	5	H	>1000	>1000	>1000	NA	N/A	NA	NA
AGF347	Benzoyl	4	F	>1000	224.0 (17.3)	479.2 (63.7)	437.1 (180.3)	42.0 (18.9)^{VVV}	214.5 (88.1)	1381.0 (182.4)
AGF355	Benzoyl	5	F	>1000	>1000	>1000	NA	N/A	NA	NA
AGF331	Thienoyl	3	NA	>1000	>1000	661.5 (62.6)	2199.5 (817.9)	969.3 (254.4)^{VV}	2367.7 (711.6)	6681.0 (604.6)
AGF318	Thienoyl	4	NA	>1000	>1000	>1000	NA	N/A	NA	NA
AGF320	Thienoyl	5	NA	>1000	>1000	694.0 (56.7)	737.5 (195.7)	116.6 (60.1)^{VV}	573.3 (144.7)	2703.5 (400.3)

Proliferation inhibition assays were performed over 96 hours (as described in section 2.2.2) using the engineered CHO cell lines R2 (folate transporter-null), PC43-10 (expresses RFC only), and R2/PCFT4 (expresses PCFT only), and human tumor cell lines including HCT116 (colon), H460 (lung), and MIA PaCa-2 (pancreatic).Results are shown as mean IC_{50} values (± standard deviation) from at least four biological replicates. IC_{50} values represent the interpolated concentrations of drug at which growth of 50% of cells was inhibited relative to vehicle-treated cells. Series refers to the side chain benzoyl or thienoyl group, whereas the bridge lengths refer to the 3-5 carbons in the side chain. R designates the 2'H or F moiety (see Figure 2.1). For HCT116 SHMT2 KO cells, significant differences in IC_{50} relative to HCT116 WT cells are denoted by ^ (indicating a significant increase) or ^{V} (indicating a significant decrease) with the number of symbols indicating the degree of significance (^ or ^{V} denotes $p<0.05$, ^^ or ^{VV} denotes $p<0.01$, ^^^ or ^{VVV} denotes $p<0.001$).

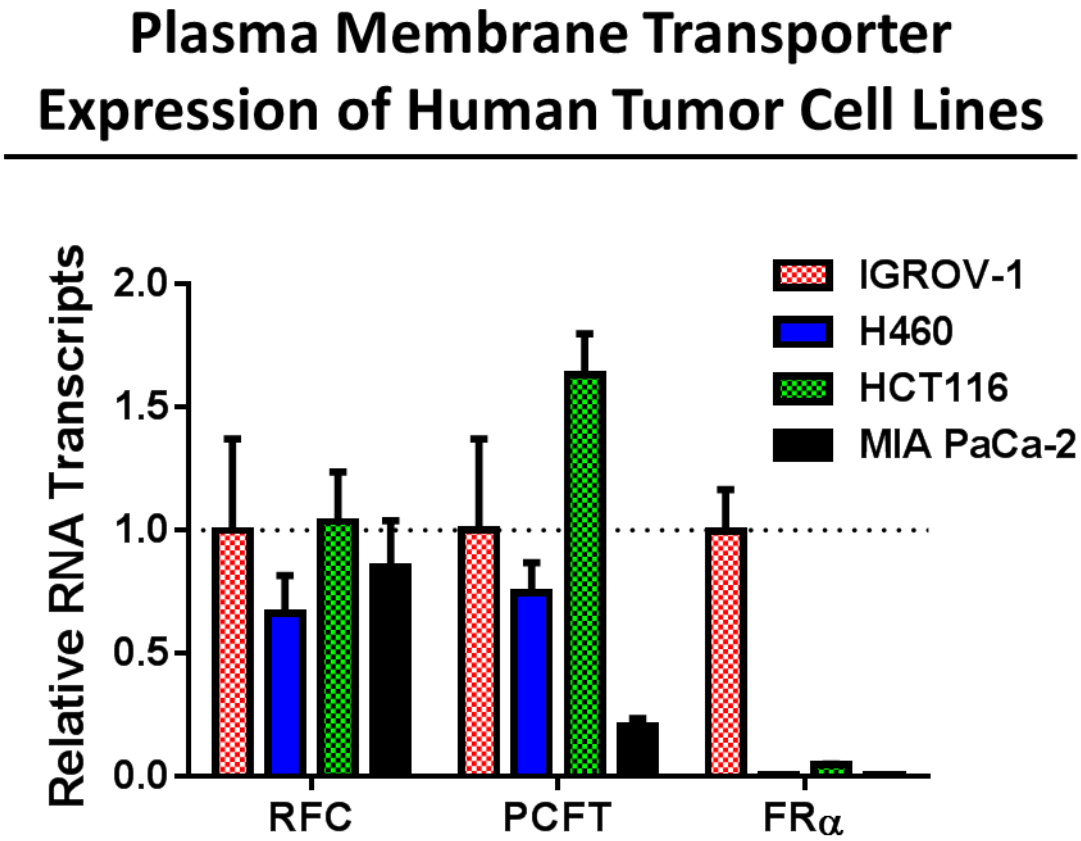

Figure 2.3 Plasma Membrane Transporter Expression of Human Tumor Cell Lines Folate transporter transcript expression of human tumor cell lines by RT-PCR (see section 2.2.4). Transcript levels for RFC, PCFT, and FRα in H460, HCT116 and MIA PaCa-2, and IGROV1 epithelial ovarian carcinoma cells were measured by RT-PCR with results normalized to those of β-actin and GAPDH. All gene expressions are shown relative to those in IGROV-1 cells. The results show represent mean values +/- standard deviations.

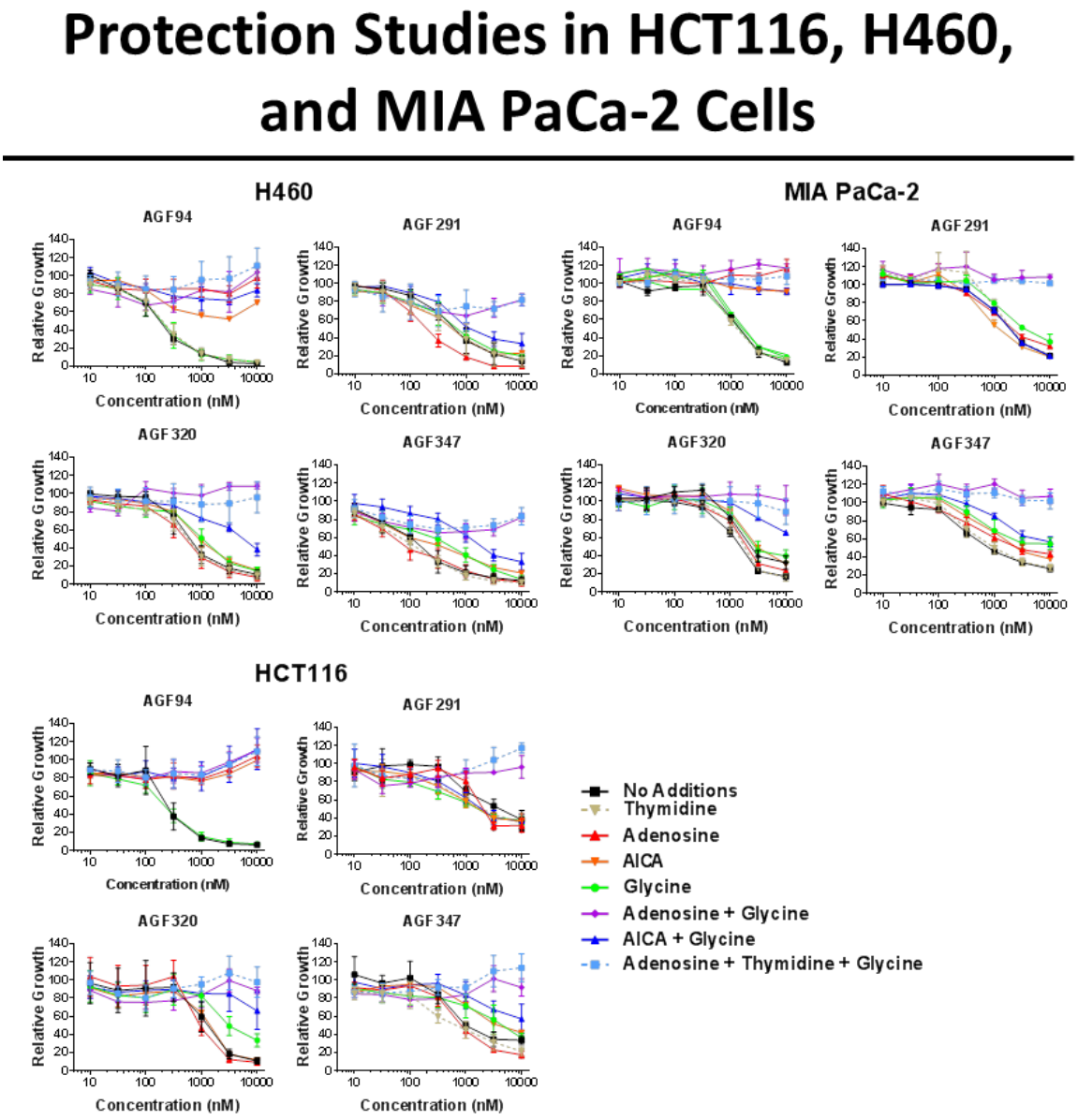

Figure 2.4 Protection Studies in Human Tumor Cell Lines *In vitro* proliferation studies over 96 hours with **AGF291**, **AGF320**, **AGF347,** and **AGF94** (see section 2.2.2) were performed without additions, or in the presence of adenosine (60 µM), 5-aminoimidazole-4-carboxamide (AICA) (320 µM), thymidine (10 µM) and/or glycine (130 µM). The results are presented as mean values ± standard deviations for at least three biological replicates, with growth of cells treated with inhibitor ± metabolite normalized to the growth of cells treated with vehicle (i.e., DMSO) ± metabolite.

AGF94, whereas glycine (130 μM) had no effect (**Figure 2.4**). We also tested the protective effects of AICA (320 μM) which is metabolized to AICAR (AICARFTase substrate), thus circumventing the GARFTase step (**Figure 1.2)** in *de novo* purine biosynthesis (Wang et al., 2011). As AICA was completely protective, GARFTase must be the intracellular target for **AGF94** (Wang et al., 2011). For **AGF291**, **AGF347**, and **AGF320**, however, adenosine alone was NOT fully protective. However, combined adenosine and glycine was substantially protective for all compounds (**Figure 2.4**). These results strongly suggest that these compounds target both mitochondrial C1 metabolism (as KO of either SHMT2 or MTHFD2 induces glycine auxotrophy) (Ducker et al., 2016) and cytosolic *de novo* purine biosynthesis. Thymidine provided no protection from any of the compounds and did not increase the extent of protection by glycine and adenosine, suggesting that TS was not targeted. For some of the analogs, notably **AGF320**, growth inhibition was modestly (and incompletely) reversed by AICA (with glycine) (**Figure 2.4**), suggesting a secondary intracellular target, most likely GARFTase (analogous to **AGF94**). Moreover, the IC_{50} values for **AGF291**, **AGF320**, and **AGF347** were significantly decreased in the HCT116 SHMT2 KO cells relative to the corresponding IC_{50} values in the HCT116 WT cells (**Table 2.1**). These results recapitulated the enhanced potency of the SHIN-1 (**Figure 1.12**) dual SHMT1/2 inhibitor in the HCT116 SHMT2 KO cell line relative to the HCT116 WT cell line (Ducker et al., 2017) and suggested that **AGF291**, **AGF320**, and **AGF347** were inhibiting SHMT1, in addition to SHMT2 and/or MTHFD2. Notably, the IC_{50} value for **AGF94** and **PMX** did NOT decrease in the HCT116 SHMT2 KO cell line relative to the WT, suggesting that the decrease in IC_{50} seen with the novel agents was not due to inhibition of a cytosolic enzyme target. Collectively, these results establish that **AGF291**, **AGF320**, and **AGF347** likely target both mitochondrial and cytosolic C1 metabolism, the former at SHMT2

and/or MTHFD2, and the latter at SHMT1 as well as GARFTase and/or AICARFTase. To further resolve the enzyme targets of **AGF291**, **AGF320**, and **AGF347**, we performed targeted metabolomics in the human tumor cell lines.

2.3.3 Identification of the Mitochondrial Enzyme Target(s) of AGF291, AGF320, and AGF347

As both SHMT2 KO and MTHFD2 KO induce glycine auxotrophy (Ducker et al., 2016), the necessity of glycine to fully abrogate the effects of **AGF291**, **AGF320**, and **AGF347** suggested that we were targeting one of these two mitochondrial C1 metabolism enzymes. To resolve the mitochondrial target, we performed targeted metabolomics (as described in section 2.2.6) on drug-treated cells grown in media containing [2,3,3-^{2}H]-serine. First, we assessed total cellular serine pools and serine isotope distribution (**Figure 2.5**). Consistent with the majority of cancer cells preferentially metabolizing serine through the mitochondrial C1 pathway (versus SHMT1 in the cytosol) (Ducker et al., 2016), SHMT2 KO and MTHFD2 KO (but not SHMT1 KO) induced a ~10-fold increase in serine accumulation in HCT116 cells (**Figure 2.5 – A**). Essentially identical results were noted in H460 cells transduced with SHMT2-targeted shRNA (SHMT2 KD) as compared to NTC H460 cells (**Figure 2.5 – B)**. Notably, drug treatment in both HCT116 and H460 cell lines recapitulated the respective SHMT2 KO or KD (as well as MTHFD2 KO) phenotype. In the MIA PaCa-2 cells (**Figure 2.5 – C**), drug treatment induced a smaller, yet still significant accumulation of serine (~3-fold), perhaps reflecting reduced serine flux overall in this cell line relative to H460 and HCT116 cells. To resolve targeting of SHMT2 or MTHFD2, we analyzed the serine isotope distribution in each cell line. M+3 serine reflects unmetabolized serine (i.e. [2,3,3-^{2}H]-serine - **Figure 2.6**). Catalysis of M+3 serine by SHMT2

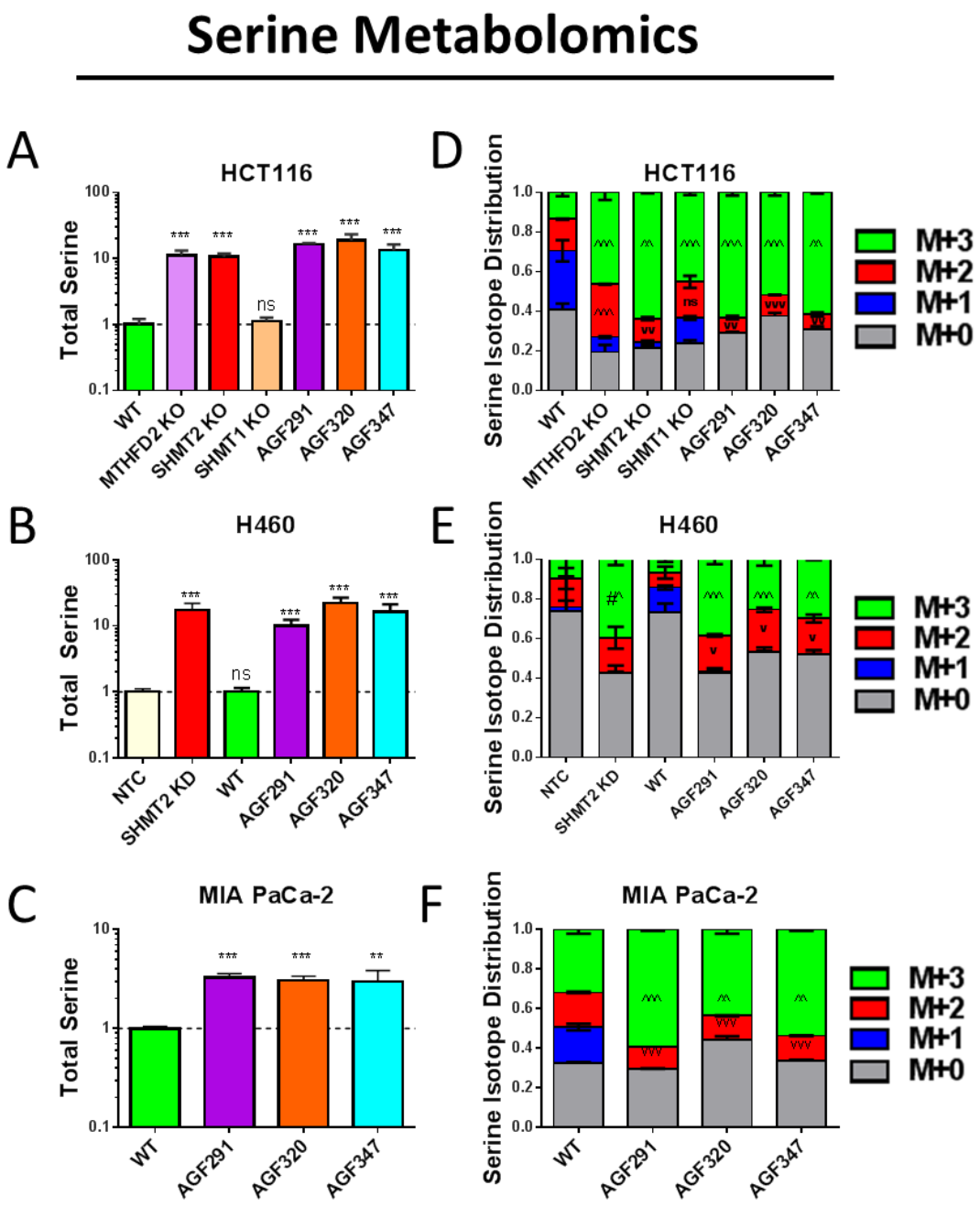

Figure 2.5 Serine Metabolomics Metabolomics analyses of total cellular serine (A-C) and serine isotope distribution (D-F) in HCT116, H460, and MIA PaCa-2 cell lines. Cells were treated with 10 µM drug or equivalent volume of DMSO for 48 hours and then processed for metabolomics analysis. The results are presented as mean values ± standard deviations for three technical replicates normalized to WT or NTC cells as appropriate (see section 2.2.6). Significant differences are denoted by # or * with ^ indicating a significant increase or ^{V} indicating a significant decrease and the number of symbols indicating the degree of significance (#^ or #^{V} denotes p <0.1, ^ or ^{V} denotes p<0.05, ^^ or ^{VV} denotes p<0.01, ^^^ or ^{VVV} denotes p<0.001).

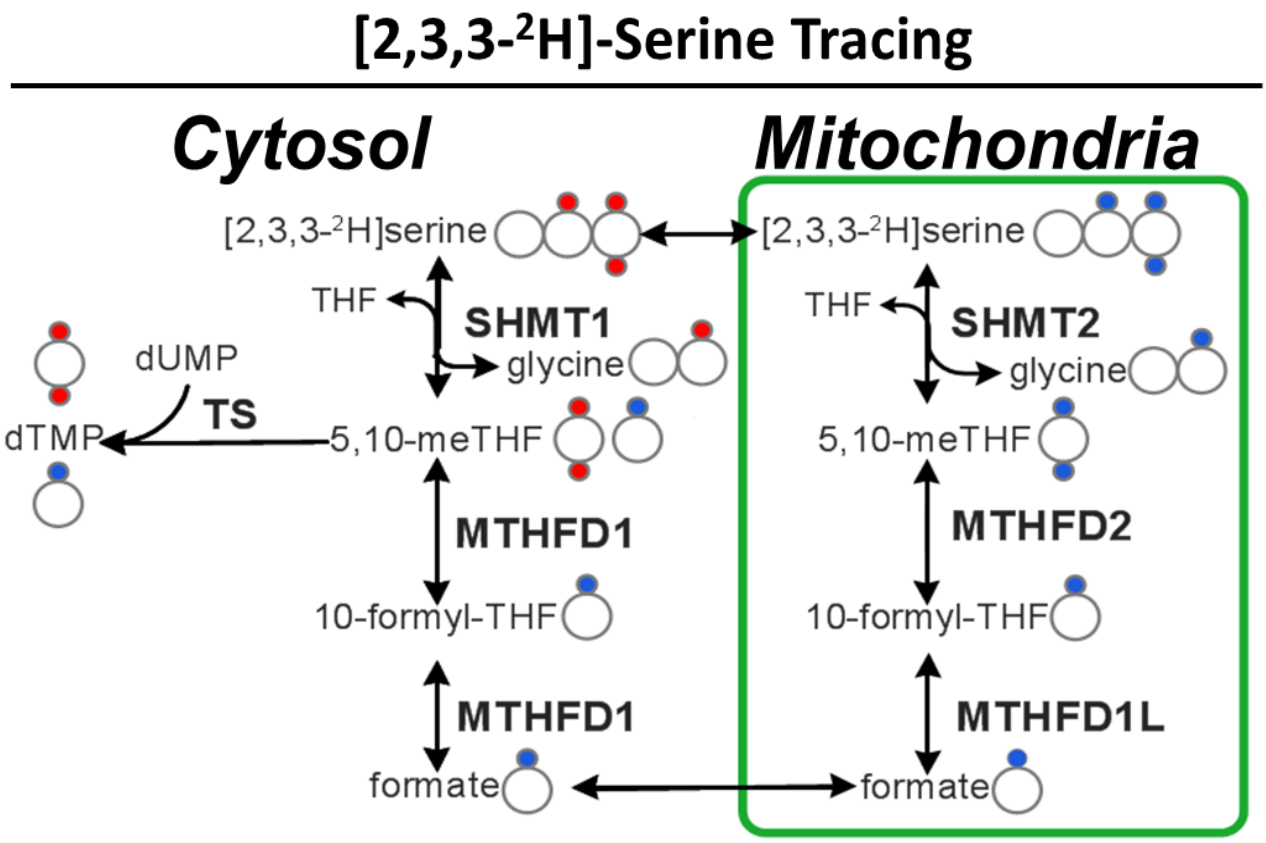

Figure 2.6 [2,3,3-^{2}H]-serine tracing [2,3,3-^{2}H]-serine (i.e. M+3 serine) is preferentially metabolized through the mitochondria by SHMT2 which generates M+2 5,10-meTHF. M+2 5,10-meTHF is metabolized to M+1 10-formylTHF by MTHFD2 and subsequently, to M+1 formate by MTHFD1L. M+1 formate is then exported to the cytosol and converted to M+1 5,10-meTHF by MTHFD1. Cytosolic M+1 5,10-meTHF is then incorporated into M+1 dTMP by TS. Alternatively, with KO of SHMT2 or MTHFD2, [2,3,3-^{2}H]-serine is catabolized in the cytosol by SHMT1, generating M+2 5,10-meTHF, which consequently forms M+2 dTMP. The deuterium flux through mitochondria (blue) or cytosol (red) is denoted by filled circles.

generates M+1 glycine (containing one deuteron) and M+2 5,10-meTHF (containing the remaining two deuterons). Catalysis of M+2 5,10-meTHF by MTHFD2 then generates M+110-formylTHF and the reversability of SHMT2 and MTHFD2 allows the levels of serine, 5,10-meTHF, and 10-formylTHF to equilibrate. Notably, reverse flux of M+2 5,10-meTHF through SHMT2 generates M+2 (rather than M+3) serine and the reverse flux of M+1 10-formylTHF through MTHFD2 and SHMT2 generates M+1 serine. Therefore, the isotope distribution of serine reflects the cellular levels of unmetabolized serine (M+3), 5,10-meTHF (M+2 serine), and 10-formylTHF (M+1 serine). Moreover, we expect inhibition of SHMT2 to induce an accumulation of unmetabolized (M+3) serine upstream and a depletion of 5,10-meTHF and 10-formylTHF (reflected in M+2 serine and M+1 serine, respectively) downstream. Conversely, inhibition of MTHFD2 will induce an accumulation of unmetabolized (M+3) serine AND 5,10-meTHF (reflected in M+2 serine) upstream, with depletion of 10-formylTHF (reflected in M+1 serine) downstream. Consequently, drug targeting of SHMT2 or MTHFD2 can be resolved by analysis of the M+2 serine fraction with a decrease indicating inhibition of the former and an increase indicating inhibition of the latter.

In the HCT116 cells (**Figure 2.5 – D**), KO of SHMT1, SHMT2, or MTHFD2 induced a significant increase in M+3 (unmetabolized) serine with a more profound accumulation (~7-fold) with SHMT2 KO than with either SHMT1 KO or MTHFD2 KO (~5-fold each). This confirms that SHMT2 is the primary serine catalysis enzyme in these cells. As expected, the M+2 serine fraction was increased with MTHFD2 KO (~2-fold), decreased with SHMT2 KO (~75% of WT), and was unchanged with SHMT1 KO. Notably, treatment with each of the drugs recapitulated the SHMT2 KO phenotype completely, significantly increasing the M+3 serine (5- to 7-fold) fraction and, most importantly, decreasing the M+2 serine fraction (~33% to 50% of WT).

Similar results were noted in the H460 cells (**Figure 2.5 – E**) where drug treatment (like SHMT2 KD) increased the M+3 serine fraction (~5-fold). However, the M+2 fraction in the drug treated samples was paradoxically increased (2- to 3-fold), perhaps because of the relatively smaller labeled serine pools (~25% of total serine) as compared to the HCT116 or MIA PaCa-2 cell lines. The M+2 serine fraction from the drug-treated H460 cells did, however, phenocopy the M+2 serine fraction from the SHMT2 KD H460 cells, suggesting SHMT2 was still the likely drug target. In the MIA PaCa-2 cells, as in the HCT116 cells, we noted a decreased M+2 serine fraction (~30% to 50% of WT) and increased M+3 serine fraction (1.5- to 2-fold) (**Figure 2.5 – F**). These results identified the mitochondrial enzyme target of **AGF291**, **AGF320**, and **AGF347** as SHMT2 (rather than MTHFD2).

2.3.4 Identification of the Cytosolic Enzyme Target(s) of AGF291, AGF320, and AGF347

Next, we sought to confirm the cytosolic targets of **AGF291**, **AGF320**, and **AGF347**, which the nucleoside/glycine protection studies (discussed in section 2.3.2) suggested were GARFTase and/or AICARFTase in *de novo* purine biosynthesis, as well as SHMT1. As inhibition of GARFTase and AICARFTase would result in accumulation of GAR and AICAR, respectively, we measured GAR and AICAR and found the drug treatments induced significant accumulations of both in all three human tumor cell lines (**Figure 2.7**). The magnitude of GAR accumulation (reflecting the potency of GARFTase inhibition) in all three cell lines was **AGF320** > **AGF347** > **AGF291**, suggesting **AGF320** was the most potent inhibitor of GARFTase (also reflected in partial protection by AICA + glycine treatment in section 2.3.2). Conversely, the magnitude of AICAR accumulation (reflecting the potency of AICARFTase inhibition) in all three cell lines was **AGF291** > **AGF347** > **AGF320** (the opposite order of GAR accumulation), suggesting **AGF291** was the most potent inhibitor of AICARFTase. However, as

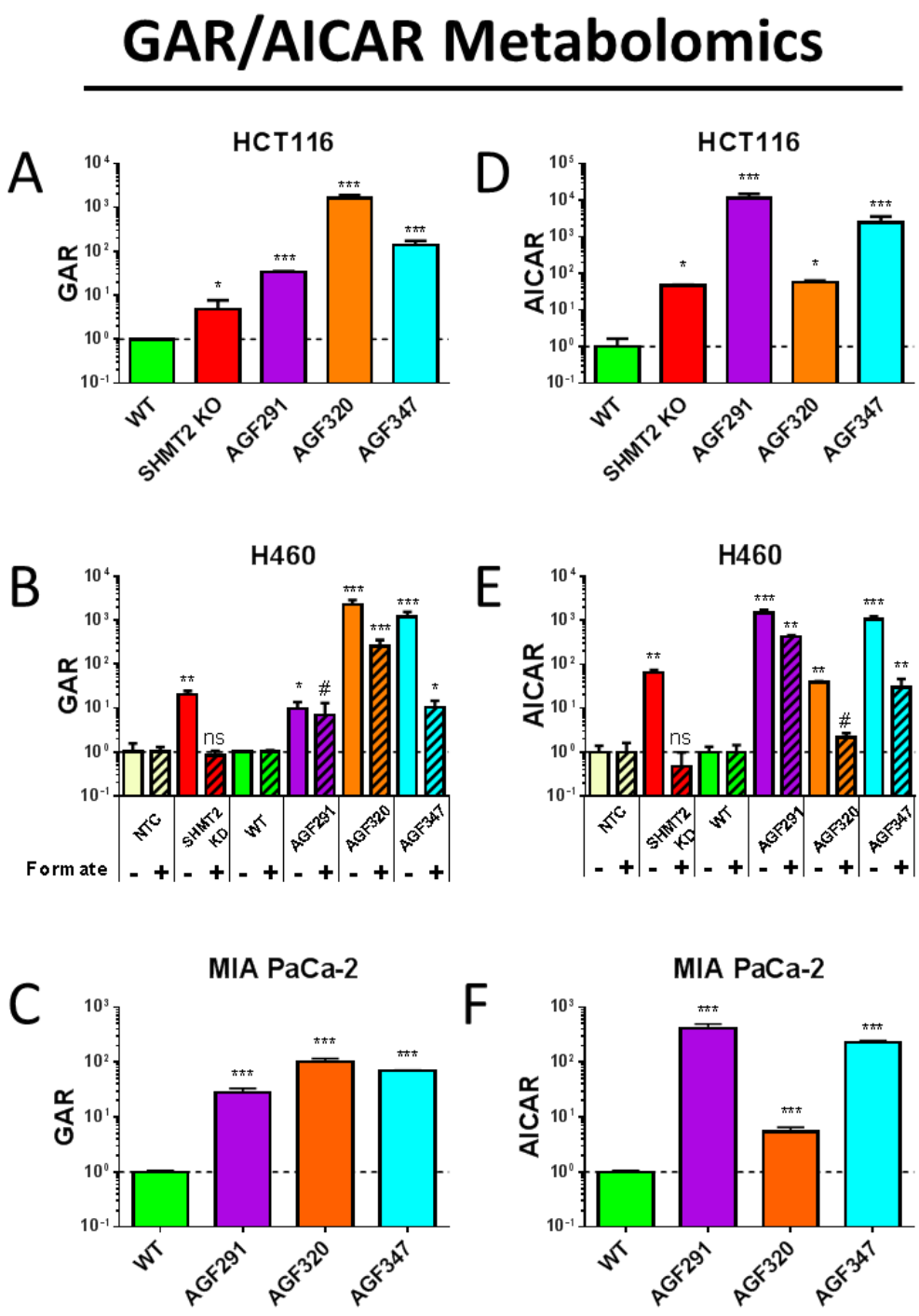

Figure 2.7 GAR/AICAR Metabolomics Metabolomics analyses of total cellular GAR (A-C) and AICAR (D-F) in HCT116, H460, and MIA PaCa-2 cell lines. Cells were treated with 10 µM drug or equivalent volume of DMSO for 48 hours and then processed for metabolomics analysis. The results are presented as mean values ± standard deviations for three technical replicates normalized to WT or NTC cells as appropriate (see section 2.2.6). Significant differences are denoted by # or * the number of symbols indicating the degree of significance (# denotes p <0.1, * denotes p<0.05, ** denotes p<0.01, *** denotes p<0.001).

all three compounds were confirmed inhibitors of SHMT2, they would all deplete cytosolic 10-formylTHF and consequently, *indirectly* inhibit GARFTase and AICARFTase which use 10-formylTHF as a cofactor (**Figure 1.2**). Indeed, this phenotype was noted with the SHMT2 KO HCT116 cells which induced a ~5-fold and ~40-fold increase in GAR (**Figure 2.7 – A**) and AICAR (**Figure 2.7 – E**) respectively. To determine if the accumulation of GAR/AICAR was primary (due to direct inhibition of GARFTase/AICARFTase) or secondary (due to depletion of cytosolic 10-formylTHF by inhibition of SHMT2), we performed the experiments in the H460 cells (**Figure 2.7 – B and E**) with and without 1 mM added formate, which had been shown to replenish cytosolic 10-formylTHF and rescue accumulation of GAR/AICAR due to SHMT2 inhibition (Ducker et al., 2016). As expected, in the SHMT2 KD H460 cells, we noted a ~20-fold and ~70-fold increase in GAR (**Figure 2.7 – B**) and AICAR (**Figure 2.7 – E**) respectively, both of which were fully reversed by addition of exogenous formate. However, the accumulations of GAR and AICAR with drug treatment in H460 cells were only partially reversed with formate supplementation, suggesting these drugs featured direct inhibition of either GARFTase (**AGF320 > AGF347** > **AGF291**) or AICARFTase (**AGF291** > **AGF347** > **AGF320**).

To assess possible SHMT1 inhibition, we traced [2,3,3-^{2}H]-serine incorporation into dTTP as the flux of deuterated serine through SHMT2 in the mitochondria forms M+1 dTTP, whereas flux of serine through SHMT1 in the cytosol forms M+2 dTTP (**Figure 2.6**). As we had established these cells preferentially catabolized serine through the mitochondria, it was unsurprising that untreated cells of each cell line generated predominantly M+1 dTTP (**Figure 2.8**). As expected, the SHMT2 KO HCT116 cells (**Figure 2.8 – A**) and the SHMT2 KD H460 cells (**Figure 2.8 – B**) generated a significant portion of M+2 dTTP, indicating compensatory reverse flux of serine through SHMT1. However, treatment with the SHMT2-inhibiting drugs

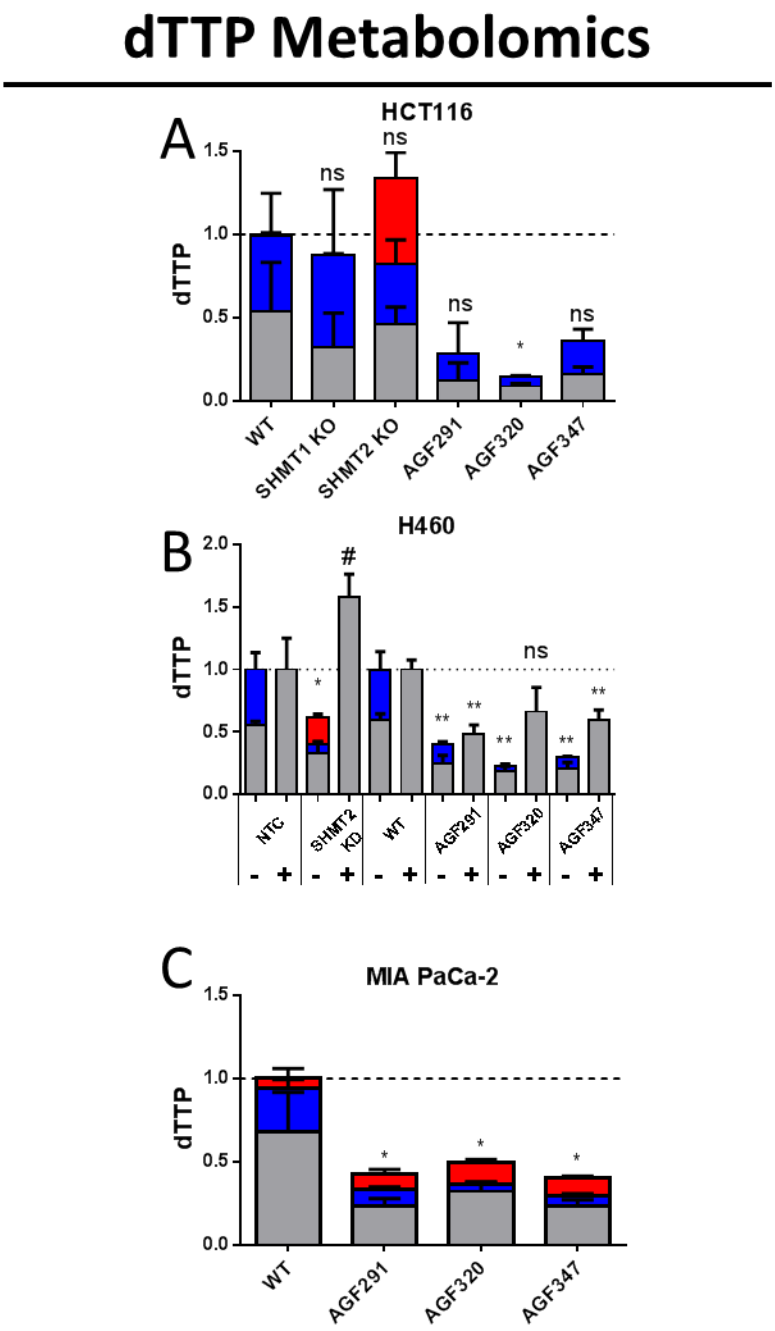

Figure 2.8 dTTP Metabolomics Metabolomics analyses of total cellular dTTP pools with isotope distributions in HCT116 (A), H460 (B), and MIA PaCa-2 (C) cell lines. Cells were treated with 10 µM drug or equivalent volume of DMSO for 48 hours and then processed for metabolomics analysis. The results are presented as mean values ± standard deviations for three technical replicates normalized to WT or NTC cells as appropriate (see section 2.2.6). Significant differences are denoted by # or * with the number of symbols indicating the degree of significance (# denotes $p < 0.1$, * denotes $p < 0.05$, ** denotes $p < 0.01$, *** denotes $p < 0.001$).

did not induce accumulation of M+2 dTTP in HCT116 or H460 cells. Only the MIA PaCa-2 cells demonstrated increased M+2 dTTP, albeit with suppressed overall dTTP pools. Taken together, these results suggested either sufficient residual flux through SHMT2 to maintain the M+1 labeling or inhibition of the compensatory pathway through SHMT1 (as reflected in decreased overall dTTP pools). As thymidine was not shown to be a protective metabolite in section 2.3.2 (in contrast with results seen with primary TS inhibitors such as PMX (Chattopadhyay et al., 2007)), these results were most consistent with direct inhibition of SHMT1 rather than inhibition of TS.

2.3.5 *In Vitro* Confirmation of Enzyme Targets

Taken together, our metabolomics results indicated that **AGF291**, **AGF320**, and **AGF347** targeted SHMT2 (and not MTHFD2) in the mitochondria and GARFTase and/or AICARFTase, as well as SHMT1, in the cytosol. To confirm these results, we directly assayed each of these enzymes (as described in section 2.2.8) with *in vitro* cell-free assays (**Table 2.2**). The values in **Table 2.2** reflect inhibition potencies of the monoglutamyl (i.e., non-polyglutamyl) form of the drug, which are usually far less potent than those of the polyglutamyl forms of antifolate compounds (as discussed in section 1.3). Consequently, the enzyme inhibition potencies are imperfect measures of actual enzyme inhibition (as the distribution of polyglutamyl forms in the cell may differ between drugs). For **AGF94**, an established inhibitor of GARFTase alone, we note 100-fold (K_i 0.88 µM versus K_i >100 µM) increased potency for GARFTase relative to SHMT1 or SHMT2, suggesting the inhibition at SHMT1/2 does not play any significant role in drug activity. . Conversely, **AGF291**, **AGF320**, and **AGF347** all potently inhibited both SHMT1 (K_is ~0.1 to 2.9 µM) and SHMT2 (K_is ~0.5 to 2.2 µM). Importantly, none

Table 2.2 *In vitro* cell-free enzyme assays [K_i (μM)]

Compound	GARFTase	AICARFTase	SHMT2	MTHFD2	SHMT1
AGF94	0.88 (0.71)	NI	188.0 (91.8)	NI	112 (57)
PMX	5.19 (1.63)	281(23)	NI	NI	NI
AGF291	ND	13.67 (3.16)	0.63 (0.29)	NI	0.090 (0.56)
AGF347	3.13 (0.66)	3.72 (1.61)	2.19 (0.23)	NI	2.91 (0.59)
AGF331	ND	ND	ND	ND	ND
AGF320	0.33 (0.22)	2.36 (1.99)	0.56 (0.20)	NI	0.126 (0.030)

In vitro cell free enzyme assays are described in the section 2.2.8. NI denotes "no inhibition" was observed up to 200 μM inhibitor and ND denotes "not determined". Results reflect mean ± standard deviation of at least three experimental replicates.

of the compounds inhibited MTHFD2 up to 200 μM. For the *de novo* purine biosynthesis enzymes, **AGF291** inhibited AICARFTase (K_i = 13.67 μM), but not GARFTase, **AGF320** inhibited GARFTase (K_i = 0.33 μM) ~7-fold more potently than AICARFTase (K_i = 2.36 μM), and **AGF347** inhibited GARFTase (K_i = 3.13 μM) and AICARFTase (K_i = 3.72 μM) roughly equally. Pleasingly, these results perfectly matched the metabolomics results discussed in section 2.3.4 which indicated that **AGF291** was likely primarily an AICARFTase-targeting drug, **AGF320** was likely primarily a GARFTase-targeting drug, and **AGF347** likely targeted both enzymes equally.

2.3.6 *In vivo* Antitumor Efficacy of AGF291 and AGF347 against MIA PaCa-2 Tumor Xenografts: Early Stage Disease

Having established that **AGF291**, **AGF320**, and **AGF347** were inhibitors of SHMT1 and SHMT2 as well as of GARFTase and/or AICARFTase, we then sought to demonstrate *in vivo* antitumor efficacy for this series which, notably, was not noted in the earlier-generation pyrazolopyran compounds due to their microsomal degradation (Ducker et al., 2017). We carried out toxicity trials to determine maximum tolerated dose (MTD) of each of the drugs in mice bearing tumor xenografts of H460, HCT116, and MIA PaCa-2 cells. Through these trials, we determined the MIA PaCa-2 tumor xenografts were most sensitive *in vivo* to the effects of the drugs, and that **AGF291** and **AGF347** appeared more potent in these small (n = 2) preliminary trials than **AGF320**. Therefore, these two drugs were advanced into full early-stage trials against MIA PaCa-2 tumor xenografts in SCID mice. As a control, we compared **AGF291-** and **AGF347-**treated mice to mice treated with gemcitabine, the longstanding standard-of-care for pancreatic cancer (Rossi et al., 2014). In both trials, NCR SCID mice were fed a folate-deficient diet *ad libitum* for 14 days to deplete serum folate to levels comparable to those found in humans

(Alati et al., 1996; Golani et al., 2016; Wang et al., 2010; Wang et al., 2011), then subcutaneously and bilaterally implanted with MIA PaCa-2 pancreatic adenocarcinoma xenografts, and non-selectively randomized into control and treatment groups (5 mice/group).

AGF291 and gemcitabine were administered IV beginning on day 3 following engraftment at doses slightly less than their respective MTDs (see section 2.2.9) Both **AGF291** and gemcitabine were efficacious (**Figure 2.9 - A**), with median tumor burdens on day 14 of 256 mg (range 75-851 mg) and 255 mg (range 63-322 mg), respectively, compared to 1321 mg (range 685-1465 mg) for the control cohort. Median T/C values were 19% for both compounds. Tumor growth delays (median T-C to reach 1000 mg) of 10 days for **AGF291** and 7 days for gemcitabine were recorded. **AGF291** and gemcitabine were well tolerated with modest weight losses (9% median nadir on day 17 and 12% median nadir on day 6, respectively) that were completely reversible after cessation of therapy. Thus, at equitoxic dose levels, **AGF291** showed comparable anti-tumor efficacy to gemcitabine, with a 20-fold decreased dose requirement and no acute or long-term toxicities other than reversible weight loss.

However, the results with **AGF347** were far more remarkable. The median tumor burden on day 16 was 420 mg (range 284-552 mg) compared to 1189 mg (range 601-1711 mg) for the control cohort (T/C=35%). **AGF347** was far more efficacious than gemcitabine, with a median tumor burden on day 16 of 0 mg (range 0-276 mg) (T/C=0%). Gemcitabine showed a slight growth delay (19-24 days to reach 1000 mg) compared to the untreated controls (12.5-20 days). For **AGF347** arm, 5 of 5 mice showed significant growth delay with 4 mice ranging from 21 to 77 days and one mouse showing undetectable tumor up to 136 days (**Figure 2.9 - B**). When this mouse was rechallenged with tumor, the tumor readily engrafted, establishing this as a “cure”. Thus, at equitoxic doses, **AGF347** showed exceptionally more potent antitumor efficacy than

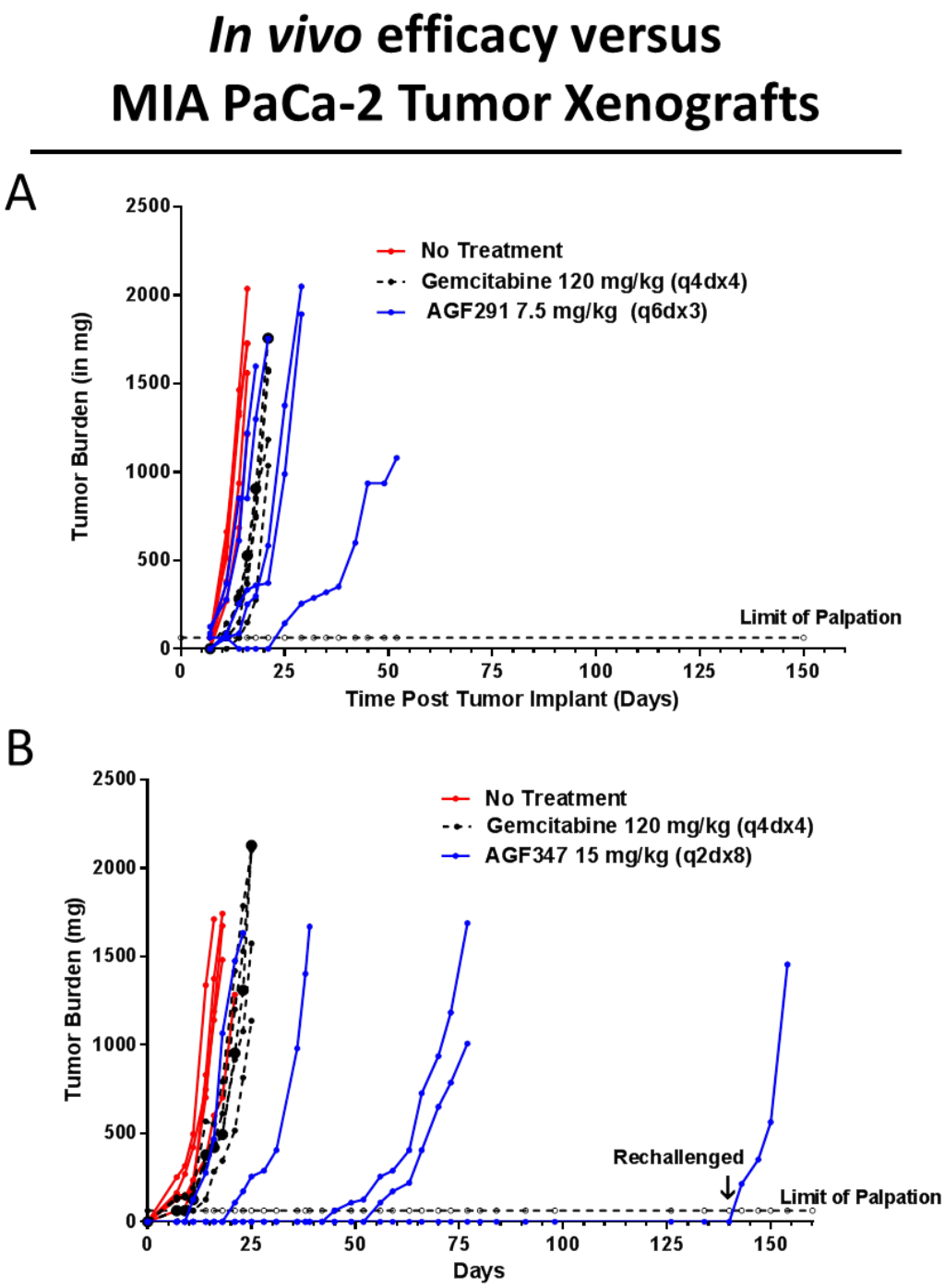

Figure 2.9 *In vivo* efficacy of AGF291 and AGF347 against MIA PaCa-2 tumor xenograft models in SCID mice. (A) **AGF291** (7.5 mg/kg q6dx3) vs gemcitabine (120 mg/kg q4dx4). Plot reflects individual tumor burdens for each mouse. (B) **AGF347** (15 mg/kg q2dx8) vs gemcitabine (120 mg/kg q4dx4). Plot reflects individual tumor burdens for each mouse. One mouse in the **AGF347**-treated group was tumor-free after 136 days and was rechallenged with tumor. The tumor readily engrafted, establishing this mouse as a "cure".

gemcitabine, with a 4-fold decreased dose requirement, no acute or long-term toxicities otherthan reversible weight loss, and 1 of 5 mice cured.

2.4 Discussion

In this chapter, we designed, synthesized, and characterized enzyme targets of novel inhibitors of C1 metabolism in mitochondria, the primary catabolic pathway for serine and for synthesis of glycine (Ducker and Rabinowitz, 2017; Newman and Maddocks, 2017; Tibbetts and Appling, 2010; Yang and Vousden, 2016). Serine catabolism in mitochondria by SHMT2, the first enzyme in the mitochondrial C1 pathway, is the principal source of C1 units for cytosolic *de novo* purine and thymidylate biosynthesis, and of reducing equivalents and ATP (Ducker and Rabinowitz, 2017; Morscher et al., 2018; Newman and Maddocks, 2017; Tibbetts and Appling, 2010; Yang and Vousden, 2016). We targeted SHMT2 with novel 5-substituted pyrrolo[3,2-*d*]pyrimidine analogs, rationally designed based on structural similarities to previously reported 5-subsituted pyrrolo[2,3-*d*]pyrimidine compounds (Mitchell-Ryan et al., 2013; Wang et al., 2015) and N-substituted THF metabolites, including 5,10-meTHF and 5-formylTHF (leucovorin). We identified lead compounds **AGF291**, **AGF320** and **AGF347** that inhibited proliferation of a broad spectrum of tumor subtypes including lung (H460), colon (HCT116), and pancreas (MIA PaCa-2).

We identified critical enzyme targets for our compounds through glycine/nucleoside protection experiments and targeted metabolomics with a [2,3,3-^{2}H]-serine tracer, and identified SHMT2 in mitochondria as the principal intracellular target, along with SHMT1, GARFTase and/or AICARFTase in the cytosol. Inhibition of all these intracellular targets was confirmed by *in vitro* assays with purified recombinant enzymes using the monoglutamyl inhibitors. Our finding that SHMT1 was a direct target of our inhibitors resembles results for a dual-

SHMT1/SHMT2 pyrazolopyran inhibitor SHIN1 (Ducker et al., 2017) and is of particular interest as this prevents metabolic "compensation" by reversal of SHMT1 catalysis in response to loss of SHMT2 activity (Ducker et al., 2016; Ducker et al., 2017). As **AGF291** and **AGF347** showed the most potent *in vivo* activity in preliminary toxicity trials, these compounds were tested *in vivo* with a MIA PaCa-2 xenograft model in SCID mice. While **AGF291** was efficacious, **AGF347** exhibited extraordinarily potent *in vivo* efficacy, far exceeding that of gemcitabine (standard-of-care) even at a 20-fold lower dose, resulting in sustained tumor growth delay and a cure in one mouse.

The active 5-substituted pyrrolo[3,2-*d*]pyrimidine compounds described in this chapter expanded upon earlier results with non-folate pyrazolopyran inhibitors of human SHMT2 (Ducker et al., 2017) and, to our knowledge, represented the first *bona fide* inhibitors of this intracellular target with demonstrated *in vivo* antitumor efficacy. However, a number of pharmacodynamic factors may have contributed to the *in vitro* antitumor effects of the novel analogs described in this chapter and these warranted further study. These pharmacodynamic characteristics include transport across the plasma membrane by PCFT and/or RFC and into mitochondria (potentially by MFT) (Lawrence et al., 2011; McCarthy et al., 2004)), as well as metabolism to drug polyglutamates (analogous to PMX and other classic antifolates – see section 1.3 (Chattopadhyay et al., 2007; Visentin et al., 2012)), which would impact binding to intracellular targets in both the mitochondria and the cytosol. Moreover, glycine and 5,10-meTHF derived from SHMT2 play a critical role in glutathione biosynthesis/reactive oxygen species (ROS)-scavenging and mitochondrial protein translation, respectively (as discussed in section 1.1.3), so these drugs may have impacted these cellular functions as well. Variations in these parameters likely account for differences in relative antiproliferative activities of these

analogs toward the assorted tumor models in this report, and are the focus of the experiments conducted in section 3.

CHAPTER 3- CELLULAR PHARMACODYNAMICS OF LEAD NOVEL 5-SUBSTITUTED PYRROLO[3,2-*d*]PYRIMIDINE COMPOUNDS AGF291, AGF320, AND AGF347

3.1 Introduction

The work in chapter 2 established the 5-substituted pyrrolo[3,2-*d*]pyrimidine compounds **AGF291**, **AGF320**, and **AGF347** as potent inhibitors of SHMT1 and SHMT2, as well as GARFTase and/or AICARFTase. However, the transport kinetics of these compounds as well as the downstream cellular effects stemming from inhibition of these enzymes were not assessed. In this chapter, we sought to elucidate the cellular pharmacodynamics of **AGF291**, **AGF320**, and **AGF347.**

First, we sought to characterize PCFT- and RFC-mediated transport of these compounds. Enzyme kinetics were studied in the isogenic CHO cell lines R2/PCFT4 and PC43-10 expressing PCFT and RFC individually (Deng et al., 2008; Deng et al., 2009), as well as in the RFC-expressing HeLa subline R1-11 RFC2 (Wang et al., 2015). Uptake into HCT116, MIA PaCa-2, and H460 cells was characterized via competitive inhibition of [^{3}H]-**MTX** and [^{3}H]-**AGF347** uptake with **AGF94** (a PCFT-selective substrate) and **PT523** (an RFC-selective substrate) (as discussed previously in sections 1.3.1 and 1.3.2). To assess mitochondrial uptake and the potential role of MFT (section 1.3.4) in drug transport, we transfected human MFT into GlyB CHO cells, which restored the MFT function of these MFT-null cells (McCarthy et al., 2004; Titus and Moran, 2000), creating the GlyBTII model. As a human tumor cell line model, we generated MFT KD and NTC MIA PaCa-2 cell lines with lentiviral shRNA. We incubated both CHO and human tumor models with [^{3}H]-**folic acid**, [^{3}H]-**MTX**, and [^{3}H]-**AGF347** and isolated mitochondrial and cytosolic fractions through differential centrifugation to determine subcellular drug compartmentation and the impact of MFT KD or KO. Using the MIA PaCa-2 NTC cells,

we assessed formation of polyglutamyl forms of [^{3}H]-**AGF347** by high performance liquid chromatography (HPLC).

Next, we sought to assess downstream effects on cellular function resulting from inhibition of cytosolic and mitochondrial C1 metabolism, respectively. As all drugs targeted *de novo* purine biosynthesis at either GARFTase and/or AICARFTase, we sought to quantify their effects on adenine nucleotide pools. Moreover, as all drugs featured either primary or secondary inhibition of AICARFTase (as discussed in section 2.3.4), they also induced accumulation of AICAR (**Figure 2.6**) in all cell lines. Accumulation of AICAR (an AMP-mimetic) induced by PMX had previously been shown (Racanelli et al., 2009; Rothbart et al., 2010) to activate AMPK, consequently downregulating the pro-survival mTOR pathway, so we sought to assess the activation of AMPK and inhibition of mTOR with these compounds.

For cellular effects resulting from inhibition of mitochondrial C1 metabolism at SHMT2, we primarily focused on mitochondrial respiration (as SHMT2 had been proven critical to correct translation of mitochondrial electron transport chain proteins – see section 1.1.3) and ROS scavenging (as glycine and NAD(P)H produced from mitochondrial C1 metabolism had been shown to be critical for glutathione biosynthesis and regeneration (Fan et al., 2014; Ye et al., 2014).

Finally, given the unprecedented antitumor efficacy of **AGF347** against MIA PaCa-2 tumor xenografts in an early-stage tumor model (as discussed in section 2.3.6), we sought to assess the efficacy of **AGF347** in late-stage disease by allowing the MIA PaCa-2 tumor xenografts to grow to 100-150 mg before treatment (see section 3.2.10). In addition, we performed metabolomics analyses on several tumors harvested from both **AGF347**-treated and

control mice to confirm *in vivo* enzyme targets. The work discussed in this chapter was partially published and is included in a manuscript under preparation.

3.2 Materials and Methods

3.2.1 Chemicals

[^{3}H]-**AGF347** (9 Ci/mmol) and [^{3}H]-**MTX** (10-30 Ci/mmol) were purchased from Moravek Biochemicals (Brea, CA). Leucovorin [(6R,S) 5-formyl THF] and **MTX** were provided by the Drug Development Branch, National Cancer Institute (Bethesda, MD). **PMX** was purchased from LC Laboratories (Woburn, MA). Gemcitabine (Gemzar) was purchased from Pfizer (New York City, NY). **PT523** (N^{α}-(4-amino-4-deoxypteroyl)-N^{δ}-hemiphthaloyl-l-ornithine) was a gift of Dr. Andre Rosowsky (Dana-Farber cancer Institute, Boston, MA). **AGF291**, **AGF320**, and **AGF347** were synthesized by Dr. Gangjee and his graduate students.

3.2.2 Cell Culture

The HCT116 cell lines including the SHMT1, SHMT2, and MTHFD2 KO cells (Ducker et al., 2016; Ducker et al., 2017) were generously provided by Drs. Gregory Ducker (University of Utah) and Joshua Rabinowitz (Princeton University). The MIA PaCa-2 cells were provided by Dr. Yubin Ge (Karmanos Cancer Institute); both were verified by short tandem repeat analysis by Genetica DNA Laboratories (Burlington, NC). The R1–11 RFC- and PCFT-null HeLa subline was a gift from Dr. I. David Goldman (Albert Einstein School of Medicine, Bronx, NY) (Zhao, 2009). The R1–11-RFC2 cell line was developed in our laboratory by transfection of R1–11 cells with the pZeoSV2-RFC vector and clonal selection, as previously described (Wang et al., 2015). For non-transport experiments, all the above cell lines were all maintained in folate-free RPMI supplemented with 10% dialyzed fetal bovine serum (Sigma-Aldrich), 1% penicillin/streptomycin solution, 2 mM L-glutamine, and 25 nM leucovorin. For transport

experiments (see section 3.2.6), these cells were maintained in RPMI supplemented with 10% fetal bovine serum, 1% penicillin/streptomycin solution, and 2 mM glutamine instead. R1-11 cells were kept under continuous selection with 500 nM **MTX** and 1 mg/ml G418. R1-11 RFC2 cells were kept under continuous selection with 100 µg/mL Zeocin. MTXRIIOua^{R}2-4 (i.e. R2) CHO cells were generously provided by Dr. Wayne Flintoff (University of Western Ontario) (Flintoff et al., 1976). From this parental R2 cell line, human RFC and PCFT were individually transfected to generate the isogenic CHO cell lines designated PC43-10 (RFC) and R2/PCFT4 (PCFT) (Deng et al., 2008; Deng et al., 2009; Wong et al., 1995). GlyB cells were a generous gift of Dr. Larry Chasin (Columbia University). GlyBTII cells were derived from GlyB cells by Yijun Deng, a former graduate student in the lab. Briefly, GlyB cells underwent electroporation with human MFT cDNAs in a pcDNA3.1 (-)/myc-His A-tagged vector and monoclonal cultures were then isolated and expanded for screening. The monoclonal culture with the highest MFT-expression by RT-PCR was denoted GlyBTII. Successful transfection of the GlyB cells to generate GlyBTII was subsequently confirmed by Western Blot in this section (**Figure 3.1 – A**). CHO cell lines were maintained in αMEM supplemented with 10% bovine calf serum, 1% penicillin/streptomycin solution, and 2 mM L-glutamine (and 1 mg/ml G418 for the GlyBTII cells) in a humidified atmosphere at 37 °C in the presence of 5% CO_2 and 95% air. Additionally, the transfected CHO cell lines (i.e. R2/PCFT4, PC43-10, and GlyBTII) were maintained under continuous selection with 1 mg/ml of G418.

3.2.3 Generation of MIA PaCa-2 MFT Knockdown (MIA PaCa-2 MFT KD) Cell Line

MIA PaCa-2 cells were seeded (2 x 10^5 cells/well) in 24 well plates containing 1 ml of routine culture media (i.e. folate-free RPMI 1640 supplemented with 10% dialyzed fetal bovine serum, 1% penicillin/streptomycin, 2 mM L-glutamine, and 25 nM leucovorin). Cells were

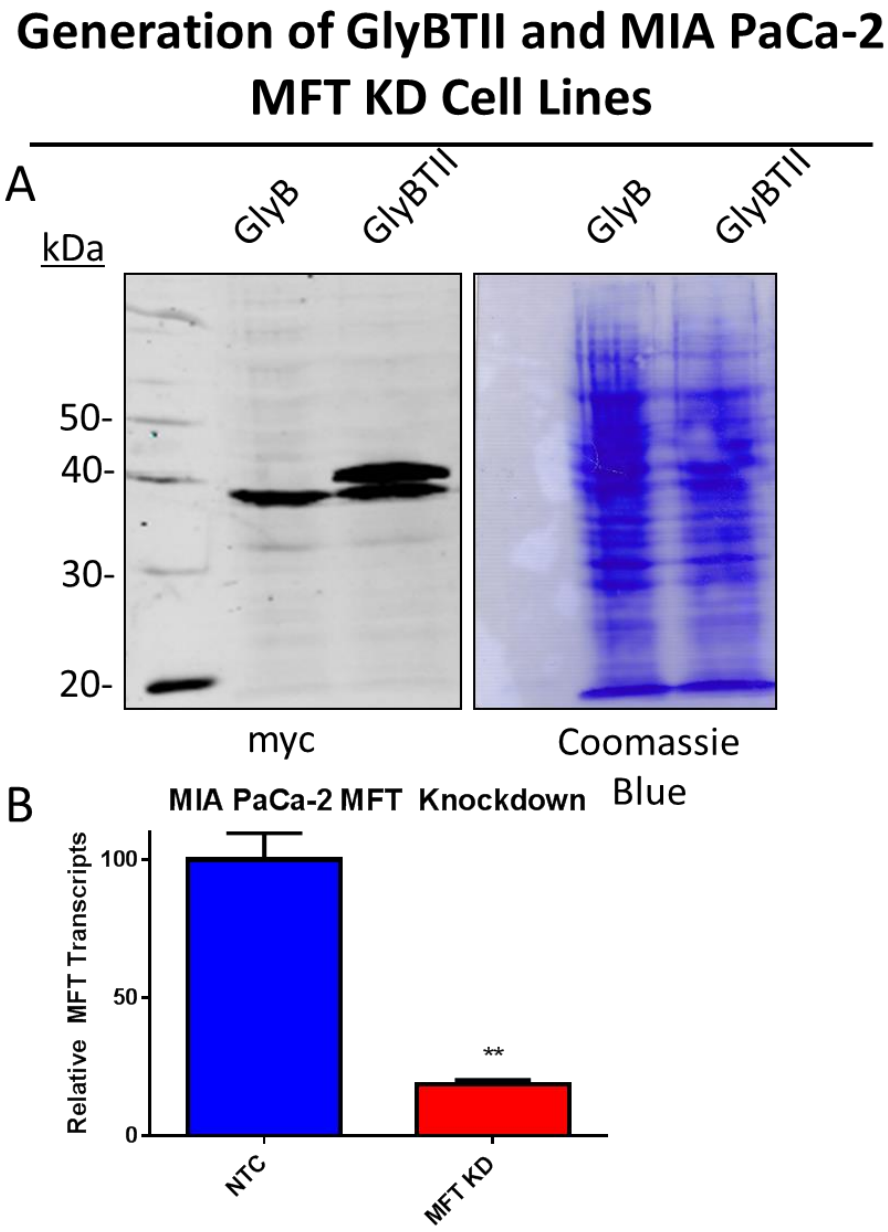

Figure 3.1 Confirmation of GlyBTII and MIA PaCa-2 MFT KD cell lines. GlyBTII cells were derived from GlyB cells by electroporation with human MFT cDNAs in a pcDNA3.1 (-)/myc-His A-tagged vector. Human MFT expression was confirmed by Western blot (A) for myc with Coomassie Blue staining used as a loading control (see section 3.2.4). MFT knockdown in MIA PaCa-2 MFT-shRNA transduced cells was confirmed by RT-PCR (see section 3.2.5) on a monoclonal culture. (B) Significant differences are denoted by # or * with the number of symbols indicating the degree of significance (# denotes $p < 0.1$, * denotes $p < 0.05$, ** denotes $p < 0.01$, *** denotes $p < 0.001$).

treated with 4 μg/ml polybrene and 10^5 transducing units of MISSION Lentiviral particles (Sigma-Aldrich) containing shRNA targeting MFT (TRCN0000043091). An additional well contained MIA PaCa-2 cells without shRNA particles. After 24 hours, the media was replaced with fresh routine culture media including 2 μg/ml puromycin as a selection marker. Once cells were confluent (and non-transduced cells had died), cells were harvested, passaged 3-4 times, then assayed by RT-PCR for MFT KD relative to NTC MIA PaCa-2 cells (Wilson et al., 2016). To isolate single clones, these cells were then plated in 100 mm dishes (200 cells/dish) in the presence of 2 μg/ml puromycin. Colonies were isolated, expanded (in RPMI 1640 supplemented with 10% fetal bovine serum, 1% penicillin/streptomycin, and 2 mM L-glutamine) and clonal cultures were assayed for MFT KD via RT-PCR (**Figure 3.1 - B**). KD was further confirmed via a [^{3}H]-**folic acid** uptake experiment. A clonal MIA PaCa-2 MFT KD culture was used as a control for the metabolism experiments.

3.2.4 Gel Electrophoresis and Western Blots

GlyB and GlyBTII cells were cultured as described in section 3.2.2. Cells were plated in 2 T150 flasks each and harvested when cells were ~90% confluent. Mitochondrial fractions were isolated as described in section 3.2.7 and assayed for protein concentrations (Lowry et al., 1951). Equal amounts of protein (36 μg) from each sample were electrophoresed on 10% polyacrylamide gels with SDS (Laemmli, 1970) and transferred to polyvinylidene difluoride membranes (ThermoFisher) (Matsudaira, 1987). To detect MFT expression, membranes were incubated for 24 hours with rabbit anti-myc primary antibody (Covance Inc., Princeton, NJ - MMS-150P). Subsequently, membranes were incubated in IRDye800CW-conjugated goat anti-rabbit IgG secondary antibody (LICOR Biosciences, Omaha, NE) for 90 min and scanned with

an Odyssey infrared imaging system (LICOR Biosciences). A Coomassie Blue stain of the blot was used as a loading control (**Figure 3.1 - B**).

For AMPK activation, total and phospho-AMPK, regulatory associated protein of mTOR (Raptor), and S6K1 were probed by Western Blot (Mitchell-Ryan et al., 2013). Briefly, HCT116 WT and SHMT2 KO cells (1 million cells/dish for vehicle-treated samples, 1.5 million cells/dish for drug-treated samples) were seeded in 60 mm dishes in 5 ml of folate-free RPMI supplemented with 10% dialyzed fetal bovine serum, 1% penicillin/streptomycin, 2 mM L-glutamine, and 25 nM leucovorin. Cells were allowed to adhere for 24 hours after which 10 µM **AGF291**, 10 µM **AGF320,** 10 µM **AGF347**, or 1 mM AICAR, or a comparable volume of vehicle (DMSO) was added. Incubations were performed at 37^{o}C with 5% CO_2. After 48 hours, cells were harvested and disrupted by sonication, with cell debris removed by centrifugation. The soluble cell fractions were assayed for protein concentrations (Lowry et al., 1951) and equal amounts of protein (50 µg for AMPK/S6K1 in both cell lines, 50 µg for Raptor in MIA PaCa-2 cells, 100 µg for Raptor in HCT116 cells) from each sample were electrophoresed on 10% polyacrylamide gels with SDS (Laemmli, 1970) and transferred to polyvinylidene difluoride membranes (ThermoFisher) (Matsudaira, 1987). To detect phospho- or total AMPK, Raptor, or p70-/p85-S6K1, membranes were incubated for 72 hours with rabbit primary antibody (Cell Signaling Technology, Danvers, MA [Catalog Number] – total AMPK [5831S], P-AMPK (T172) [2535S], Total Raptor [2280S], P-Raptor (S792) [2083S], Total p70-/p85-S6K1 [2708S], P-p70/P-p80-S6K1 (T389/T412) [9234S]). The blots were developed by incubating in IRDye800CW-conjugated goat anti-rabbit IgG secondary antibody (LICOR Biosciences, Omaha, NE) for 90 min and scanning with an Odyssey infrared imaging system (LICOR Biosciences).

Protein loading was normalized to β-actin using anti-β-actin mouse antibody (Sigma-Aldrich [A2228]). Densitometry was conducted in Image Studio Software (LICOR Biosciences).

3.2.5 RT-PCR

Cells were harvested from either 60 mm dishes or T25 flasks at ~80% confluence and RNAs extracted using TRIzol reagent (Invitrogen, Carlsbad, CA). cDNAs were synthesized with random hexamers, MuLV reverse transcriptase, and RNase inhibitor (Applied Biosystems, Waltham, MA) and purified with a QIAquick PCR Purification Kit (QIAGEN, Valencia, CA). Quantitative RT-PCR was performed using a Roche LightCycler 480 (Roche Diagnostics, Indianapolis, IN) with gene-specific primers and SYBR Green I dye) and transcript levels were normalized to transcript levels of β-actin and GAPDH.

3.2.6 Plasma Membrane Transport

General inhibition studies with R2, R2/PCFT4, and PC43-10 cells were performed as previously described (Ravindra et al., 2018). Buffers used include MES (2-(N-morpholino)ethanesulfonic acid)-buffered saline at pH 5.5 (20 mM MES, 140 mM NaCl, 5 mM KCl, 2 mM $MgCl_2$, and 5 mM glucose), HEPES at pH 6.8 (20 mM HEPES, 140 mM NaCl, 5 mM KCl, 2 mM $MgCl_2$, and 5 mM glucose), and anion-free buffer at pH 7.2 (20 mM HEPES and 235 mM sucrose). Calculations of K_m and V_{max} were performed with concentrations of [^{3}H]-**AGF347** or [^{3}H]-**MTX** from 20 nM to 500 nM (R2/PCFT4 at pH 5.5) or 250 nM to 5 μM (R1-11 RFC2 at pH 7.2). Analysis of the data used Lineweaver-Burk plots. Using the average K_m and V_{max} values from these experiments, K_i values for each of the drugs relative to 0.5 μM [^{3}H]-**MTX** were calculated by Dixon plots using concentrations of cold competitor (i.e. drug) from 0 to 500 nM (R2/PCFT4 at pH 5.5) or 0 to 1 μM (R1-11 RFC2 at pH 7.2). General inhibition studies with human tumor cell lines (HCT116 WT and MIA PaCa-2 WT) were performed as

follows: cells were seeded in 60 mm dishes at a density of 1 million cells per dish. After 48 hours, cellular uptakes of [^{3}H]-**MTX** and [^{3}H]-**AGF347** (both 500 nM) were measured over 5 minutes at pH 5.5, 6.8, and 7.2, using the previously mentioned buffers. Uptake experiments were also performed in the presence of an excess (10 μM) of unlabeled **AGF94** (Wang et al., 2011) (blocks PCFT uptake) and/or **PT523** (Rosowsky, 1999) (blocks RFC uptake). The dishes were then washed three times with ice-cold PBS and cells solubilized with 0.5 N NaOH with aliquots counted for radioactivity and assayed for protein concentrations (Lowry et al., 1951). Final values were expressed in pmol[^{3}H]-substrate per mg of protein.

3.2.7 Subcellular Fractionation of Folates.

GlyB, GlyBTII, MIA PaCa-2 NTC, and MIA PaCa-2 MFT KD cells were cultured in complete αMEM supplemented with bovine calf serum, 1% penicillin/streptomycin, and 2 mM L-glutamine (CHO cell lines) or complete RPMI 1640 supplemented with fetal bovine serum, 1% penicillin/streptomycin, and 2 mM L-glutamine (MIA PaCa-2 cell lines) respectively. Prior to incubating with radiolabel, each cell line was depleted of intracellular folates by culturing in complete folate-free RPMI 1640 supplemented with dialyzed fetal bovine serum, 1% penicillin/streptomycin, and 2 mM L-glutamine (i.e. depletion media) for 48 hours. Two T150 flasks per treatment condition were then seeded with 6 million (CHO) or 8 million (MIA PaCa-2) cells in depletion media supplemented with 60 μM adenosine and 10 μM thymidine to a total volume of 30 mL per T150 flask to which 2 μM unlabeled drug and 9 μCi of either [^{3}H]-**MTX** or [^{3}H]-**AGF347** (specific activity of 133.20 cpm/pmol) were added. To measure [^{3}H]-**folic acid** fractionation, folate-depleted cells were instead seeded in complete αMEM or complete RPMI 1640 medium (containing 2.26 μM folic acid) to which 9 μCi of [^{3}H]-folic acid (specific activity of 117.88 cpm/pmol) was added. Cells were allowed to incubate with radiolabel for 48 hours.

After incubation, mitochondrial, cellular, and total fractions were separated by differential centrifugation, essentially as previously described (Clayton and Shadel, 2014). Briefly, cells were harvested by trypsinizing, washed once with PBS, and resuspended in hypotonic resuspension buffer (RSB – 10mM NaCl, 1.5 mg $MgCl_2$, 10mM Tris (pH 7.5)) for 15 minutes. Cells were then lysed with 15 strokes of the B (i.e. "tight-fitting") pestle in a 7 mL Dounce homogenizer. 2.5x mannitol-sucrose buffer (MS – 5.5 mM mannitol, 175 mM sucrose, 12. 5mM Tris (pH 7.5), and 2.5 mM EDTA (pH 8.0)) was then added to a final concentration of 1x MS and an aliquot (i.e. "Total" fraction containing both cytosol and mitochondria) was sampled for radioactivity via scintillation counter and protein via Folin-phenol reagent (Lowry et al., 1951). The homogenized cell suspension was then spun at 3100 rpm for 5 minutes at 4^oC in a Jouan CR4i centrifuge to pellet nuclei and unbroken cells. After collecting the supernatant (containing mitochondria), the nuclei and unbroken cell pellet were resuspended in 1x MS, homogenized with 5 additional strokes, and respun at 3100 rpm. The supernatant was pooled with the supernatant collected earlier and spun at 11,900 rpm at 4^oC for 15 minutes in a Sorvall SS34 rotor to pellet mitochondria. The supernatant (i.e., the cytosol fraction) was collected and aliquots were assayed for protein and radioactivity. The mitochondrial pellet was washed once with 1x MS, repelleted at 11,900 rpm for 15 minutes, and then solubilized in 0.5 M NaOH, after which aliquots were assayed for proteins and radioactivity (i.e. mitochondrial fraction). To assess purities and yields of the cytosolic and mitochondrial fractions, parallel incubations were performed with no drug or radiolabel added, cells were harvested in RSB and MS buffers containing cOmplete Protease Inhibitor Cocktail (Sigma), and each fraction was assayed for lactate dehydrogenase (LDH-cytosolic marker) and succinate dehydrogenase (SDH-mitochondrial marker). LDH was assayed in sodium phosphate buffer (0.03 M, pH 7.4) with

excess of sodium pyruvate (300 µM) and NADH (70 µM) by measuring rate of decrease in absorbance at 340nm (i.e. depletion of NADH). SDH was assayed in potassium phosphate buffer (10 mM, pH 7.5 with 1mM potassium cyanide) with an excess of sodium succinate (20mM) and 2,6-dichlorophenolindophenol (DCPIP) by measuring rate of decrease in absorbance at 600 nm (i.e. reduction of DCPIP). While the mitochondrial fractions were relatively pure (<5% cytosolic contamination – see section 3.3.2), cytosolic fractions were heavily contaminated with lysed mitochondria. As both positive ([^{3}H]-**folic acid**) and negative ([^{3}H]-**MTX**) controls demonstrated the expected phenotypes (see section 3.3.2), data were not corrected.

3.2.8 Polyglutamylation of [^{3}H]-AGF347

Polyglutamates of **AGF347** were studied in cytosolic and mitochondrial fractions of MIA PaCa-2 NTC cells, as previously described with some modifications (Kugel Desmoulin et al., 2011). Briefly, the protocol for subcellular fractionation of folates in section 3.2.7 was modified by addition of 18 µCi (rather than 9 µCi) of [^{3}H]-**AGF347** to each T150 flask (specific activity of 266.40 cpm/pmol). The cytosolic and mitochondrial fractions were then boiled for 10 minutes to denature lysosomal conjugases, spun at 14,000 rpm in a tabletop centrifuge at 0^{o}C for 15 minutes, and the supernatant was analyzed via HPLC (Agilent Infinity 1260 II, Agilent Technologies Inc, Santa Clara, CA) essentially as previously described (Kugel Desmoulin et al., 2011) with minor modifications. Supernatants were injected (200 µL) into a Waters 4 µm Nova-Pak C-18 column (3.9 x 150 mm) with a Nova-Pak 4 µM C-18 guard column. The gradient of 100 mM sodium acetate pH 5.5 (mobile phase A) and acetonitrile (mobile phase B) was initiated with 100% A from 0 to 5 minutes, followed by a linear gradient from 100% A at 5 minutes to 75% A/25% B at 35 minutes. Fractions were automatically collected every minute for the first 5 minutes, every 30 seconds for the next 5 minutes, and every 10 seconds thereafter. Radioactivity

was measured via scintillation counter and total picomoles of each polyglutamate were calculated from the percentage of total radioactivity in each peak and total picomoles of **AGF347** in each compartment, as calculated in subcellular fractionation of folates. To confirm the identities peaks as polyglutamate metabolites of **AGF347**, samples were treated overnight treatment with a preparation of partially purified chicken pancreas conjugase in 0.5 ml of 0.1 M sodium borate, pH 7.8, containing 10 mM β-Me at 32°C to hydrolyze all polyglutamates to the monoglutamyl form (i.e. **AGF347**) (Matherly et al., 1985). Samples were deproteinized by boiling (5 min), then analyzed by HPLC.

3.2.9 Determination of Oxygen Consumption Rate

Oxygen consumption rates (OCR) were determined using a Seahorse XF24 extracellular flux analyzer (Agilent Technologies). HCT116 WT and SHMT2 KO cells were grown in complete folate-free, glycine-replete RPMI 1640 supplemented with 10% dialyzed fetal bovine serum, 1% penicillin/streptomycin, 25 nM leucovorin, 2 mM L-glutamine, and adenosine (60 μM – to abrogate cytotoxicity of drug) and treated with **AGF347** (10 μM) or DMSO for 48 hours. Cells were then seeded into gelatin-coated XF24 cell culture microplates in the same media (containing drug) at a density of 130,000 cells per well with 5 replicate wells per condition and allowed to adhere for 24 hours. OCR was then monitored at baseline and throughout sequential injections of oligomycin (1 μM), carbonyl cyanide-4-(trifluoromethoxy)phenylhydrazone (FCCP - 1 μM) and rotenone/antimycin A (1 μM each) (Mean Son et al., 2017; Minton et al., 2018; Morscher et al., 2018). Baseline OCR consists of the sum of mitochondrial respiration (i.e. oxygen consumed by the electron transport chain) and non-mitochondrial respiration (e.g. oxygen consumed through non-mitochondrial NADPH oxidases, which represents up to 10% of total OCR in most cells (Brand and Nicholls, 2011)).

Mitochondrial respiration functions by pumping protons from the mitochondrial matrix into the intermembrane space through oxidation of NADH, ubiquinone, and cytochrome *c* at complexes I, III, and IV of the electron transport chain, respectively (Jastroch et al., 2010). The electrons from these oxidation reactions eventually flow to oxygen, which is reduced into water (i.e. consumed, hence allowing measurement of OCR as a proxy for mitochondrial respiration) (Jastroch et al., 2010). Most protons then flow down their concentration gradient into the mitochondrial matrix and this energetically favorable reaction is coupled to production of ATP from ADP at the enzyme ATP synthase (Jastroch et al., 2010). However, some protons "leak" back into the mitochondrial matrix through non-ATP synthase mechanisms, as well (Jastroch et al., 2010). As oligomycin blocks ATP synthase (Masaya et al., 1995), treatment with oligomycin resolves mitochondrial respiration into ATP production (which is blocked) and proton leak (which persists). Subsequent treatment with FCCP effectively permeabilizes the inner mitochondrial membrane to protons, dissipating the proton gradient and thus, "uncoupling" ATP production from the electron transport chain altogether (Heytler and Prichard, 1962). The mitochondria, then, achieve maximum OCR as abrogation of the proton gradient removes any energetic resistance to the pumping of protons into the intermembrane space by Complexes I, III, and IV. Finally, treatment with rotenone (which inhibits Complex I) and antimycin A (which inhibits Complex III directly and therefore, Complex IV indirectly) (Kim et al., 1999; Krieger, 2010) terminates all remaining electron transport chain activity, leaving just non-mitochondrial respiration. After completion of this "mitochondrial stress test" (see section 3.3.4), the OCR measured in each section was normalized to the protein concentration in each well calculated after stress test by solubilizing with 0.5 N NaOH and using the Folin-phenol method (Lowry et al., 1951).

3.2.10 Glutathione and ROS

HCT116 WT, SHMT1 KO, and SHMT2 KO cells were seeded (25,000 cells per 96-well plate well for glutathione assay, 1.5 million cells per 60 mm dish for ROS assay) in complete folate-free, RPMI 1640 supplemented with 10% dialyzed fetal bovine serum, 1% penicillin/streptomycin, 25 nM leucovorin, and 2 mM L-glutamine. The cells were allowed to adhere overnight under normoxia (21% O_2, 5% CO_2). Media was then replaced with complete folate-free, *glycine-free* RPMI 1640 supplemented with 10% dialyzed fetal bovine serum, 1% penicillin/streptomycin, 25 nM leucovorin, 2 mM L-glutamine, and adenosine (60 μM – to isolate effects of SHMT2 inhibition vis-a-vis *de novo* purine biosynthesis inhibition). Cells were then treated with 10 μM **AGF291**, **AGF320**, or **AGF347** for 24 hours in parallel incubations under normoxia (21% O_2, 5% CO_2) or hypoxia (0.5% O_2, 5% CO_2) (Ye et al., 2014). Cells were then processed for glutathione pools by an o-phthalaldehyde assay (Senft et al., 2000) (Biovision, San Francisco, CA – Catalog #: K264) or ROS levels by 2',7'-dichlorofluorescin diacetate (H2DCFDA) fluorophore assay (Eruslanov and Kusmartsev, 2010) (Biovision, Catalog #: K936) by kit following the manufacturer's protocols. In the glutathione assay, o-phthaldehyde reacts with the sulfhydryl group of glutathione (reduced-GSH), but not glutathione disulfide (oxidized) (GSSG), to produce fluorescence that can be measured by plate-reader via excitation/emission at 340 nm/420 nm, allowing for quantification of GSH against a standard curve. GSSG may also be quantified by quenching all cellular GSH (but not GSSG) with the kit's proprietary GSH quencher, and subsequently reducing all GSSG into GSH by the kit's proprietary reducing agent mix. In the ROS assay, H2DCFDA enters the cell and is deacetylated into non-fluorescent H2DCF, which interacts with intracellular ROS to yield a fluorescent product detectable by plate-reader via excitation/emission at 495 nm/529 nm. The proprietary ROS inducer provides a

positive experimental control and was included in the ROS assay kit. After assaying ROS, results were normalized to protein concentrations in each well by solubilizing with 0.5 N NaOH and using the Folin-phenol method (Lowry et al., 1951).

3.2.11 Targeted Metabolomics

Targeted metabolomics was performed essentially as previously described in section 2.2.6 (Ducker et al., 2016; Ducker et al., 2017). Briefly, cells (HCT116 MIA PaCa-2) (1 million cells/dish for vehicle-treated samples, 1.5 million cells/dish for drug-treated samples) were seeded in triplicate 60 mm dishes in 5 mL of folate-free RPMI supplemented with 10% dialyzed fetal bovine serum, 1% penicillin/streptomycin, 2 mM L-glutamine, and 25 nM leucovorin. The cells were allowed to adhere for 24 hours, after which 10 μM **AGF291**, **AGF320** or **AGF347**, or a comparable volume of vehicle (DMSO), was added. After drug incubation for 16 hours, the media were aspirated, the cells were washed once with PBS, and *serine-free* folate-free RPMI supplemented with 250 μM [2,3,3-^{2}H]-serine, 10% dialyzed fetal bovine serum, 1% penicillin/streptomycin, 2 mM L-glutamine, and 25 nM leucovorin was added. Vehicle or drugs (10 μM) were also added back in for an additional 24 hours. Incubations were performed at 37^{o}C with 5% CO_2. After 24 hours, the media were aspirated, and cells were washed (3x) rapidly (< 30 s) with 5 mL ice-cold PBS; metabolism was quickly quenched with methanol:water (80:20) at -80^{o}C. Cells were allowed to rock on dry ice for 10 min to cover the entire dish with 80:20 methanol:water (at -80^{o}C), then harvested by scraping and pipetting into 1.5 mL Eppendorf tubes. The tubes were centrifuged to fully extract metabolites into the supernatant with the pellet used for normalization. The supernatants were collected and analyzed by reversed-phase ion-pairing chromatography coupled with negative-mode electrospray-ionization high-resolution mass spectrometry on an AB SCIEX (Foster City, CA) QTRAP 6500 LC-MS/MS system, which

consists of a SHIMADZU (Kyoto, Japan) Nexera ultra-high performance liquid chromatograph (UHPLC) coupled with a hybrid triple quadrupole/linear ion trap mass spectrometer. Raw metabolite values were normalized to total proteins from the post-extraction pellet by solubilizing with 0.5 N NaOH and using the Folin-phenol protein method (Lowry et al., 1951).

3.2.12 *In Vivo* Efficacy Trial with MIA PaCa-2 Tumor Xenografts

Methods for *in vivo* maintenance of MIA PaCa-2 tumor xenografts and drug efficacy evaluations are analogous to those previously described in section 2.2.9. MIA PaCa-2 human pancreatic cancer tumor fragments (30-50 mg) were bilaterally implanted subcutaneously with a 12-gauge trocar in female NCr SCID mice (NCI Animal Production Program stock strain; Charles River Labs #561). The mice were 10 (late-stage) weeks old on day 0 (tumor implant) with average body weights of 19 g. For the efficacy trials, the mice were maintained on a folate-deficient diet from Envigo (TD.00434) or a folate–replete control diet from Lab Diet (#5021) starting 16 days before subcutaneous tumor implant. Mice were supplied with food and water *ad libitum*. Serum folate concentrations were monitored prior to tumor implant and post study by *Lactobacillus casei* bioassay (Varela-Moreiras and Selhub, 1992). The mice in each group (folate-deficient and standard diet) were pooled before non-selective distribution to each group's respective treatment and control arms. Chemotherapy was initiated seven days post-tumor implantation (when tumors had grown to 100-150 mg) with **AGF347**. For both designs, dosing for **AGF347** was 15 mg/kg/injection every 2 days x 8 (total dose of 120 mg/kg); for gemcitabine, dosing was 120 mg/kg/injection every 4 days x 4 (total dose of 480 mg/kg). The AGF compound was dissolved in 5% ethanol (v/v), 1% Tween-80 (v/v), and 0.06% $NaHCO_3$ and sterile H_2O; the GEM clinical stock was prepared per insert instructions with sterile 0.9% NaCl. Both drugs were administered IV (0.2 ml/injection).

3.2.13 *In Vivo* Metabolomics.

Of 8 mice each in the treatment and control arms of the *in vivo* study, 3 were randomly designated for metabolomics studies with the remaining 5 mice used to determine efficacy. Six hours after the 6th dose of **AGF347** (when control mice tumors reached 2000 mg, mandating euthanasia), both treated and control groups of metabolomics mice were euthanized and tumors were removed and immediately frozen in liquid nitrogen for LC-MS analysis. Frozen isolated tumors were weighed, then 50 mg tissue was disrupted using a cryomill (Retsch) and lysed in 1 mL ice-cold 40:40:20 acetonitrile:methanol:water. Solids were precipitated, spun down, and re-extracted with 1 mL lysis buffer. Combined supernatants were dried down and resuspended in water to a concentration of 50 mg/mL (original tissue mass) before analysis by LC-MS. Samples were run on a ThermoElectron Corporation Exactive mass spectrometer operating in negative ion mode as previously described (Lu et al., 2010). Separation was accomplished by reverse phase ion-pairing chromotagraphy using a 100 mm/ 2.5 μm Synergi Hydro-RP C18 column (Phenomenex). Individual metabolites were identified from spectral data using the MAVEN software suite coupled with retention time information from standards (Clasquin et al., 2012).

3.2.14 Statistics.

All data shown reflect at least three biological replicates unless noted otherwise (e.g. targeted metabolomics data, which reflect three technical triplicates measured in single experiments). All statistical analyses were performed by the Karmanos Cancer Institute Biostatistics Core. The expression levels were assessed for the normality assumption. When the expression levels were positive, the $\log_2$ transformation was used, while the square root transformation was instead applied when the expression levels included zero values. P-values were not adjusted for multiple comparisons.

3.3 Results

3.3.1 Determination of Plasma Membrane Folate Transporters and Kinetics

Our initial characterization of **AGF291**, **AGF320**, and **AGF347** (**Table 2.1**) revealed inhibition of proliferation of both PCFT-expressing R2/PCFT4 and RFC-expressing PC43-10 CHO cells, suggesting uptake by both PCFT and RFC. To confirm PCFT- and RFC-mediated uptake, we measured the impact of unlabeled **AGF291**, **AGF320**, and **AGF347** on uptake of [^{3}H]-**MTX** by both CHO cell lines (**Figure 3.2 – A,B**). **PMX**, **AGF94** (blocks PCFT mediated uptake (Hou et al., 2017; Wilson et al., 2016) – see section 1.3.2) and **PT523** (blocks RFC mediated uptake (Wang et al., 2010) – see section 1.3.1) were used as controls. Under ideal transport conditions (Desmoulin et al., 2012a) for PCFT (pH 5.5) and RFC (pH 7.2, anion-free buffer), adding 10 μM competitor reduced [^{3}H]-**MTX** uptake in the CHO cell lines to background (i.e. R2) levels, confirming uptake of **AGF291**, **AGF320**, and **AGF347** by both transporters. To extend these studies into our human tumor cell line models, we performed analogous experiments with both [^{3}H]-**MTX** and [^{3}H]-**AGF347** in the presence or absence of excess unlabeled **AGF94** and/or **PT523** to gauge the relative contribution of each transporter to total uptake. As expected, experiments at pH 5.5 and 7.2 revealed predominant uptake of both substrates by PCFT and RFC, respectively (**Figure 3.3 - A, C, D, F, G, I**). At pH 6.8, representative of the tumor microenvironment (Stubbs et al., 2000), uptake of [^{3}H]-**MTX** and [^{3}H]-**AGF347** was significantly inhibited by both **PT523** and **AGF94**, confirming transport by both RFC and PCFT (**Figure 3.3 – B, E, H).** RFC in particular was especially critical for uptake in MIA PaCa-2 cells (**Figure 3.3 – B**), as evidenced by a significant decrease in uptake from samples treated with **AGF94** to samples treated with **PT523**.

Next, we assessed RFC and PCFT transport kinetics of **AGF291**, **AGF320**, and **AGF347**

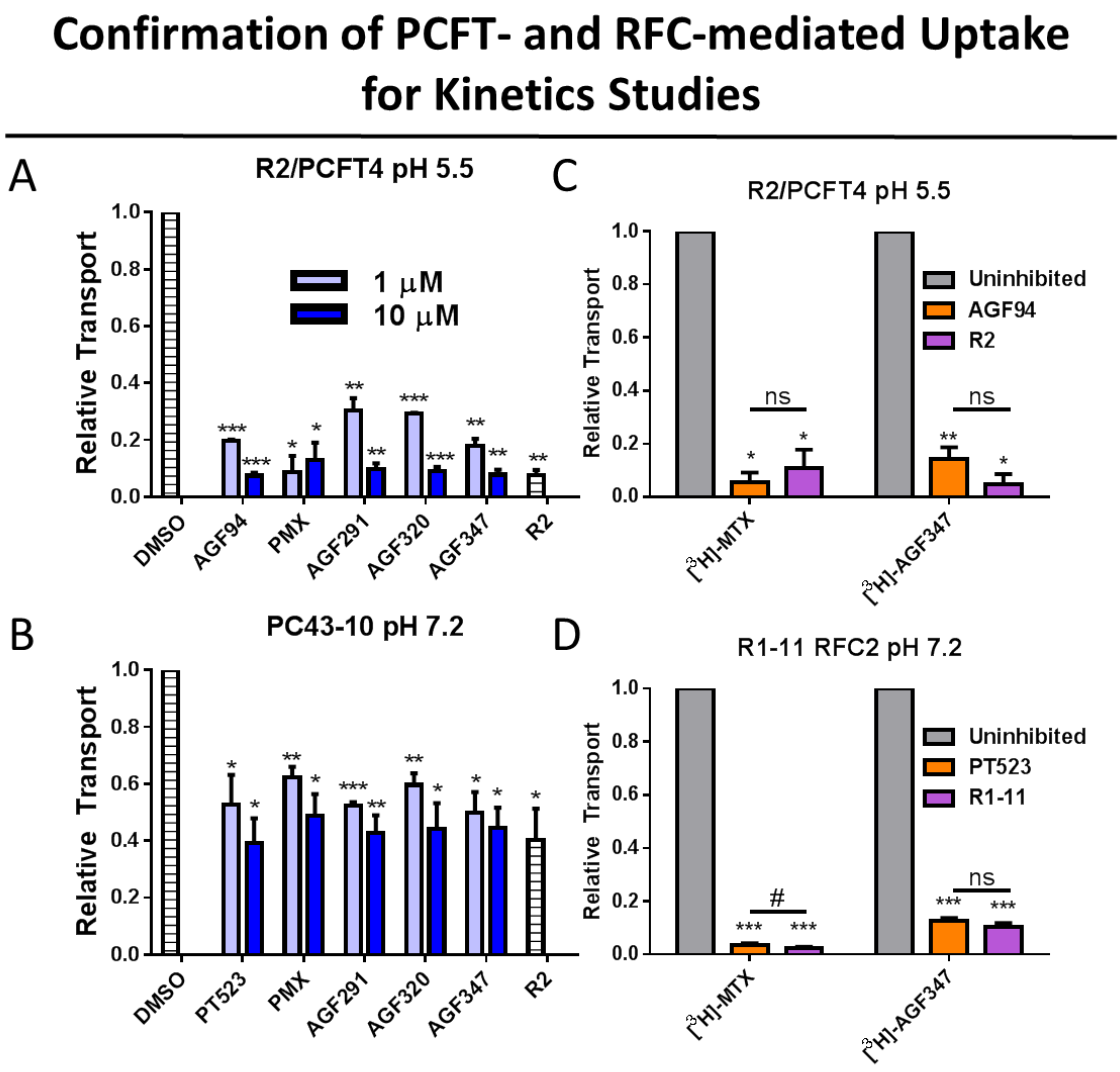

Figure 3.2 RFC- and PCFT-mediated uptake in R2/PCFT4, PC43-10, and R1-11 RFC2 Cells. (A,B) Uptake over five minutes of 0.5 μM [^{3}H]-**MTX** in R2/PCFT4 (expressing PCFT – A) and PC43-10 (expressing RFC – B) CHO cells measured in the presence of vehicle (i.e. DMSO) or unlabeled inhibitor, as compared to uptake in plasma membrane folate transporter-null R2 cells. (C,D) Uptake over five minutes of 0.5 μM [^{3}H]-**MTX** and 0.5 μM [^{3}H]-**AGF347** in R2/PCFT4 cells (C) and R1-11 RFC2 cells (D) as compared to the corresponding plasma membrane folate transporter-null parental cell lines R2 and R1-11 respectively. Significant differences are denoted by # or * with the number of symbols indicating the degree of significance (# denotes $p < 0.1$, * denotes $p < 0.05$, ** denotes $p < 0.01$, *** denotes $p < 0.001$).

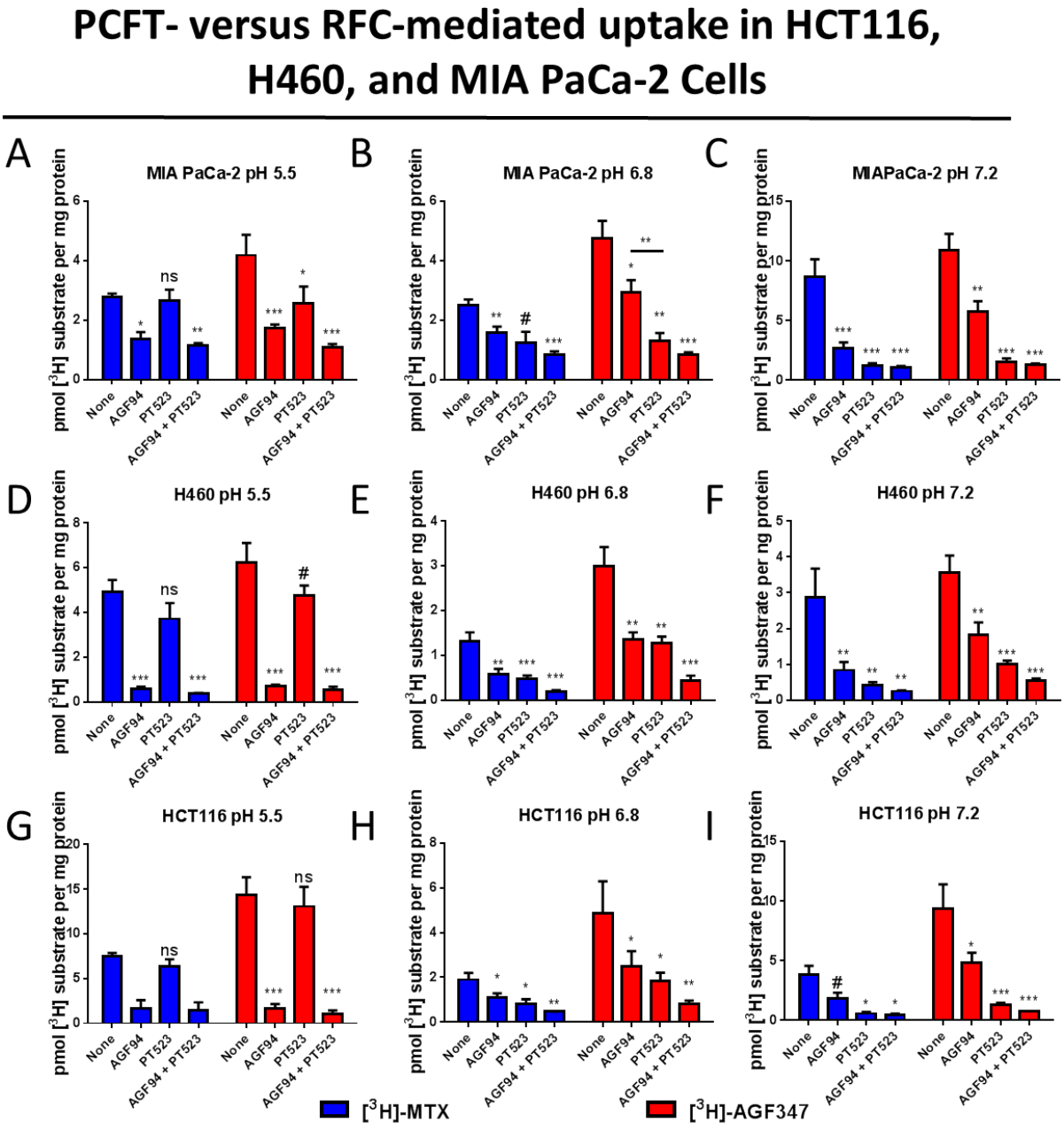

Figure 3.3 RFC- and PCFT-mediated uptake in HCT116, H460, and MIA PaCa-2 Cells. Uptake over five minutes of 0.5 µM [^{3}H]-**MTX** and 0.5 µM [^{3}H]-**AGF347** in the presence of excess (10 µM) unlabeled **AGF94** (blocks PCFT-mediated uptake) and/or **PT523** (blocks RFC-mediated uptake) in MIA PaCa-2 (A-C), H460 (D-F), and HCT116 (G-I) cells at pH 5.5 (PCFT-optimum), pH 6.8 (tumor microenvironment), and pH 7.2 (anion-free buffer, RFC-optimum). Significant differences are denoted by # or * with the number of symbols indicating the degree of significance (# denotes p <0.1, * denotes p<0.05, ** denotes p<0.01, *** denotes p<0.001).

in cell lines expressing each transporter individually. For PCFT, we used R2/PCFT4 CHO cells, as **AGF94** potently inhibited (decreased by 85-95%) uptake of both radiolabels (**Figure 3.2 – C**), confirming robust PCFT transport. However, the analogous experiment with **PT523** and PC43-10 CHO cells revealed more modest inhibition (decreased by 60%), suggesting less-than-ideal RFC activity for kinetics measurements (**Figure 3.2 - B**). Therefore, we instead used the R1-11 (transporter-null) and R1-11-RFC2 (RFC-expressing) engineered isogenic HeLa sublines (Ravindra et al., 2018). In the latter, **PT523** potently inhibited (decreased by 87-97%) uptake of both radiolabels (**Figure 3.2 - D**), confirming robust RFC transport. K_m and V_{max} values for [^{3}H]-**MTX** and [^{3}H]-**AGF347** are given in **Table 3.1**. As expected from the greater uptake of [^{3}H]-**AGF347** than [^{3}H]-**MTX** in both human tumor cell lines at all pH values (**Figure 3.3**), [^{3}H]-**AGF347** had an 1.5-fold increased affinity for RFC (K_m - 0.399 μM vs 0.609 μM respectively) and a 5.5-fold increased affinity for PCFT (K_m - 0.060 μM vs 0.336 μM respectively) compared to [^{3}H]-**MTX** (**Table 1**)**.** Using the K_m and V_{max} values derived from these studies, we calculated K_i values against **MTX** for all novel compounds, as well as **AGF94** and **PMX**. **AGF291**, **AGF320**, and **AGF347** are roughly equivalent substrates for RFC based on their Ki values (K_i range- 0.205 μM to 0.278 μM) and 2- to 3-fold better than PMX (K_i = 0.585 μM). For PCFT, **AGF347** (K_i = 0.140 μM) was a 2- to 2.5-fold better substrate than **AGF291** (K_i = 0.350 μM) and **AGF320** (K_i = 0.296 μM) and on par with **AGF94** (K_i = 0.148 μM) and **PMX** (K_i = 0.112 μM).

3.3.2 Subcellular Compartmentation of [^{3}H]-AGF347

Having established the plasma membrane transport profiles of **AGF291**, **AGF320**, and **AGF347**, we next sought to assess their mitochondrial uptake using [^{3}H]-**AGF347** as a model. In particular, as MFT was established as the only known transporter of folates into the

Table 3.1: Transport Kinetics

Transporter	**RFC**			**PCFT**		
Constant	K_m (µM)	V_{max} (µMol/min)	K_i (**MTX**)	K_m (µM)	V_{max} (µMol/min)	K_i (**MTX**)
MTX	0.609 (0.011)	71.7 (3.15)	ND	0.336 (0.092)	467.3 (277.6)	ND
PMX	ND	ND	0.585 (0.067)	ND	ND	0.056 (0.002)
AGF94	ND	ND	1.620 (0.182)	ND	ND	0.074 (0.029)
AGF291	ND	ND	0.278 (0.048)	ND	ND	0.175 (0.081)
AGF320	ND	ND	0.205 (0.052)	ND	ND	0.148 (0.050)
AGF347	0.399 (0.122)	87.9 (50.3)	0.252 (0.058)	0.06 (0.02)	190.1 (55.6)	0.070 (0.002)

Transport assays were performed over five minutes using the engineered CHO cell line R2/PCFT4 (expresses PCFT only) and the engineered HeLa-derivative cell line R1-11 RFC2 (expresses RFC only). Calculations of K_m and V_{max} were performed with concentrations of [^{3}H]-**AGF347** or [^{3}H]-**MTX** from 20 nM to 500 nM (R2/PCFT4 at pH 5.5) or 250 nM to 5 µM (R1-11 RFC2 at pH 7.2). Analysis was carried out by Lineweaver-Burk plots. Using the average K_m and V_{max} values obtained from these experiments, K_i values for each of the drugs relative to 0.5 µM [^{3}H]-**MTX** were calculated by Dixon plot using concentrations of cold competitor (i.e. drug) from 0 to 500 nM (R2/PCFT4 at pH 5.5) or 0 to 1 µM (R1-11 RFC2 at pH 7.2).

mitochondrial matrix (as previously discussed in section 1.3.4) , we sought to assess whether MFT played a role in mitochondrial uptake of [^{3}H]-**AGF347**. To that end, we transfected human MFT into the MFT-inactive GlyB CHO cells (McCarthy et al., 2004) to generate the GlyBTII cell line (**Figure 3.1 - A**). In addition, we also generated NTC and MFT KD MIA PaCa-2 cell lines (**Figure 3.1 - B)** as human tumor models. [^{3}H]-**Folic acid** was used as a positive control as inactivation of MFT reduces mitochondrial folate accumulation by 99% (McCarthy et al., 2004). [^{3}H]-**MTX** was used as a negative control as **MTX** does not enter the mitochondria (Lin et al., 1993). All cell lines were cultured in glycine-replete, folate-free media for 48 hours to deplete intracellular folate pools (as discussed in section 3.2.7). 2.26 µM [^{3}H]-**folic acid**, 2 µM [^{3}H]-**MTX**, or 2 µM [^{3}H]-**AGF347** were then added for an additional 48 hours, with [^{3}H]-**MTX** and [^{3}H]-**AGF347** incubations also containing 60 µM adenosine and 10 µM thymidine to abrogate any cytotoxic drug effects (see **Figure 2.4** and (Deng et al., 2008)). Cytosolic and mitochondrial fractions were subsequently resolved by differential centrifugation (Clayton and Shadel, 2014) with radiolabel in each fraction quantified (**Figure 3.4 – A-C**) and normalized to fraction protein (**Table 3.2, Figure 3.4 – D-F**). As expected, all radiolabels showed no biologically relevant difference in total (**Figure 3.4 - D**) or cytosolic (**Figure 3.4 - E**) accumulations between the MFT-functional cell lines (MIA PaCa-2 NTC and GlyBTII) and their corresponding MFT KD/KO counterparts (MIA PaCa-2 MFT KD and GlyB respectively). In the mitochondrial fraction (**Figure 3.4 – F**), [^{3}H]-**folic acid** accumulation was significantly diminished in the MFT KD/KO cell lines compared to their MFT-functional counterparts, consistent with MFT-mediated uptake of [^{3}H]-**folic acid**-derived [^{3}H]-THF. Also as expected, no significant difference was seen with mitochondrial [^{3}H]-**MTX** accumulation as all cell lines accumulated minimal amounts of mitochondrial [^{3}H]-**MTX**. This is consistent with a level of cytosolic contamination

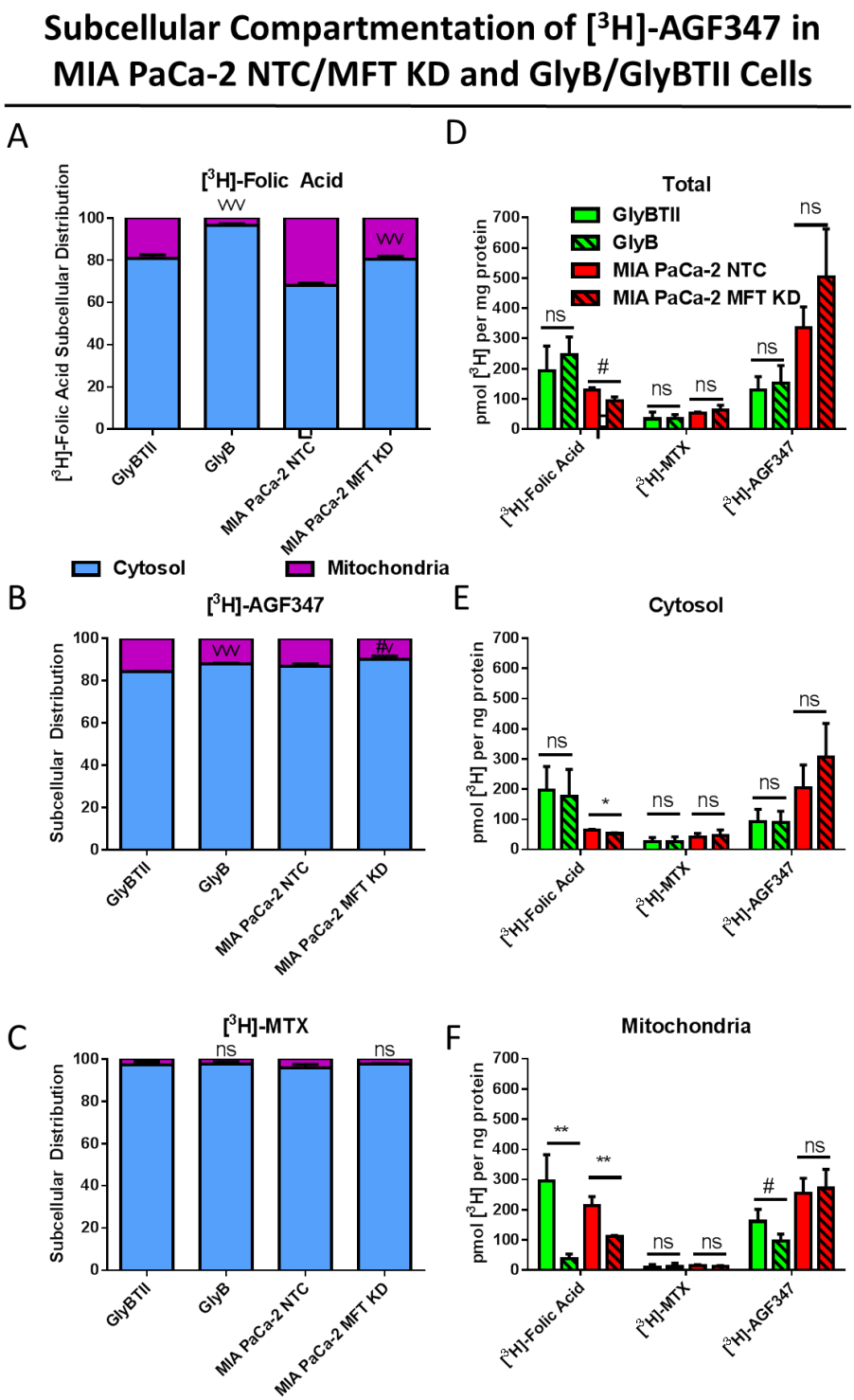

Figure 3.4 – Subcellular Fractionation of [^{3}H]-Folic Acid, [^{3}H]-MTX, and [^{3}H]-AGF347 in MIA PaCa-2 NTC, MIA PaCa-2 MFT KD, *glyB*, and *glyBTII* Cell Lines. Cells were treated for 48 hours with radiolabel (2.26 µM [^{3}H]-**folic acid**, 2.0 µM [^{3}H]-**MTX**, or 2.0 µM-**AGF347**) and fractionated per protocol in section 3.2.7. Distribution of radiolabel in cytosol and mitochondria was quantified (A-C). Total cellular uptake of radiolabel (D) and compartment-specific uptake (E-F) was normalized to cellular and compartment-specific protein level. Results represent mean ± standard deviation of at least three biological replicates. Significant differences are denoted by # or * with the number of symbols indicating the degree of significance (# denotes $p < 0.1$, * denotes $p < 0.05$, ** denotes $p < 0.01$, *** denotes $p < 0.001$).

Table 3.2: Subcellular Distribution of Folates						
Cell Line	**MIA PaCa-2 NTC**			**MIA PaCa-2 MFT KD**		
Compartment	Total	Cytosol	Mito.	Total	Cytosol	Mito.
[^{3}H]-**Folic Acid**	129.57 (7.3)	63.50 (3.25)	214.25 (29.35)	92.33 (14.06)	53.03 (2.49)	111.56 (3.92)
[^{3}H]-**MTX**	52.02 (4.46)	40.63 (12.87)	13.91 (4.54)	64.16 (14.76)	46.78 (18.32)	12.09 (2.91)
[^{3}H]-**AGF347**	336.28 (68.28)	205.02 (75.29)	254.18 (50.14)	502.80 (160.04)	306.09 (111.73)	271.17 (63.01)
Cell Line	**GlyB**			**GlyBTII**		
Compartment	Total	Cytosol	Mito.	Total	Cytosol	Mito.
[^{3}H]-**Folic Acid**	193.43 (81.58)	175.96 (89.56)	38.99 (14.33)	245.56 (59.08)	196.68 (78.45)	294.59 (87.97)
[^{3}H]-**MTX**	33.81 (22.20)	26.35 (15.83)	10.65 (12.37)	35.44 (12.05)	27.19 (13.06)	9.95 (9.25)
[^{3}H]-**AGF347**	129.99 (43.42)	89.62 (37.32)	96.53 (23.00)	152.01 (58.27)	91.28 (42.05)	161.15 (40.65)
Cells were treated for 48 hours with radiolabel (2.26 µM [^{3}H]-folic acid, 2.0 µM [^{3}H]-**MTX**, or 2.0 µM-**AGF347**) and fractionated per protocol in section 3.2.7. Total cellular ("Total"), cytosolic ("Cytosol"), and mitochondrial ("Mito.") radiolabel was quantified and normalized to compartment-specific protein level. Results represent mean ± standard deviation of at least three biological replicates.						

of the mitochondrial fraction (**Table 3.3**). [^{3}H]-**AGF347**, however, yielded an intermediate phenotype as compared to [^{3}H]-**MTX** and [^{3}H]-**folic acid**. While the mitochondrial accumulation of [^{3}H]-**AGF347** was significantly decreased in MFT-null GlyB cells as compared to GlyBTII cells, consistent with MFT-mediated uptake, this difference was not recapitulated in the MIA PaCa-2 sublines in spite of MFT KD approximating 20% of wild-type levels. Moreover, the concentration of [^{3}H]-**AGF347** exceeded the concentration of [^{3}H]-**folic acid** in the mitochondrial fraction of GlyB cells, suggesting an alternate transport mechanism for the former in addition to MFT. These results establish that **AGF347** uptake into the mitochondria is mediated partially, but not completely, by MFT.

As it had previously been reported that accumulation of folates in the mitochondria and cytosol was dependent upon polyglutamylation by the respective compartment-specific isoforms of FPGS (Lawrence et al., 2014), we next sought to assess whether[^{3}H]-**AGF347** was similarly polyglutamylated in each compartment. Using MIA PaCa-2 NTC mitochondrial and cytosolic fractions, we resolved polyglutamates via HPLC. In addition to the monoglutamate (PG_1) parent compound (i.e., [^{3}H]-**AGF347**), six polyglutamyl metabolites (PG_{2-7}) were resolved in the cytosolic fraction (**Figure 3.5 - A**) and three predominant polyglutamyl metabolites (PG_{5-7}) were resolved in the mitochondrial fraction (**Figure 3.5 - B**). This reveals near-complete (98%) polyglutamylation of [^{3}H]-**AGF347** in both compartments with distinct polyglutamyl populations in each (**Table 3.4**). To confirm identity of the peaks as polyglutamyl metabolites of [^{3}H]-**AGF347**, aliquots of the cytosolic fraction were treated with chicken pancreas conjugase (Kugel Desmoulin et al., 2011), which reverted the polyglutamyl metabolites back to the monoglutamate [^{3}H]-**AGF347** (**Figure 3.5 - C**). Collectively, these results establish that **AGF347** is an excellent polyglutamylation substrate in both the mitochondria and cytosol.

Table 3.3: Purity of Subcellular Fractions		
MIA PaCa-2 NTC	Cytosol	Mitochondria
LDH Activity	96.92 (1.69)	3.08 (1.69)
SDH Activity	77.53 (6.06)	22.47 (6.06)
MIA PaCa-2 MFT KD	Cytosol	Mitochondria
LDH Activity	97.22 (0.49)	2.78 (0.49)
SDH Activity	83.78 (3.63)	16.22 (3.63)
GlyB	Cytosol	Mitochondria
LDH Activity	99.62 (0.06)	0.38 (0.06)
SDH Activity	76.94 (10.93)	23.07 (10.93)
GlyBTII	Cytosol	Mitochondria
LDH Activity	98.48 (2.15)	1.52 (2.15)
SDH Activity	78.04 (2.64)	21.96 (2.64)
Subcellular fractions were generated per section 3.2.7. Lactate dehydrogenase (LDH) and succinate dehydrogenase (SDH) were assayed spectrophotometrically as markers for cytosol and mitochondria, respectively. Results reflect three biological replicates and the percentage of total enzyme activity in each fraction (mean ± standard deviation) is given above.		

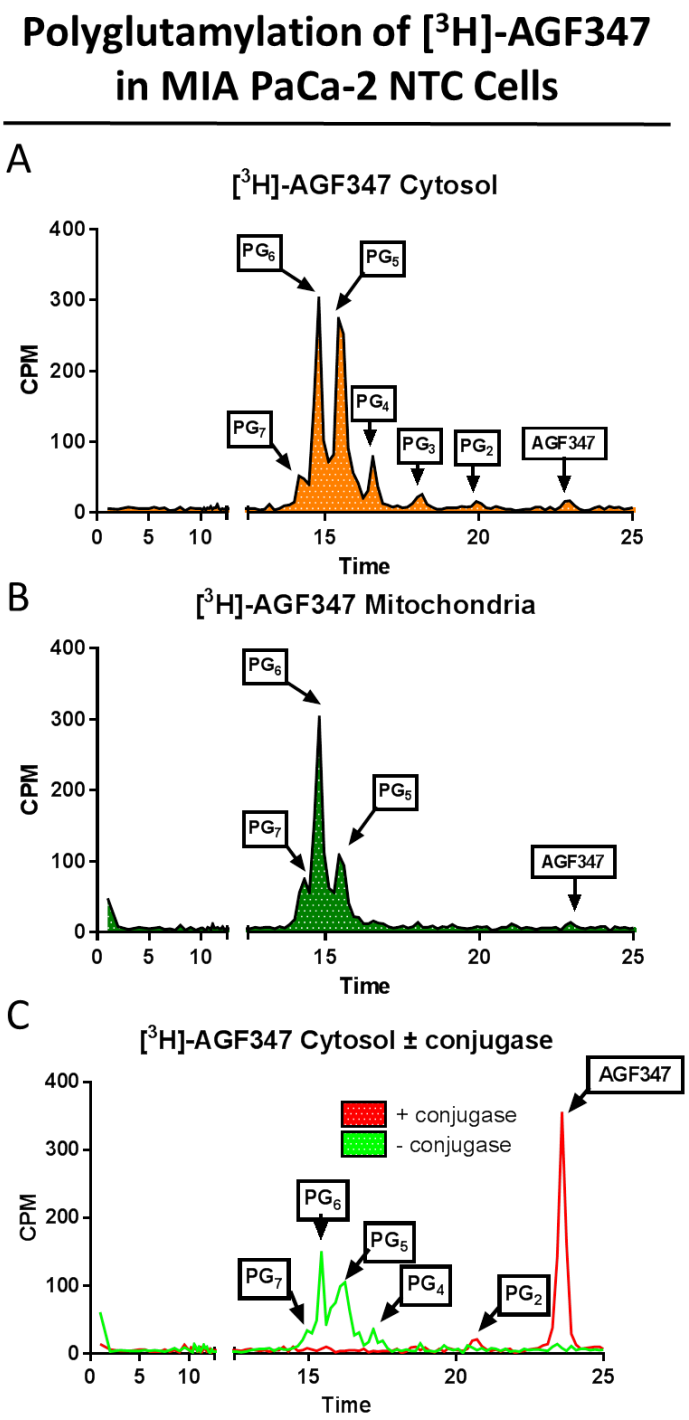

Figure 3.5 Polyglutamylation of [^{3}H]-AGF347 in MIA PaCa-2 NTC Cell Line. MIA PaCa-2 NTC cells were treated with 2.0 µM [^{3}H]-**AGF347** for 48 hours with cytosolic and mitochondrial fractions resolved per section 3.2.8. Polyglutamyl derivatives (PG_n) of [^{3}H]-**AGF347** were resolved in the cytosolic (A) and mitochondrial (B) fractions by HPLC. To confirm identities of peaks as polyglutamyl derivatives of [^{3}H]-**AGF347**, aliquots of the cytosolic fraction were treated with conjugase, restoring the polyglutamyl forms to the parent monoglutamate form (i.e., PG_1 or [^{3}H]-**AGF347**).

Table 3.4: Subcellular [^{3}H]-AGF347 Polyglutamate Distribution in MIA PaCa-2 NTC Cells

	Percentage		Total (pmol/mg protein)	
	Cytosol	Mitochondria	Cytosol	Mitochondria
PG_7	8%	16%	16.40	40.67
PG_6	33%	48%	67.66	122.01
PG_5	42%	26%	86.11	66.09
PG_4	8%	4%	16.40	10.17
PG_3	4%	3%	8.20	7.63
PG_2	2%	1%	4.10	2.54
PG_1 (**[^{3}H]-AGF347**)	2%	2%	4.10	5.08

MIA PaCa-2 NTC cells were treated with 2.0 μM [^{3}H]-AGF347 for 48 hours with cytosolic and mitochondrial fractions resolved and polyglutamyl derivatives quantified per protocol in section 3.2.8**.** Percentage (left) and total radiolabel normalized to compartment-specific protein (right) are given above.

3.3.3 Effects Secondary to Inhibition of Cytosolic *De Novo* Purine Biosynthesis

Having established plasma membrane and mitochondrial transporter profiles, we then interrogated cellular pharmacodynamics of **AGF291**, **AGF320**, and **AGF347**. As we had previously established in section 2.3.5 that these drugs all inhibited SHMT2 in the mitochondria and GARFTase and/or AICARFTase in cytosolic purine biosynthesis, we sought to assess the potential downstream effects of targeting these enzymes, starting with purine biosynthesis via targeted metabolomics. HCT116, H460, and MIA PaCa-2 cells were treated with 10 μM **AGF291**, **AGF320**, **AGF347**, or an equivalent volume of DMSO for 48 hours and processed for LC-MS analyses of adenine nucleotide species per protocol in section 3.2.11. Results for drug-treated WT cells were compared to vehicle (i.e. DMSO) treated WT and, for HCT116, SHMT2 KO cells. H460 SHMT2 KD cells were compared to H460 NTC cells.

After 48 hours of drug treatment, adenine nucleotides were suppressed in both HCT116 and MIA PaCa-2 cell lines with greater decreases in AMP (~50%) and ADP (~50%) than ATP (~25%) in HCT116 (**Figure 3.6 - A**) and roughly equal (~50%) suppression in MIA PaCa-2 (**Figure 3.6 - C**). However, adenine nucleotide pools in H460 cells (**Figure 3.6 – B**) were only nominally affected with drug treatment, as AMP pools actually increased (~60%), ADP pools decreased (10-50%), and ATP pools remained generally unchanged. Interestingly, SHMT2 KD alone in these cells effected a significant decrease (25-50%) in all three adenine nucleotide pools. Taken together with the protection data (see section 2.3.2) which confirmed that adenosine was essential to rescue drug effects in all three cell lines, these data suggest that the drugs may be selectively depleting subcellular adenine nucleotide pools that are not captured in the total cellular metabolomics data captured above, particularly in the H460 cell line.

As **PMX**, which inhibits AICARFTase in addition to TS, had previously been shown to

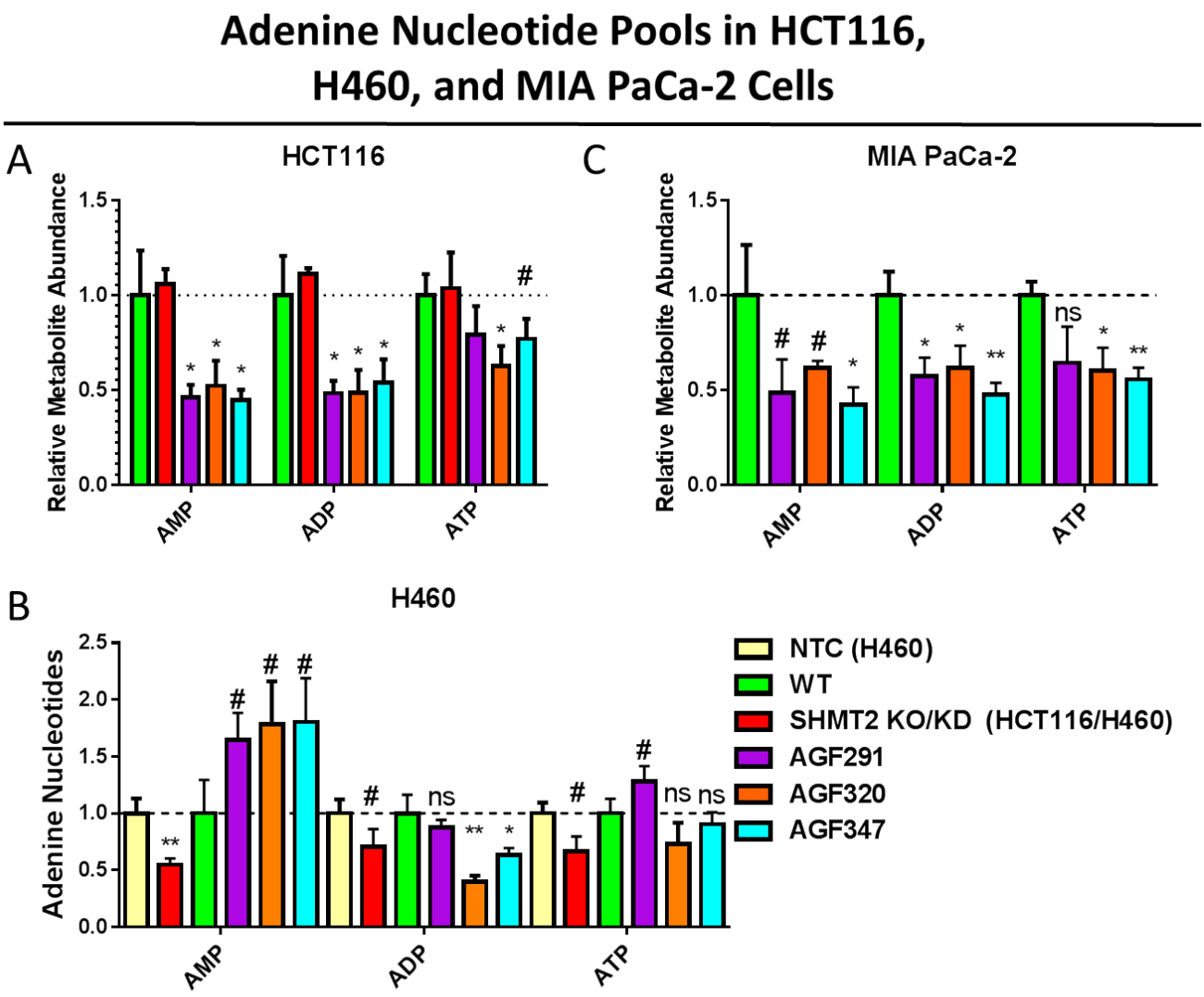

Figure 3.6 Adenine Nucleotide Pools in HCT116, H460, and MIA PaCa-2 Cells. AMP, ADP, and ATP in WT, SHMT2 KO/KD (HCT116/H460, respectively), and **AGF291**-, **AGF320**-, and **AGF347**-treated HCT116 (A), H460 (B), and MIA PaCa-2 (C) were quantified per protocol in section 3.2.11. Cells were treated with 10 µM drug or equivalent volume of DMSO for 48 hours and then processed for metabolomics analysis. Results represent mean ± standard deviation of three technical replicates. Significant differences are denoted by # or * with the number of symbols indicating the degree of significance (# denotes p <0.1, * denotes p<0.05, ** denotes p<0.01, *** denotes p<0.001).

induce accumulation of AICAR (ZMP), subsequently activating AMPK and consequently downregulating the pro-survival mTOR pathway (as discussed previously in section 1.4.2), we sought to assess whether our drugs might have the same effect as **AGF291**, **AGF320**, and **AGF347** all induced striking accumulations of AICAR (**Figure 2.6 – D-F**). HCT116 and MIA PaCa-2 WT cells were treated with drug for 48 hours and compared to vehicle- and AICAR-treated WT cells and, for HCT116, vehicle-treated SHMT2 KO cells as controls. Cells were then harvested and probed for activation of AMPK, Raptor, and both p70 and p85 isoforms of S6K1 (mTOR effector protein) by Western blots, as described in section 3.2.4.

In HCT116 cells (**Figure 3.7 - A**), SHMT2 KO and treatment with AICAR both induced activation (i.e. hyperphosphorylation – 12% and 40% respectively) of AMPK with the latter accompanying suppression of S6K1 (i.e., hypophosphorylation – 78% at p70-S6K1 and 83% at p85-S6K1). No effect on AMPK was seen in cells treated with **AGF291**, **AGF320**, or **AGF347**. However, inhibition of S6K1 (45% at p70-S6K1 and 17.5% at p85-S6K1) was noted with **AGF291** treatment, perhaps signifying that a combination of purine depletion (Hoxhaj et al., 2017) and AICAR/ZMP-induced AMPK activation may be primarily regulating mTOR in these cells.Interestingly, this S6K1 inhibition by **AGF291** was not recapitulated by **AGF320** or **AGF347**, which induce similar perturbations in cellular purine pools (**Figure 3.6 - A**), suggesting potential crosstalk from other cell signaling pathways (see below). mTOR inhibition by **AGF291** (i.e. hyperphosphorylation) in HCT116 cells was better resolved by loading twice the protein (see section 3.2.4) in a second blot (**Figure 3.7 - B**), which confirmed modest inhibition (i.e. hyperphosphorylation - 65%). In the MIA PaCa-2 cells (**Figure 3.7 - C**), only AICAR treatment activated AMPK (40%) and inhibited S6K1 (66% at p70-S6K1 and 83% at p85-S6K1). As there was no drug effect at either AMPK or S6K1 in MIA PaCa-2 cells, we did

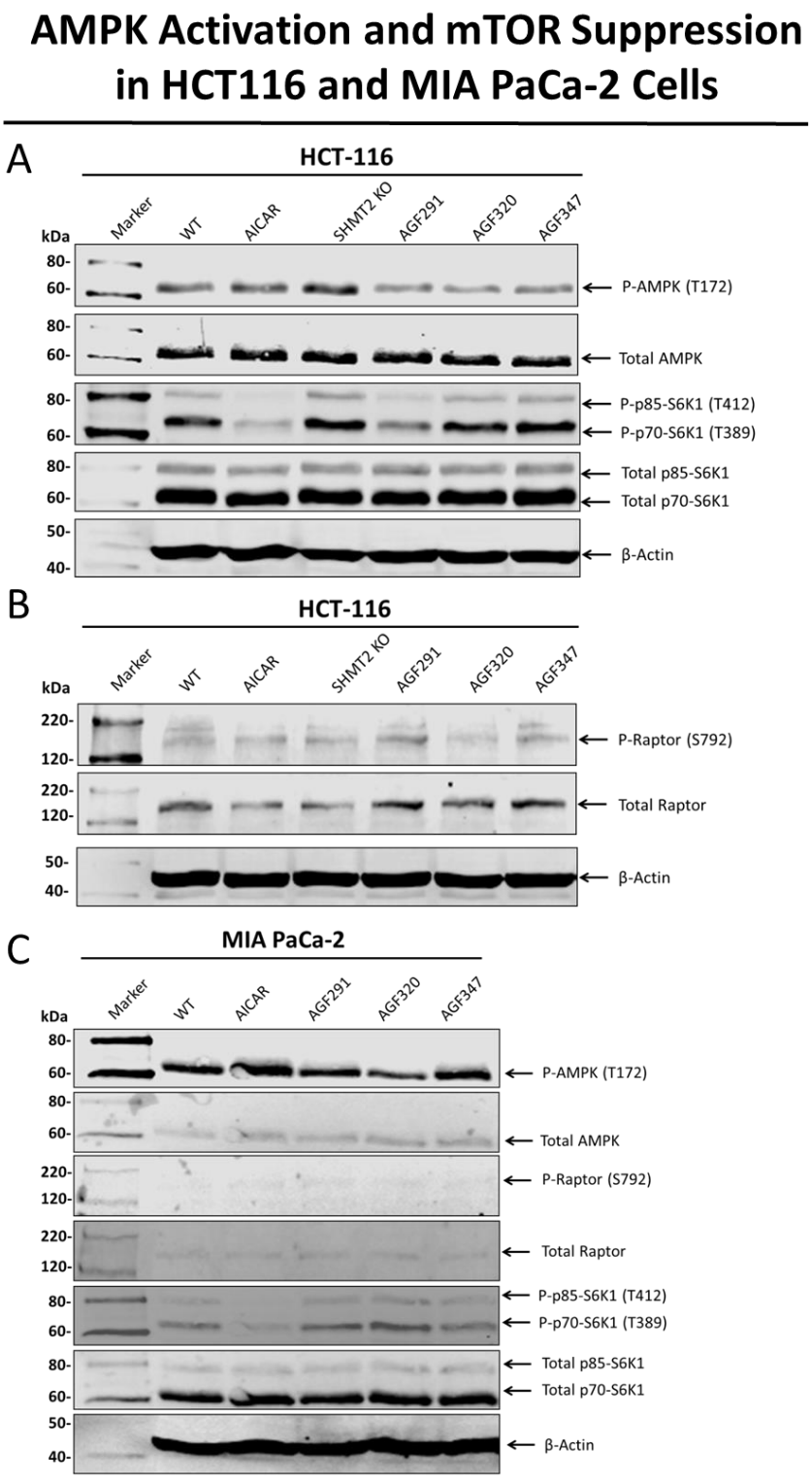

Figure 3.7 Activation of AMPK and Inhibition of mTOR in HCT116 and MIA PaCa-2 Cells. HCT116 and MIA PaCa-2 cells were analyzed for AMPK, mTOR (via Raptor), and S6K1 (mTOR effector) activation by Western Blot per protocol in section 3.2.4. HCT116 cell lysates were probed with 50 µg loaded (A) for AMPK and S6K1 and 100 µg loaded (B) for mTOR (via Raptor). MIA PaCa-2 cell lysates were probed with 50 µg loaded (C) for all proteins.

not further interrogate mTOR inhibition as we did with HCT116 cells. However, both HCT116 and MIA PaCa-2 are K-Ras driven, and K-Ras mutant cancers have been shown to crosstalk with mTOR signaling (Liang et al., 2018; Mann et al., 2016) independent of drug treatment. Taken together with the modest inhibition of mTOR and S6K1 only by **AGF291** in HCT116 cells, it is likely that mTOR suppression secondary to treatment with **AGF291**, **AGF320**, and **AGF347** plays at most only a minor role in the efficacy of these compounds.

3.3.4 Effects Secondary to Inhibition of Mitochondrial One-Carbon Metabolism

Next, we assessed potential cellular effects secondary to inhibition of SHMT2. As SHMT2 had been established to play a critical role in complex I assembly via methylation of select mitochondrial tRNAs with SHMT2 KO cells displaying respiratory deficiency (Lucas et al., 2018; Morscher et al., 2018), we sought to assess whether the ATP suppression in HCT116 cells (**Figure 3.6 - A**) seen with all three compounds could at least in part stem from impairment of mitochondrial respiration secondary to SHMT2 inhibition. To assess mitochondrial respiration, we measured OCR via the Seahorse XF-24 Extracellular Flux analyzer (per the protocol in section 3.2.9). HCT116 cells were pre-treated with either DMSO (WT and SHMT2 KO) or **AGF347** (WT) for 48 hours in glycine-replete media with 60 μM adenosine to abrogate cytotoxicity. Cells were then seeded into Seahorse Assay plates, allowed to adhere overnight, and subjected to a mitochondrial stress test the following day (**Figure 3.8 – A,B**). Consistent with their previously reported phenotype (Morscher et al., 2018), the SHMT2 KO cells exhibited decreased respiratory capacity relative to WT. **AGF347**-treated cells, however, did not recapitulate the phenotype of the SHMT2 KO cells, suggesting lack of respiration impairment. These results establish that **AGF347** does not inhibit sufficient SHMT2 *in vitro* to inhibit mitochondrial respiration and are consistent with an earlier report demonstrating even minimal,

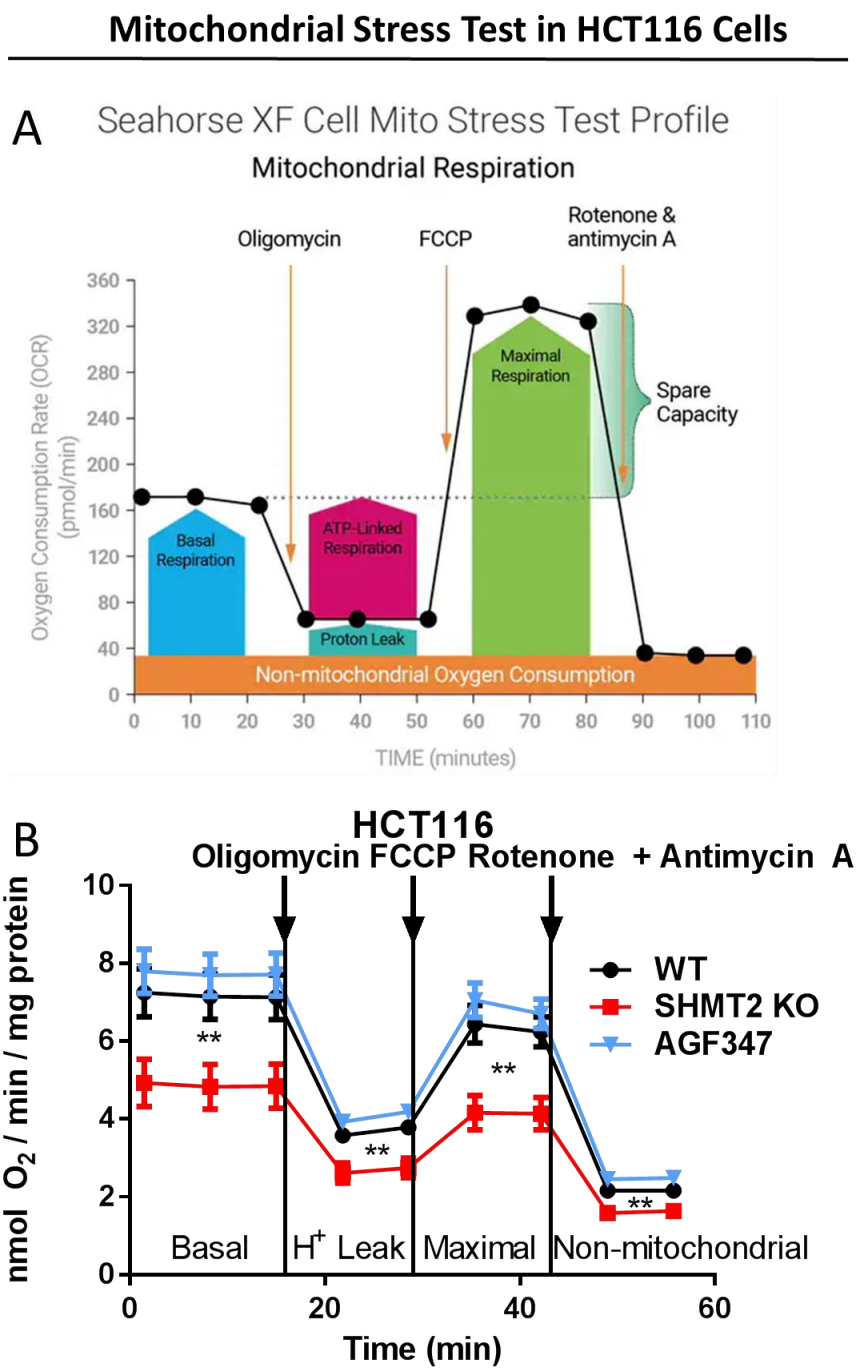

Figure 3.8 Mitochondrial Stress Test in HCT116 Cells. HCT116 WT and SHMT2 KO cells were treated with vehicle or **AGF347** (10 μM) per protocol in section 3.2.9 and oxygen consumption rate (OCR) was monitored throughout a mitochondrial stress test (A – adapted from Agilent Technologies, Inc.) (i.e. at baseline and throughout sequential injections of oligomycin (1 μM), carbonyl cyanide-4-(trifluoromethoxy)phenylhydrazone (FCCP- 1 μM) and rotenone/antimycin A (0.5 μM each)). The results (B) reflect mean ± standard error of at least 10 technical replicates measured over two independent experiments. Significant differences are denoted by # or * with the number of symbols indicating the degree of significance (# denotes p <0.1, * denotes p<0.05, ** denotes p<0.01, *** denotes p<0.001).

leaky expression of SHMT2 through an uninduced tet-inducible vector was sufficient to translate mitochondrial proteins (Minton et al., 2018). ATP suppression in **AGF347-**treated cells is, then, likely secondary to inhibition of upstream purine biosynthesis.While inhibition of mitochondrial respiration required functional KO of SHMT2, another report indicated mere KD of SHMT2 was sufficient to impact cellular antioxidant capacity (Ye et al., 2014). SHMT2 is critical for synthesis of glycine required for generation of GSH as well as synthesis of NADPH required to regenerate GSH from GSSG (Ducker and Rabinowitz, 2017). Indeed, previous work had shown that *de novo* GSH biosynthesis was more sensitive to glycine depletion than either purine or protein biosynthesis (Ducker et al., 2017). GSH functions to scavenge the ROS that are byproducts of oxidative phosphorylation, particularly under hypoxic conditions (such as those found in tumors) which induce an electron leak from the electron transport chain (Chandel et al., 2000; Guzy et al., 2005). We first measured the effects of SHMT2 inhibition by our compounds on ROS levels using the SHMT1 KO, SHMT2 KO, and WT HCT116 cells. WT cells were treated with drugs (10 μM) in glycine-free media (24 hours) supplemented with adenosine (60 μM – to isolate effects of SHMT2 inhibition vis a vis *de novo* purine biosynthesis inhibition) under hypoxia (0.5% oxygen (Ye et al., 2014)) and normoxia (21% oxygen) with measurements of carbonic anhydrase IX as a functional readout of hypoxia (**Figure 3.9 - A**) (Wykoff et al., 2000). Under hypoxia, but not normoxia (**Figures 3.9 C and B, respectively**), ROS levels were 3-fold increased for the SHMT2 KO cells relative to WT. Notably, SHMT2 KO induced a 6-fold larger increase in ROS relative to WT than did SHMT1 KO, establishing SHMT2 as the critical enzyme target for drug-induced ROS production. A similar pattern was seen with drug treatment as only **AGF320** induced a minor increase in ROS under normoxia while all three drugs induced

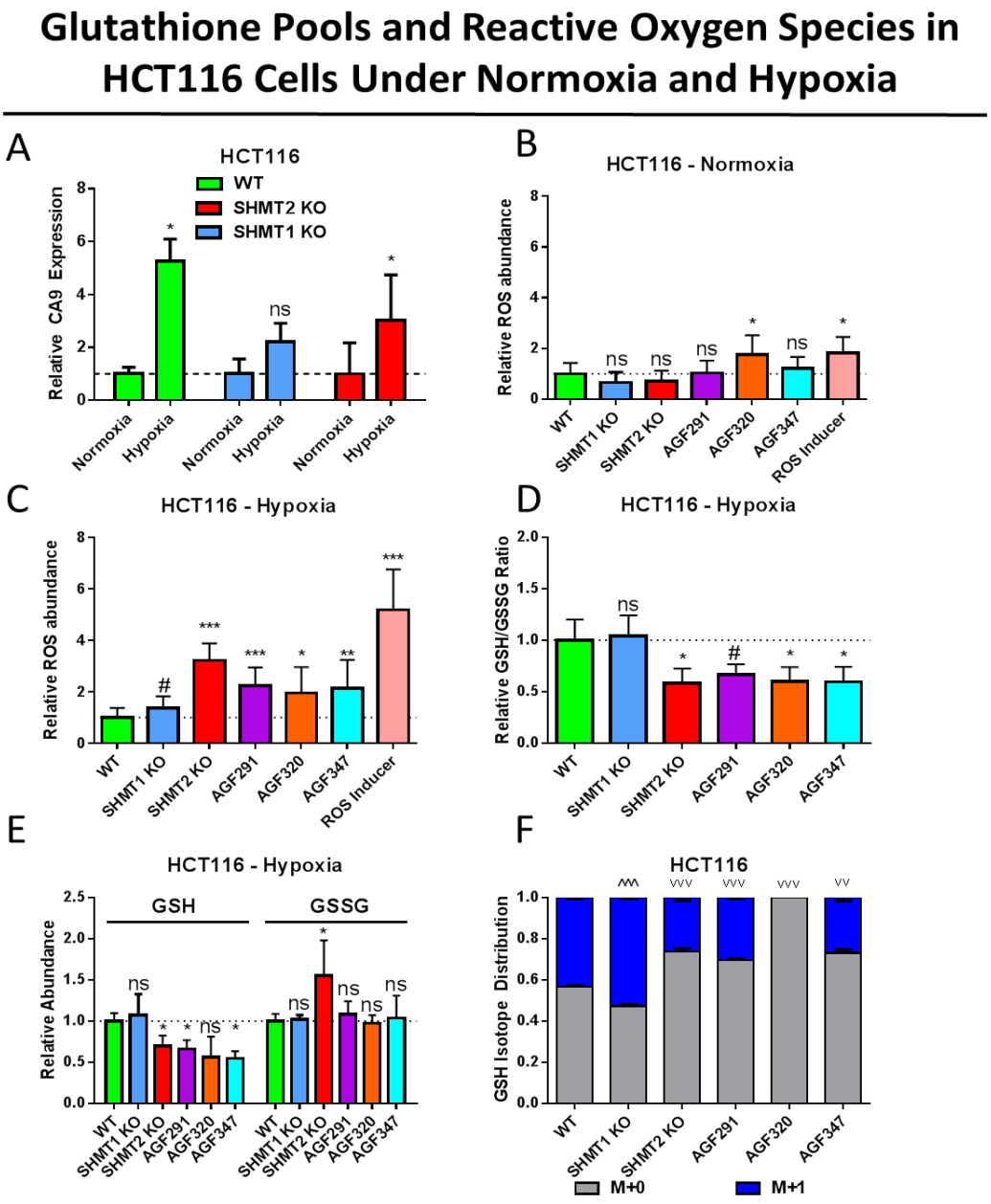

Figure 3.9 Glutathione Pools and ROS in HCT116 Cells. (A). Parallel incubations were conducted under normoxia (21% O_2) and hypoxia (0.5% O_2) with carbonic anhydrase IX (CA9) measured by RT-PCR as a hypoxia marker (Wykoff et al., 2000) (B,C). ROS were quantified under normoxia (B) and hypoxia (C) per protocol in section 3.2.10. (D,E). Reduced (GSH) and oxidized glutathione(GSSG) ((D) – ratio, (E) – individual measurements) were calculated per protocol in section 3.2.10 (F). [2,3,3-^{2}H]-serine flux into GSH was quantified by targeted metabolomics per protocol in section 3.2.11. Significant differences are denoted by # or * with ^ indicating a significant increase or ^{V} indicating a significant decrease and the number of symbols indicating the degree of significance (#^ or #^{V} denotes p <0.1, ^ or ^{V} denotes p<0.05, ^^ or ^{VV} denotes p<0.01, ^^^ or ^{VVV} denotes p<0.001).

a 2-fold increase in ROS under hypoxia, confirming ROS production as a potential mechanism of cytotoxicity in hypoxic tumors.

To assess if suppression of GSH synthesis was the primary cause of the increase in ROS, we assayed GSH and GSSG in the HCT116 cells using a fluorescence assay (o-phthalaldehyde (Senft et al., 2000)). Consistent with the relative changes in ROS, the GSH/GSSG ratio was significantly diminished (~30%) in both SHMT2 KO and drug-treated HCT116 cells, but not in SHMT1 KO cells (**Figure 3.9 - D**). Importantly, SHMT2 KO effected accumulation of GSSG along with depletion of GSH (**Figure 3.9 - E**), suggesting perturbation of GSH/GSSG ratio by both inhibition of GSSG reduction to GSH and suppression of *de novo* GSH biosynthesis, consistent with previous literature (Ducker et al., 2017; Ye et al., 2014). Conversely, the change in GSH/GSSG ratio caused by drug treatment was entirely due to depletion of GSH pools without accumulation of GSSG, suggesting inhibition of *de novo* GSH biosynthesis alone as causal.

To confirm GSH biosynthesis inhibition as the underlying drug-induced mechanism perturbing the GSH/GSSG ratio, we performed targeted metabolomics per protocol in section 2.2.6 (**Figure 3.9 - F**) using a [2,3,3-^{2}H]-serine tracer in cells treated with 10 μM drug for 48 hours to trace the conversion of serine to glycine (by SHMT2) and the subsequent incorporation of glycine into GSH (by GSH synthetase) (Lu, 2013). As expected, SHMT2 KO decreased [2,3,3-^{2}H]-serine flux into GSH by ~40%, decreasing the GSH M+1 (i.e. labeled) fraction from 44% in the WT to 26% and reflecting partial compensation by reversal of SHMT1 (Ducker et al., 2016). SHMT1 KO, however, actually increased the M+1 fraction to 53%, consistent with a compensatory increase in SHMT2 activity in these cells. Notably, treatment with **AGF291**, **AGF320**, and **AGF347** (which inhibit both SHMT1 and SHMT2), had an equal or larger effect

on the M+1 fraction as compared to SHMT2 KO alone, decreasing M+1 labeling to 30%, 0%, and 27%, respectively. These results are consistent with our earlier enzymology studies, which confirmed **AGF320** to be the most potent inhibitor of both SHMT1 and SHMT2 *in vitro*, and establish inhibition of *de novo* GSH biosynthesis as another potential mechanism of *in vivo* cytotoxic activity by these compounds.

3.3.5 *In vivo* Antitumor Efficacy and Pharmacodynamics of AGF347 against MIA PaCa-2 Tumor Xenografts: Late Stage Disease

Because of the unprecedented efficacy of **AGF347** in the early-stage trial against a MIA PaCa-2 xenograft model (as discussed in section 2.2.9), we progressed to a late-stage trial of **AGF347** in the same model where tumors were allowed to grow untreated for 7 days to 100-150 mg before treatment to simulate late-stage disease. As before, starting 14 days before tumor implantation, the mice were maintained on either a folate-deficient diet to ensure that serum folate levels would approximate those of humans, or on a standard folate-replete diet which results in normal mouse serum folates that are ~10-fold higher than those in humans (Golani et al., 2016; Varela-Moreiras and Selhub, 1992; Wang et al., 2010; Wang et al., 2011). The mice were then non-selectively distributed to each group's treatment and control arms (5 mice per group for the folate-deficient diet, 3-4 mice per group for the standard folate-replete diet). **AGF347** (15 mg/kg q2dx8) and gemcitabine (120 mg/kg q4dx4) were, as a whole, comparably efficacious, with a median tumor burden- on day 21 of 733 mg (range 373-1835 mg) and 524 mg (range 247-1045 mg), respectively, compared to 1736 mg (range 1117-2046 mg) for the control cohort. The resulting median T/C values on day 21 were also comparable, 30% for gemcitabine and 42% for **AGF347** (**Figure 3.10 - A**). However, **AGF347**, but not gemcitabine, induced two partial responses (treatment-induced tumor burden nadir < 50% of peak tumor burden after

tumor engraftment (i.e. tumor burden >150 mg)), including one complete response (treatment-induced tumor burden nadir = 0 mg after tumor engraftment). For **AGF347**, the partial responses were strikingly large changes in tumor burden (688 mg to 220 mg and 400 mg to 0 mg) and occurred on day 31 (10 days post last dose), consistent with long-term cellular accumulation of polyglutamyl drug forms (see section 3.3.2). Overall tumor growth delays (median T-C to reach 1000 mg) of 11 days (gemcitabine) compared to 7 days (**AGF347)** were recorded. However, for the partial responses, **AGF347** induced superior tumor growth delay of 26 and 52 days as compared to 16 and 25 days for the best gemcitabine responders. In this test, both drugs were well tolerated, with modest weight loss as the only symptom observed during treatment (**AGF347**: 1% (-0.2 g) median nadir on day 21; full recovery on day 24; and GEM: 5.1%(-1.0 g) median nadir on day 20 with full recovery on day 24). Collectively, these results establish that **AGF347**, even in the setting of late-stage disease, offers significant potential therapeutic benefit over the standard-of-care gemcitabine.

In addition to an efficacy arm, we also included a metabolomics arm to assess the *in vivo* pharmacodynamics of **AGF347**. Tumor samples from a separate cohort of **AGF347**-treated and control mice were harvested six hours after the 6^{th} injection of **AGF347**, when the control mice had achieved a tumor burden that required their euthanasia (i.e. 2000 mg). These tumors were then flash-frozen and analyzed via targeted metabolomics (**Figure 3.10 – B-C**). Consistent with its *in vitro* effects (**Figure 2.7 – C,F**), **AGF347** effected increases in GAR (200- fold), AICAR (500-fold), and serine (1.5-fold), consistent with inhibition of GARFTase, AICARFTase, and SHMT2 respectively. Moreover, **AGF347** effected a 5-fold increase in AMP coupled with a 10-fold decrease in ATP, indicating cytotoxicity and severe perturbation of energy charge and purine biosynthesis (**Figure 3.10 – C**). These results confirm the *in vivo* mechanism of action of

Late-stage Efficacy and Metabolomics Trials with AGF347 against MIA Paca-2 Tumor Xenografts

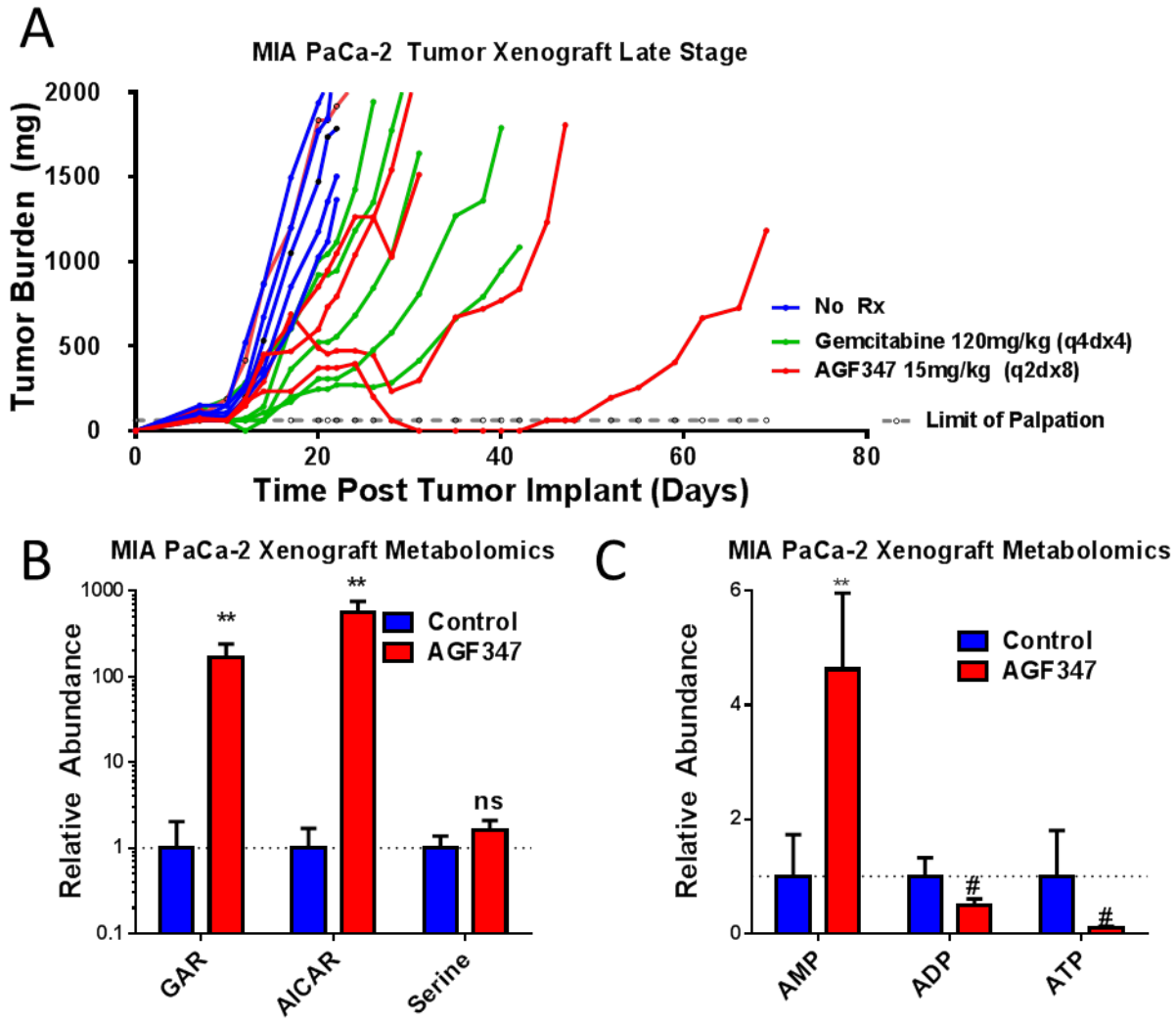

Figure 3.10 ***In vivo*** **Efficacy and Metabolomics Against Late-Stage MIA PaCa-2 Tumor xenografts in SCID Mice. AGF347** was tested head-to-head against gemcitabine against late-stage MIA PaCa-2 tumor xenograft models (A – per protocol in section 3.2.12). Tumor samples from separate treatment and control arms were harvested after 6 doses of **AGF347** and assessed by targeted metabolomics (section 3.2.13) for total GAR, AICAR, serine (B) and adenine nucleotide pools (C). Significant differences are denoted by # or * with the number of symbols indicating the degree of significance (# denotes p <0.1, * denotes p<0.05, ** denotes p<0.01, *** denotes p<0.001).

AGF347 to be inhibition of cytosolic purine biosynthesis at GARFTase and AICARFTase as well as inhibition of mitochondrial C1 metabolism.

3.4 Discussion

In this chapter, we characterized the cellular pharmacodynamics of the 5-substituted pyrrolo[3,2-*d*]pyrimidine compounds, **AGF291**, **AGF320**, and **AGF347**, which we established in Chapter 2 to inhibit mitochondrial C1 metabolism at SHMT2 and cytosolic C1 metabolism at SHMT1 and the purine biosynthetic enzymes GARFTase and AICARFTase.

We established plasma membrane transport profiles in HCT116, H460, and MIA PaCa-2 cells and determined RFC and PCFT transporter kinetics. Although the lead compound **AGF347** had a PCFT affinity comparable to the best known PCFT substrates **AGF94** and **PMX** (Desmoulin et al., 2012a), it along with **AGF291** and **AGF320** maintained a stronger affinity for RFC than **PMX** (**Table 1**). Combined with pH 6.8 uptake of [^{3}H]-**AGF347** predominantly by RFC over PCFT (**Figure 3.3 – B,E,H)**, these results suggest substantial room for improvement in PCFT selectivity, which would increase tumor selectivity overall (Desmoulin et al., 2012a).

We also resolved the cytosolic and mitochondrial compartmentation of **AGF347**, noting near-complete polyglutamylation in both compartments (**Figure 3.5 – A,B**), which likely enables *in vivo* cellular accumulation and delayed, yet potent antitumor activity (**Figure 3.10 - A**). As a significant decrease in mitochondrial accumulation of [^{3}H]-**AGF347** occurs in MFT KO (GlyB vs GlyBTII), but not MFT KD (MIA PaCa-2 MFT KD vs NTC) (**Figure 3.4 - F**), we deduce that even a small amount of MFT is sufficient to fully transport **AGF347** into the mitochondria. Moreover, MFT-inactive cells (GlyB) accumulated more mitochondrial [^{3}H]-**AGF347** than [^{3}H]-**folic acid** (for which MFT is the only known mitochondrial transporter (Lawrence et al., 2011; McCarthy et al., 2004)) while the opposite was true for the MFT-restored cells (GlyBTII)

(**Figure 3.4 - F**). **AGF347**, then, must be transported into mitochondria by an additional transporter besides MFT.

Finally, we investigated several mechanisms of cytotoxicity, including depletion of purines, inhibition of mTOR, impairment of mitochondrial respiration, and inhibition of ROS scavenging. Interestingly, while purine depletion by **AGF347** in MIA PaCa-2 cells *in vitro* was in the order AMP >ADP > ATP (**Figure 3.6 - C**), purine depletion by **AGF347** in MIA PaCa-2 xenografts *in-vivo* was reversed in the order ATP > ADP with AMP actually *increased* (**Figure 3.10 - B**). These differences likely stem from the difference in treatment course as the *in vitro* data reflect a single acute drug treatment for 48 hours whereas the *in vivo* data reflect chronic treatment with drug over 6 q2d doses. The long-course treatment of **AGF347** *in vivo* leads to increased tumor cell death, thus leading to energy depletion as reflected in an increase of the AMP/ATP ratio. As accumulation of GAR, AICAR, and serine remain qualitatively identical *in vitro* (**Figure 2.7 – C,F, Figure 2.5 - C**) and *in vivo* (**Figure 3.10 - A**), we deduce enzyme targets of **AGF347** are identical in both settings.

The pharmacodynamics of **AGF291**, **AGF320**, and **AGF347** described in this chapter expand upon the biological uniqueness and unequivocal antitumor potential of these compounds. While these prototype agents leave significant room for improvement for PCFT-selectivity, their potent efficacy *in vivo* sets an exciting benchmark for further clinical development.

CHAPTER 4- CONCLUSIONS AND FUTURE DIRECTIONS

The goal of this dissertation work was to design and characterize inhibitors of mitochondrial C1 metabolism at SHMT2. In Chapter 2, we designed, synthesized, and confirmed enzyme targets of novel 5-substituted pyrrolo[3,2-*d*]pyrimidine compounds **AGF291**, **AGF320**, and **AGF347**. These multitargeted agents were shown to inhibit SHMT2 in the mitochondria as well as SHMT1, GARFTase, and AICARFTase in the cytosol. In Chapter 3, we assessed the downstream cellular effects of targeting these enzymes on "non-C1" pathways such as ROS scavenging, mitochondrial oxidative phosphorylation, and mTOR signaling. Moreover, we also determined the plasma membrane and mitochondrial membrane transport profiles. Importantly, **AGF291** and **AGF347** were, to our knowledge, the first inhibitors of SHMT2 with *bona fide in vivo* activity as demonstrated against early-stage MIA PaCa-2 tumor xenografts with **AGF347** demonstrating similar efficacy in the late-stage disease setting as well.

These studies provide proof-of-concept that targeting mitochondrial C1 metabolism offers tremendous therapeutic potential against cancer. Moreover, the structure-activity-relationship profile derived from this initial series of drugs establishes the pyrrolo[3,2-*d*]pyrimidine scaffold as superior to the previously described pyrazolopyran SHMT inhibitors that were inactive *in vivo*. In particular, the lead compound of this series, **AGF347**, is a promising candidate for future clinical development and optimization.

Despite the exceptionally positive early returns, further work on these compounds remains to be done. One major area for improvement for these compounds remains selectivity for non-RFC transporters (i.e. PCFT or FR). Although **AGF347** is the most potent of this series *in vivo*, its activity is mediated primarily by RFC (as previously discussed in section 3.3.1) and, perhaps, this RFC-mediated uptake limits the MTD of this drug to merely one-fourth that of

gemcitabine. A next-generation analog of **AGF347** carrying increased selectivity for PCFT or FR would, in theory, allow for increased drug dosing and consequently, improved efficacy. Further basic science work may be conducted on identifying the specific mitochondrial transporter for **AGF347**, which we established in section 3.3.2 is partially, but not completely, transported into mitochondria by MFT. Perhaps this unidentified transporter is another member of the mitochondrial carrier family.

Another area for further study is the characterization of the *in vivo* response to **AGF291** and **AGF347**. In both the early-stage (**Figure 2.9**) and late-stage (**Figure 3.10**) trials of these drugs against MIA PaCa-2 tumor xenografts, individual mouse responses ranged from indistinguishable from those of the vehicle-treated controls to complete response/cure. In contrast, the responses to gemcitabine were largely more uniform. This difference between **AGF347** treatment and gemcitabine treatment was most evident in the late-stage trial where both the most-responsive and least-responsive mice to treatment were **AGF347**-treated. If we could identify a biomarker that would predict response to **AGF347**, we would be able to focus treatment on those 20% of tumors more likely to exhibit complete response.

Beyond this particular series of molecules, which target SHMT2, we may, in the future, generate molecules which inhibit MTHFD2, another mitochondrial C1 metabolism enzyme with substantial promise as a drug target (as previously discussed in section 1.5.1). Notably, the function of MTHFD2 (which is only expressed in tumor and embryonic tissues) in normal tissues is performed by MTHFD2L, which maintains 60-65% sequence identity with MTHFD2 (Shin et al., 2014). Therefore, selective inhibition of MTHFD2 without concomitant inhibition of MTHFD2L would likely confer additional tumor selectivity relative to targeting SHMT2.

While inhibition of C1 metabolism has largely played a central role in the arsenal against cancer since the beginning of chemotherapy, classical inhibitors of C1 metabolism have been pushed to the periphery of the modern day chemotherapeutic toolbox by more targeted therapies such as inhibitors of HER-2, BRAF, and tyrosine kinases. Through targeting of non-classical enzymes such as SHMT2, as well as targeting of non-RFC transporters such as PCFT, we have generated compounds with broad-spectrum antitumor efficacy both *in vitro* and *in vivo*. Although first generation compounds, these agents already offer significant therapeutic promise in the battle against cancer and, with next generation compounds continuously being refined and synthesized, the future for C1 metabolism inhibitors remains bright.

REFERENCES

Abolmaali SS, Tamaddon AM and Dinarvand R (2013) A review of therapeutic challenges and achievements of methotrexate delivery systems for treatment of cancer and rheumatoid arthritis. *Cancer chemotherapy and pharmacology* **71**(5): 1115-1130.

Adjei AA (2004) Pemetrexed (ALIMTA), A Novel Multitargeted Antineoplastic Agent. *Clinical Cancer Research* **10**(12): 4276s-4280s.

Aherne GW, Hardcastle A, Raynaud F and Jackman AL (1996) Immunoreactive dUMP and TTP pools as an index of thymidylate synthase inhibition; effect of tomudex (ZD1694) and a nonpolyglutamated quinazoline antifolate (CB30900) in L1210 mouse leukaemia cells. *Biochemical Pharmacology* **51**(10): 1293-1301.

Alati T, Worzalla JF, Shih C, Bewley JR, Lewis S, Moran RG and Grindey GB (1996) Augmentation of the Therapeutic Activity of Lometrexol [-(6-R)5,10-Dideazatetrahydrofolate] by Oral Folic Acid. *Cancer Research* **56**(10): 2331-2335.

Allaire M, Li Y, MacKenzie RE and Cygler M (1998) The 3-D structure of a folate-dependent dehydrogenase/cyclohydrolase bifunctional enzyme at 1.5 A resolution. *Structure (London, England : 1993)* **6**(2): 173-182.

Amelio I, Cutruzzolá F, Antonov A, Agostini M and Melino G (2014) Serine and glycine metabolism in cancer. *Trends in Biochemical Sciences* **39**(4): 191-198.

Anderson DD, Quintero CM and Stover PJ (2011) Identification of a de novo thymidylate biosynthesis pathway in mammalian mitochondria. *Proceedings of the National Academy of Sciences* **108**(37): 15163-15168.

Anderson DD, Woeller CF, Chiang EP, Shane B and Stover PJ (2012) Serine hydroxymethyltransferase anchors de novo thymidylate synthesis pathway to nuclear lamina for DNA synthesis. *Journal of Biological Chemistry* **287**(10): 7051-7062.

Appling DR (1991) Compartmentation of folate-mediated one-carbon metabolism in eukaryotes. *FASEB Journal* **5**(12): 2645-2651.

Assaraf YG, Leamon CP and Reddy JA (2014) The folate receptor as a rational therapeutic target for personalized cancer treatment. *Drug Resistance Update* **17**(4-6): 89-95.

Badar T, Patel KP, Thompson PA, DiNardo C, Takahashi K, Cabrero M, Borthakur G, Cortes J, Konopleva M, Kadia T, Bohannan Z, Pierce S, Jabbour EJ, Ravandi F, Daver N, Luthra R, Kantarjian H and Garcia-Manero G (2015) Detectable FLT3-ITD or RAS mutation at the time of transformation from MDS to AML predicts for very poor outcomes. *Leukemia research* **39**(12): 1367-1374.

Banerji U, Garces AHI, Michalarea V, Ruddle R, Raynaud FI, Riisnaes R, Rodrigues DN, Tunariu N, Porter JC, Ward SE, Parmar M, Turner AJ, Seeramreddi S, Hall E, Dean EJ, Basu B, George A, Kaye SB, Banerjee SN and Bono JSD (2017) An investigator-initiated phase I study of ONX-0801, a first-in-class alpha folate receptor targeted, small molecule thymidylate synthase inhibitor in solid tumors. *Journal of Clinical Oncology* **35**(15_suppl): 2503-2503.

Beardsley GP, Moroson BA, Taylor EC and Moran RG (1989) A new folate antimetabolite, 5,10-dideaza-5,6,7,8-tetrahydrofolate is a potent inhibitor of de novo purine synthesis. *Journal of Biological Chemistry* **264**(1): 328-333.

Ben-Sahra I, Hoxhaj G, Ricoult SJH, Asara JM and Manning BD (2016) mTORC1 induces purine synthesis through control of the mitochondrial tetrahydrofolate cycle. *Science (New York, NY)* **351**(6274): 728-733.

Beroukhim R, Mermel CH, Porter D, Wei G, Raychaudhuri S, Donovan J, Barretina J, Boehm JS, Dobson J, Urashima M, Mc Henry KT, Pinchback RM, Ligon AH, Cho YJ, Haery L, Greulich H, Reich M, Winckler W, Lawrence MS, Weir BA, Tanaka KE, Chiang DY, Bass AJ, Loo A, Hoffman C, Prensner J, Liefeld T, Gao Q, Yecies D, Signoretti S, Maher E, Kaye FJ, Sasaki H, Tepper JE, Fletcher JA, Tabernero J, Baselga J, Tsao MS, Demichelis F, Rubin MA, Janne PA, Daly MJ, Nucera C, Levine RL, Ebert BL, Gabriel S, Rustgi AK, Antonescu CR, Ladanyi M, Letai A, Garraway LA, Loda M, Beer DG, True LD, Okamoto A, Pomeroy SL, Singer S, Golub TR, Lander ES, Getz G, Sellers WR and Meyerson M (2010) The landscape of somatic copy-number alteration across human cancers. *Nature* **463**(7283): 899-905.

Bertino JR, Waud WR, Parker WB and Lubin M (2011) Targeting tumors that lack methylthioadenosine phosphorylase (MTAP) activity Current strategies. *Cancer Biology & Therapy* **11**(7): 627-632.

Brand MD and Nicholls DG (2011) Assessing mitochondrial dysfunction in cells. *Biochem J* **435**(2): 297-312.

Bronder JL and Moran RG (2002) Antifolates targeting purine synthesis allow entry of tumor cells into S phase regardless of p53 function. *Cancer Research* **62**(18): 5236-5241.

Bulock KG, Beardsley GP and Anderson KS (2002) The kinetic mechanism of the human bifunctional enzyme ATIC (5-amino-4-imidazolecarboxamide ribonucleotide

transformylase/inosine 5'-monophosphate cyclohydrolase). A surprising lack of substrate channeling. *Journal of Biological Chemistry* **277**(25): 22168-22174.

Calvert AH, Alison DL, Harland SJ, Robinson BA, Jackman AL, Jones TR, Newell DR, Siddik ZH, Wiltshaw E, McElwain TJ and et al. (1986) A phase I evaluation of the quinazoline antifolate thymidylate synthase inhibitor, N10-propargyl-5,8-dideazafolic acid, CB3717. *Journal of Clinical Oncology* **4**(8): 1245-1252.

Chandel NS, McClintock DS, Feliciano CE, Wood TM, Melendez JA, Rodriguez AM and Schumacker PT (2000) Reactive oxygen species generated at mitochondrial complex III stabilize hypoxia-inducible factor-1alpha during hypoxia: a mechanism of O2 sensing. *Journal of Biological Chemistry* **275**(33): 25130-25138.

Chattopadhyay S, Moran RG and Goldman ID (2007) Pemetrexed: biochemical and cellular pharmacology, mechanisms, and clinical applications. *Molecular cancer therapeutics* **6**(2): 404-417.

Chattopadhyay S, Wang Y, Zhao R and Goldman ID (2004) Lack of Impact of the Loss of Constitutive Folate Receptor {alpha} Expression, Achieved by RNA Interference, on the Activity of the New Generation Antifolate Pemetrexed in HeLa Cells. *Clinical Cancer Research* **10**(23): 7986-7993.

Chattopadhyay S, Zhao R, Krupenko SA, Krupenko N and Goldman ID (2006) The inverse relationship between reduced folate carrier function and pemetrexed activity in a human colon cancer cell line. *Molecular cancer therapeutics* **5**(2): 438-449.

Cherian C, Desmoulin SK, Wang L, Polin L, White K, Kushner J, Stout M, Hou Z, Gangjee A and Matherly LH (2013) Therapeutic targeting malignant mesothelioma with a novel 6-substituted pyrrolo[2,3-D]pyrimidine thienoyl antifolate via its selective uptake by the

proton-coupled folate transporter. *Cancer chemotherapy and pharmacology* **71**(4): 999-1011.

Cheung A, Bax HJ, Josephs DH, Ilieva KM, Pellizzari G, Opzoomer J, Bloomfield J, Fittall M, Grigoriadis A, Figini M, Canevari S, Spicer JF, Tutt AN and Karagiannis SN (2016) Targeting folate receptor alpha for cancer treatment. *Oncotarget* **7**(32): 52553-52574.

Chu E, Callender MA, Farrell MP and Schmitz JC (2003) Thymidylate synthase inhibitors as anticancer agents: from bench to bedside. *Cancer chemotherapy and pharmacology* **52**(1): 80-89.

Ciuleanu T, Brodowicz T, Zielinski C, Kim JH, Krzakowski M, Laack E, Wu YL, Bover I, Begbie S, Tzekova V, Cucevic B, Pereira JR, Yang SH, Madhavan J, Sugarman KP, Peterson P, John WJ, Krejcy K and Belani CP (2009) Maintenance pemetrexed plus best supportive care versus placebo plus best supportive care for non-small-cell lung cancer: a randomised, double-blind, phase 3 study. *Lancet (London, England)* **374**(9699): 1432-1440.

Clasquin MF, Melamud E and Rabinowitz JD (2012) LC-MS data processing with MAVEN: a metabolomic analysis and visualization engine. *Current protocols in bioinformatics* **14**(37): 14.11.11-14.11.23.

Clayton DA and Shadel GS (2014) Isolation of mitochondria from tissue culture cells. *Cold Spring Harbor protocols* **2014**(10): pdb.prot080002.

Cohen MH, Justice R and Pazdur R (2009) Approval summary: pemetrexed in the initial treatment of advanced/metastatic non-small cell lung cancer. *Oncologist* **14**(9): 930-935.

Cunningham D, Zalcberg JR, Rath U, Oliver I, van Cutsem E, Svensson C, Seitz JF, Harper P, Kerr D and Perez-Manga G (1996) Final results of a randomised trial comparing

'Tomudex' (raltitrexed) with 5-fluorouracil plus leucovorin in advanced colorectal cancer. "Tomudex" Colorectal Cancer Study Group. *Annals of Oncology* **7**(9): 961-965.

Deis SM, Doshi A, Hou Z, Matherly LH, Gangjee A and Dann CE, 3rd (2016) Structural and Enzymatic Analysis of Tumor-Targeted Antifolates That Inhibit Glycinamide Ribonucleotide Formyltransferase. *Biochemistry* **55**(32): 4574-4582.

Deng Y, Wang Y, Cherian C, Hou Z, Buck SA, Matherly LH and Gangjee A (2008) Synthesis and Discovery of High Affinity Folate Receptor-Specific Glycinamide Ribonucleotide Formyltransferase Inhibitors With Antitumor Activity. *Journal of Medicinal Chemistry* **51**(16): 5052-5063.

Deng Y, Zhou X, Desmoulin SK, Wu J, Cherian C, Hou Z, Matherly LH and Gangjee A (2009) Synthesis and biological activity of a novel series of 6-substituted thieno[2,3-d]pyrimidine antifolate inhibitors of purine biosynthesis with selectivity for high affinity folate receptors over the reduced folate carrier and proton-coupled folate transporter for cellular entry. *Journal of Medicinal Chemistry* **52**(9): 2940-2951.

Desmoulin SK, Hou Z, Gangjee A and Matherly LH (2012a) The human proton-coupled folate transporter: Biology and therapeutic applications to cancer. *Cancer Biology & Therapy* **13**(14): 1355-1373.

Desmoulin SK, Wang L, Polin L, White K, Kushner J, Stout M, Hou Z, Cherian C, Gangjee A and Matherly LH (2012b) Functional Loss of the Reduced Folate Carrier Enhances the Antitumor Activities of Novel Antifolates with Selective Uptake by the Proton-Coupled Folate Transporter. *Molecular Pharmacology* **82**(4): 591-600.

Ducker GS, Chen L, Morscher RJ, Ghergurovich JM, Esposito M, Teng X, Kang Y and Rabinowitz JD (2016) Reversal of Cytosolic One-Carbon Flux Compensates for Loss of the Mitochondrial Folate Pathway. *Cell Metabolism* **23**(6): 1140-1153.

Ducker GS, Ghergurovich JM, Mainolfi N, Suri V, Jeong SK, Hsin-Jung Li S, Friedman A, Manfredi MG, Gitai Z, Kim H and Rabinowitz JD (2017) Human SHMT inhibitors reveal defective glycine import as a targetable metabolic vulnerability of diffuse large B-cell lymphoma. *Proceedings of the National Academy of Sciences* **114**(43): 11404-11409.

Ducker GS and Rabinowitz JD (2017) One-Carbon Metabolism in Health and Disease. *Cell Metabolism* **25**(1): 27-42.

Eadsforth TC, Gardiner M, Maluf FV, McElroy S, James D, Frearson J, Gray D and Hunter WN (2012) Assessment of Pseudomonas aeruginosa N5,N10-methylenetetrahydrofolate dehydrogenase-cyclohydrolase as a potential antibacterial drug target. *PLoS ONE* **7**(4): e35973.

Elnakat H and Ratnam M (2004) Distribution, functionality and gene regulation of folate receptor isoforms: implications in targeted therapy. *Advanced drug delivery reviews* **56**(8): 1067-1084.

Eruslanov E and Kusmartsev S (2010) Identification of ROS Using Oxidized DCFDA and Flow-Cytometry, in *Advanced Protocols in Oxidative Stress II* (Armstrong D ed) pp 57-72, Humana Press, Totowa, NJ.

Esteban E, Casillas M and Cassinello A (2009) Pemetrexed in first-line treatment of non-small cell lung cancer. *Cancer treatment reviews* **35**(4): 364-373.

Fabre I, Fabre G and Goldman ID (1984) Polyglutamylation, an Important Element in Methotrexate Cytotoxicity and Selectivity in Tumor versus Murine Granulocytic Progenitor Cells in Vitro. *Cancer Research* **44**(8): 3190-3195.

Fan J, Kamphorst JJ, Mathew R, Chung MK, White E, Shlomi T and Rabinowitz JD (2013) Glutamine-driven oxidative phosphorylation is a major ATP source in transformed mammalian cells in both normoxia and hypoxia. *Molecular systems biology* **9**: 712.

Fan J, Ye J, Kamphorst JJ, Shlomi T, Thompson CB and Rabinowitz JD (2014) Quantitative flux analysis reveals folate-dependent NADPH production. *Nature* **510**(7504): 298-302.

Farber S, Cutler EC, Hawkins JW, Harrison JH, Peirce EC, 2nd and Lenz GG (1947) The Action of Pteroylglutamic Conjugates on Man. *Science (New York, NY)* **106**(2764): 619-621.

Farber S and Diamond LK (1948) Temporary remissions in acute leukemia in children produced by folic acid antagonist, 4-aminopteroyl-glutamic acid. *New England Journal of Medicine* **238**(23): 787-793.

Field MS, Kamynina E, Chon J and Stover PJ (2018) Nuclear Folate Metabolism. *Annu Rev Nutr* **38**(1): 219-243.

Field MS, Kamynina E and Stover PJ (2016) MTHFD1 regulates nuclear de novo thymidylate biosynthesis and genome stability. *Biochimie* **126**: 27-30.

Flintoff WF, Davidson SV and Siminovitch L (1976) Isolation and partial characterization of three methotrexate-resistant phenotypes from Chinese hamster ovary cells. *Somatic Cell and Molecular Genetics* **2**(3): 245-261.

Foss FM, Parker TL, Girardi M and Li A (2018) Clinical Activity of Pralatrexate in Patients With Cutaneous T-Cell Lymphoma Treated With Varying Doses of Pralatrexate. *Clinical lymphoma, myeloma & leukemia* **18**(11): e445-e447.

Fu C, Sikandar A, Donner J, Zaburannyi N, Herrmann J, Reck M, Wagner-Döbler I, Koehnke J and Müller R (2017) The natural product carolacton inhibits folate-dependent C1 metabolism by targeting FolD/MTHFD. *Nature communications* **8**: 1529.

Fu TF, Scarsdale JN, Kazanina G, Schirch V and Wright HT (2003) Location of the pteroylpolyglutamate-binding site on rabbit cytosolic serine hydroxymethyltransferase. *Journal of Biological Chemistry* **278**(4): 2645-2653.

Gazzali AM, Lobry M, Colombeau L, Acherar S, Azaïs H, Mordon S, Arnoux P, Baros F, Vanderesse R and Frochot C (2016) Stability of folic acid under several parameters. *European Journal of Pharmaceutical Sciences* **93**: 419-430.

Giardina G, Paone A, Tramonti A, Lucchi R, Marani M, Magnifico MC, Bouzidi A, Pontecorvi V, Guiducci G, Zamparelli C, Rinaldo S, Paiardini A, Contestabile R and Cutruzzola F (2018) The catalytic activity of serine hydroxymethyltransferase is essential for de novo nuclear dTMP synthesis in lung cancer cells. *FEBS Journal* **285**(17): 3238-3253.

Gibbs DD, Theti DS, Wood N, Green M, Raynaud F, Valenti M, Forster MD, Mitchell F, Bavetsias V, Henderson E and Jackman AL (2005) BGC 945, a novel tumor-selective thymidylate synthase inhibitor targeted to alpha-folate receptor-overexpressing tumors. *Cancer Research* **65**(24): 11721-11728.

Gibson DG, Young L, Chuang RY, Venter JC, Hutchison CA, 3rd and Smith HO (2009) Enzymatic assembly of DNA molecules up to several hundred kilobases. *Nature Methods* **6**(5): 343-345.

Girgis S, Nasrallah IM, Suh JR, Oppenheim E, Zanetti KA, Mastri MG and Stover PJ (1998) Molecular cloning, characterization and alternative splicing of the human cytoplasmic serine hydroxymethyltransferase gene. *Gene* **210**(2): 315-324.

Golani LK, Wallace-Povirk A, Deis SM, Wong JE, Ke J, Gu X, Raghavan S, Wilson MR, Li X, Polin L, de Waal PW, White K, Kushner J, O'Connor C, Hou Z, Xu HE, Melcher K, Dann CE, Matherly LH and Gangjee A (2016) Tumor Targeting with Novel 6-Substituted Pyrrolo [2,3-d] Pyrimidine Antifolates with Heteroatom Bridge Substitutions Via Cellular Uptake by Folate Receptor α and the Proton-coupled Folate Transporter and Inhibition of De Novo Purine Nucleotide Biosynthesis. *Journal of Medicinal Chemistry* **59**(17): 7856-7876.

Goldman ID and Zhao R (2002) Molecular, biochemical, and cellular pharmacology of pemetrexed, in *Seminars in Oncology* pp 3-17, Elsevier.

Gustafsson R, Jemth A-S, Gustafsson NMS, Färnegårdh K, Loseva O, Wiita E, Bonagas N, Dahllund L, Llona-Minguez S, Häggblad M, Henriksson M, Andersson Y, Homan E, Helleday T and Stenmark P (2017) Crystal Structure of the Emerging Cancer Target MTHFD2 in Complex with a Substrate-Based Inhibitor. *Cancer Research* **77**(4): 937-948.

Guzy RD, Hoyos B, Robin E, Chen H, Liu L, Mansfield KD, Simon MC, Hammerling U and Schumacker PT (2005) Mitochondrial complex III is required for hypoxia-induced ROS production and cellular oxygen sensing. *Cell Metabolism* **1**(6): 401-408.

Hanauske A-R, Chen V, Paoletti P and Niyikiza C (2001) Pemetrexed Disodium: A Novel Antifolate Clinically Active Against Multiple Solid Tumors. *Oncologist* **6**(4): 363-373.

Hansen HH, Selawry OS, Holland JF and McCall CB (1971) The variability of individual tolerance to methotrexate in cancer patients. *British Journal of Cancer* **25**(2): 298-305.

Henderson GB and Zevely EM (1983) Use of non-physiological buffer systems in the analysis of methotrexate transport in L1210 cells. *International journal of Biochemistry* **6**(4): 507-515.

Heytler PG and Prichard WW (1962) A new class of uncoupling agents — Carbonyl cyanide phenylhydrazones. *Biochemical and biophysical research communications* **7**(4): 272-275.

Hitchings GH and Elion GB (1954) THE CHEMISTRY AND BIOCHEMISTRY OF PURINE ANALOGS. *Annals of the New York Academy of Sciences* **60**(2): 195-199.

Horsman MR and Overgaard J (2016) The impact of hypoxia and its modification of the outcome of radiotherapy. *Journal of radiation research* **57 Suppl 1**: i90-i98.

Hou Z, Gattoc L, O'Connor C, Yang S, Wallace-Povirk A, George C, Orr S, Polin L, White K, Kushner J, Morris RT, Gangjee A and Matherly LH (2017) Dual targeting of epithelial ovarian cancer via folate receptor alpha and the proton-coupled folate transporter with 6-substituted pyrrolo[2,3-d]pyrimidine antifolates. *Molecular cancer therapeutics* **16**(5): 819-830.

Hou Z and Matherly LH (2014) Biology of the Major Facilitative Folate Transporters SLC19A1 and SLC46A1. *Current topics in membranes* **73**: 175-204.

Howard SC, McCormick J, Pui CH, Buddington RK and Harvey RD (2016) Preventing and Managing Toxicities of High-Dose Methotrexate. *Oncologist* **21**(12): 1471-1482.

Hoxhaj G, Hughes-Hallett J, Timson RC, Ilagan E, Yuan M, Asara JM, Ben-Sahra I and Manning BD (2017) The mTORC1 Signaling Network Senses Changes in Cellular Purine Nucleotide Levels. *Cell Reports* **21**(5): 1331-1346.

Jackman AL and Calvert AH (1995) Folate-based thymidylate synthase inhibitors as anticancer drugs. *Annals of Oncology* **6**(9): 871-881.

Jackson RC, Hart LI and Harrap KR (1976) Intrinsic resistance to methotrexate of cultured mammalian cells in relation to the inhibition kinetics of their dihydrololate reductases. *Cancer Research* **36**(6): 1991-1997.

Jackson RC, Jackman AL and Calvert AH (1983) Biochemical effects of a quinazoline inhibitor of thymidylate synthetase, N-(4-(N-((2-amino-4-hydroxy-6-quinazolinyl)methyl)prop-2-ynylamino) benzoyl)-L-glutamic acid (CB3717), on human lymphoblastoid cells. *Biochemical Pharmacology* **32**(24): 3783-3790.

Jaffe N (2009) Osteosarcoma: review of the past, impact on the future. The American experience. *Cancer Treatment Research* **152**: 239-262.

Jägerstad M and Jastrebova J (2013) Occurrence, Stability, and Determination of Formyl Folates in Foods. *Journal of Agricultural and Food Chemistry* **61**(41): 9758-9768.

Jain M, Nilsson R, Sharma S, Madhusudhan N, Kitami T, Souza AL, Kafri R, Kirschner MW, Clish CB and Mootha VK (2012) Metabolite Profiling Identifies a Key Role for Glycine in Rapid Cancer Cell Proliferation. *Science (New York, NY)* **336**(6084): 1040-1044.

Jastroch M, Divakaruni AS, Mookerjee S, Treberg JR and Brand MD (2010) Mitochondrial proton and electron leaks. *Essays in biochemistry* **47**: 53-67.

Kamen BA and Smith AK (2004) A review of folate receptor alpha cycling and 5-methyltetrahydrofolate accumulation with an emphasis on cell models in vitro. *Advanced drug delivery reviews* **56**(8): 1085-1097.

Kim D, Fiske BP, Birsoy K, Freinkman E, Kami K, Possemato R, Chudnovsky Y, Pacold ME, Chen WW, Cantor JR, Shelton LM, Gui DY, Kwon M, Ramkissoon SH, Ligon KL, Kang SW, Snuderl M, Heiden MGV and Sabatini DM (2015) SHMT2 drives glioma cell

survival in the tumor microenvironment but imposes a dependence on glycine clearance. *Nature* **520**(7547): 363-367.

Kim H, Esser L, Hossain MB, Xia D, Yu C-A, Rizo J, van der Helm D and Deisenhofer J (1999) Structure of Antimycin A1, a Specific Electron Transfer Inhibitor of Ubiquinol−Cytochrome c Oxidoreductase. *Journal of the American Chemical Society* **121**(20): 4902-4903.

Koufaris C, Gallage S, Yang T, Lau CH, Valbuena GN and Keun HC (2016) Suppression of MTHFD2 in MCF-7 Breast Cancer Cells Increases Glycolysis, Dependency on Exogenous Glycine, and Sensitivity to Folate Depletion. *Journal of proteome research* **15**(8): 2618-2625.

Krieger R (2010) *Hayes' Handbook of Pesticide Toxicology*. Elsevier Science.

Kuan J and Saier MH (1993) The Mitochondrial Carrier Family of Transport Proteins: Structural, Functional, and Evolutionary Relationships. *Critical Reviews in Biochemistry and Molecular Biology* **28**(3): 209-233.

Kugel Desmoulin S, Wang L, Hales E, Polin L, White K, Kushner J, Stout M, Hou Z, Cherian C, Gangjee A and Matherly LH (2011) Therapeutic Targeting of a Novel 6-Substituted Pyrrolo [2,3-d]pyrimidine Thienoyl Antifolate to Human Solid Tumors Based on Selective Uptake by the Proton-Coupled Folate Transporter. *Molecular Pharmacology* **80**(6): 1096-1107.

Kunze B, Reck M, Dotsch A, Lemme A, Schummer D, Irschik H, Steinmetz H and Wagner-Dobler I (2010) Damage of Streptococcus mutans biofilms by carolacton, a secondary metabolite from the myxobacterium Sorangium cellulosum. *BMC microbiology* **10**: 199.

Labuschagne CF, van den Broek NJ, Mackay GM, Vousden KH and Maddocks OD (2014) Serine, but not glycine, supports one-carbon metabolism and proliferation of cancer cells. *Cell Reports* **7**(4): 1248-1258.

Laemmli UK (1970) Cleavage of structural proteins during the assembly of the head of bacteriophage T4. *Nature* **227**(5259): 680-685.

Laposata M (2019) Clinical Laboratory Reference Values, in *Laposata's Laboratory Medicine: Diagnosis of Disease in the Clinical Laboratory, 3e*, McGraw-Hill Education, New York, NY.

Lawrence SA, Hackett JC and Moran RG (2011) Tetrahydrofolate Recognition by the Mitochondrial Folate Transporter. *Journal of Biological Chemistry* **286**(36): 31480-31489.

Lawrence SA, Titus SA, Ferguson J, Heineman AL, Taylor SM and Moran RG (2014) Mammalian mitochondrial and cytosolic folylpolyglutamate synthetase maintain the subcellular compartmentalization of folates. *Journal of Biological Chemistry* **289**(42): 29386-29396.

Lehtinen L, Ketola K, Makela R, Mpindi JP, Viitala M, Kallioniemi O and Iljin K (2013) High-throughput RNAi screening for novel modulators of vimentin expression identifies MTHFD2 as a regulator of breast cancer cell migration and invasion. *Oncotarget* **4**(1): 48-63.

Levin BL and Varga E (2016) MTHFR: Addressing Genetic Counseling Dilemmas Using Evidence-Based Literature. *Journal of genetic counseling* **25**(5): 901-911.

Liang S-Q, Bührer ED, Berezowska S, Marti TM, Xu D, Froment L, Yang H, Hall SRR, Vassella E, Yang Z, Kocher GJ, Amrein MA, Riether C, Ochsenbein AF, Schmid RA and

Peng R-W (2018) mTOR mediates a mechanism of resistance to chemotherapy and defines a rational combination strategy to treat KRAS-mutant lung cancer. *Oncogene* **38**(5): 622-636.

Lin BF, Huang RF and Shane B (1993) Regulation of folate and one-carbon metabolism in mammalian cells. III. Role of mitochondrial folylpoly-gamma-glutamate synthetase. *Journal of Biological Chemistry* **268**(29): 21674-21679.

Liu F, Liu Y, He C, Tao L, He X, Song H and Zhang G (2014) Increased MTHFD2 expression is associated with poor prognosis in breast cancer. *Tumour Biology* **35**(9): 8685-8690.

Locasale JW (2013) Serine, glycine and the one-carbon cycle: cancer metabolism in full circle. *Nature Reviews Cancer* **13**(8): 572-583.

Locasale JW, Grassian AR, Melman T, Lyssiotis CA, Mattaini KR, Bass AJ, Heffron G, Metallo CM, Muranen T, Sharfi H, Sasaki AT, Anastasiou D, Mullarky E, Vokes NI, Sasaki M, Beroukhim R, Stephanopoulos G, Ligon AH, Meyerson M, Richardson AL, Chin L, Wagner G, Asara JM, Brugge JS, Cantley LC and Vander Heiden MG (2011) Phosphoglycerate dehydrogenase diverts glycolytic flux and contributes to oncogenesis. *Nature genetics* **43**(9): 869-874.

Longley DB, Harkin DP and Johnston PG (2003) 5-Fluorouracil: mechanisms of action and clinical strategies. *Nature Reviews Cancer* **3**: 330-338.

Longo GSA, Gorlick R, Tong WP, Ercikan E and Bertino JR (1997) Disparate Affinities of Antifolates for Folylpolyglutamate Synthetase From Human Leukemia Cells. *Blood* **90**(3): 1241-1245.

Low PS and Antony AC (2004) Folate receptor-targeted drugs for cancer and inflammatory diseases. *Advanced drug delivery reviews* **56**(8): 1055-1058.

Lowry OH, Rosebrough NJ, Farr AL and Randall RJ (1951) Protein measurement with the Folin phenol reagent. *Journal of Biological Chemistry* **193**(1): 265-275.

Lu SC (2013) Glutathione synthesis. *Biochimica Et Biophysica Acta* **1830**(5): 3143-3153.

Lu W, Clasquin MF, Melamud E, Amador-Noguez D, Caudy AA and Rabinowitz JD (2010) Metabolomic analysis via reversed-phase ion-pairing liquid chromatography coupled to a stand alone orbitrap mass spectrometer. *Analytical chemistry* **82**(8): 3212-3221.

Lucas S, Chen G, Aras S and Wang J (2018) Serine catabolism is essential to maintain mitochondrial respiration in mammalian cells. *Life Science Alliance* **1**(2): e201800036.

Ma EH, Bantug G, Griss T, Condotta S, Johnson RM, Samborska B, Mainolfi N, Suri V, Guak H, Balmer ML, Verway MJ, Raissi TC, Tsui H, Boukhaled G, Henriques da Costa S, Frezza C, Krawczyk CM, Friedman A, Manfredi M, Richer MJ, Hess C and Jones RG (2017) Serine Is an Essential Metabolite for Effector T Cell Expansion. *Cell Metabolism* **25**(2): 345-357.

Mager DR (2015) Methotrexate. *Home healthcare now* **33**(3): 139-141.

Mann KM, Ying H, Juan J, Jenkins NA and Copeland NG (2016) KRAS-related proteins in pancreatic cancer. *Pharmacology & therapeutics* **168**: 29-42.

Marani M, Paone A, Fiascarelli A, Macone A, Gargano M, Rinaldo S, Giardina G, Pontecorvi V, Koes D, McDermott L, Yang T, Paiardini A, Contestabile R and Cutruzzola F (2016) A pyrazolopyran derivative preferentially inhibits the activity of human cytosolic serine hydroxymethyltransferase and induces cell death in lung cancer cells. *Oncotarget* **7**(4): 4570-4583.

Martiniak Y, Heuer T and Hoffmann I (2015) Intake of dietary folate and folic acid in Germany based on different scenarios for food fortification with folic acid. *European Journal of Nutrition* **54**(7): 1045-1054.

Masaya N, Takashi I, Shinichi A, Youichi H, Hiroshi M, Rika S and Kuniaki T (1995) Synthetic Studies on Oligomycins. Synthesis of the Oligomycin B Spiroketal and Polypropionate Portions. *Bulletin of the Chemical Society of Japan* **68**(3): 967-989.

Matherly LH, Hou Z and Deng Y (2007) Human reduced folate carrier: translation of basic biology to cancer etiology and therapy. *Cancer metastasis reviews* **26**(1): 111-128.

Matherly LH, Voss MK, Anderson LA, Fry DW and Goldman ID (1985) Enhanced polyglutamylation of aminopterin relative to methotrexate in the Ehrlich ascites tumor cell in vitro. *Cancer Research* **45**(3): 1073-1078.

Matherly LH, Wilson MR and Hou Z (2014) The Major Facilitative Folate Transporters Solute Carrier 19A1 and Solute Carrier 46A1: Biology and Role in Antifolate Chemotherapy of Cancer. *Drug Metabolism & Disposition* **42**(4): 632-649.

Matloub Y, Bostrom BC, Hunger SP, Stork LC, Angiolillo A, Sather H, La M, Gastier-Foster JM, Heerema NA, Sailer S, Buckley PJ, Thomson B, Cole C, Nachman JB, Reaman G, Winick N, Carroll WL, Devidas M and Gaynon PS (2011) Escalating intravenous methotrexate improves event-free survival in children with standard-risk acute lymphoblastic leukemia: a report from the Children's Oncology Group. *Blood* **118**(2): 243-251.

Matsudaira P (1987) Sequence from picomole quantities of proteins electroblotted onto polyvinylidene difluoride membranes. *Journal of Biological Chemistry* **262**(21): 10035-10038.

Mazurek S (2011) Pyruvate kinase type M2: A key regulator of the metabolic budget system in tumor cells. *The International Journal of Biochemistry & Cell Biology* **43**(7): 969-980.

McCarthy EA, Titus SA, Taylor SM, Jackson-Cook C and Moran RG (2004) A mutation inactivating the mitochondrial inner membrane folate transporter creates a glycine requirement for survival of chinese hamster cells. *Journal of Biological Chemistry* **279**(32): 33829-33836.

Mean Son J, Sarsour E, Kakkerla Balaraju A, Fussell J, L. Kalen A, Wagner B, Buettner G and C. Goswami P (2017) Mitofusin 1 and optic atrophy 1 shift metabolism to mitochondrial respiration during aging. *Aging Cell* **16**(5): 1136-1145.

Miller AL (2003) The methionine-homocysteine cycle and its effects on cognitive diseases. *Alternative Medicine Review* **8**(1): 7-19.

Mills JL and Dimopoulos A (2015) Folic acid fortification for Europe? *BMJ* **351**: h6198.

Minton DR, Nam M, McLaughlin DJ, Shin J, Bayraktar EC, Alvarez SW, Sviderskiy VO, Papagiannakopoulos T, Sabatini DM, Birsoy K and Possemato R (2018) Serine Catabolism by SHMT2 Is Required for Proper Mitochondrial Translation Initiation and Maintenance of Formylmethionyl-tRNAs. *Molecular Cell* **69**(4): 610-621.e615.

Mitchell-Ryan S, Wang Y, Raghavan S, Ravindra MP, Hales E, Orr S, Cherian C, Hou Z, Matherly LH and Gangjee A (2013) Discovery of 5-substituted pyrrolo[2,3-d]pyrimidine antifolates as dual acting inhibitors of glycinamide ribonucleotide formyltransferase and 5-aminoimidazole-4-carboxamide ribonucleotide formyltransferase in de novo purine nucleotide biosynthesis: implications of inhibiting 5-aminoimidazole-4-carboxamide ribonucleotide formyltransferase to AMPK activation and anti-tumor activity. *Journal of Medicinal Chemistry* **56**(24): 10016-10032.

Mitrovski B, Pressacco J, Mandelbaum S and Erlichman C (1994) Biochemical effects of folate-based inhibitors of thymidylate synthase in MGH-U1 cells. *Cancer chemotherapy and pharmacology* **35**(2): 109-114.

Morscher RJ, Ducker GS, Li SH, Mayer JA, Gitai Z, Sperl W and Rabinowitz JD (2018) Mitochondrial translation requires folate-dependent tRNA methylation. *Nature* **554**(7690): 128-132.

Mukherjee S (2010) *The emperor of all maladies: a biography of cancer*. Simon and Schuster.

Munch-Petersen B, Cloos L, Jensen HK and Tyrsted G (1995) Human thymidine kinase 1. Regulation in normal and malignant cells. *Advances in enzyme regulation* **35**: 69-89.

Murthy S and Reddy GP-V (2006) Replitase: Complete machinery for DNA synthesis. *Journal of Cellular Physiology* **209**(3): 711-717.

Myers CE, Young RC and Chabner BA (1975) Biochemical determinants of 5-fluorouracil response in vivo. The role of deoxyuridylate pool expansion. *Journal of Clinical Investigation* **56**(5): 1231-1238.

Naderi N and House JD (2018) Recent Developments in Folate Nutrition. *Advances in Food Nutrition Research* **83**: 195-213.

Nelson JA, Carpenter JW, Rose LM and Adamson DJ (1975) Mechanisms of action of 6-thioguanine, 6-mercaptopurine, and 8-azaguanine. *Cancer Research* **35**(10): 2872-2878.

Newman AC and Maddocks ODK (2017) One-carbon metabolism in cancer. *British Journal of Cancer* **116**(12): 1499-1504.

Nilsson R, Jain M, Madhusudhan N, Sheppard NG, Strittmatter L, Kampf C, Huang J, Asplund A and Mootha VK (2014) Metabolic enzyme expression highlights a key role for MTHFD2 and the mitochondrial folate pathway in cancer. *Nat Communications* **5**: 4128.

Ning S, Ma S, Saleh AQ, Guo L, Zhao Z and Chen Y (2018) SHMT2 Overexpression Predicts Poor Prognosis in Intrahepatic Cholangiocarcinoma. *Gastroenterology Research and Practice* **2018**: 4369253.

Noguchi K, Konno M, Koseki J, Nishida N, Kawamoto K, Yamada D, Asaoka T, Noda T, Wada H, Gotoh K, Sakai D, Kudo T, Satoh T, Eguchi H, Doki Y, Mori M and Ishii H (2018) The mitochondrial one-carbon metabolic pathway is associated with patient survival in pancreatic cancer. *Oncology letters* **16**(2): 1827-1834.

O'Connor OA, Amengual J, Colbourn D, Deng C and Sawas A (2017) Pralatrexate: a comprehensive update on pharmacology, clinical activity and strategies to optimize use. *Leukemia & lymphoma* **58**(11): 2548-2557.

O'Connor OA, Pro B, Pinter-Brown L, Bartlett N, Popplewell L, Coiffier B, Lechowicz MJ, Savage KJ, Shustov AR, Gisselbrecht C, Jacobsen E, Zinzani PL, Furman R, Goy A, Haioun C, Crump M, Zain JM, Hsi E, Boyd A and Horwitz S (2011) Pralatrexate in patients with relapsed or refractory peripheral T-cell lymphoma: results from the pivotal PROPEL study. *Journal of Clinical Oncology* **29**(9): 1182-1189.

Pazdur R (1997) Raltitrexed ('Tomudex') versus 5-fluorouracil and leucovorin (5-FU+ LV) in patients with advanced colorectal cancer (ACC): results of a randomized, multicenter North American trial, in *Proceedings of the American Society of Clinical Oncology* p 228a.

Pedley AM and Benkovic SJ (2017) A New View into the Regulation of Purine Metabolism: The Purinosome. *Trends in Biochemical Sciences* **42**(2): 141-154.

Pikman Y, Puissant A, Alexe G, Furman A, Chen LM, Frumm SM, Ross L, Fenouille N, Bassil CF, Lewis CA, Ramos A, Gould J, Stone RM, DeAngelo DJ, Galinsky I, Clish CB, Kung

AL, Hemann MT, Vander Heiden MG, Banerji V and Stegmaier K (2016) Targeting MTHFD2 in acute myeloid leukemia. *Journal of Experimental Medicine* **213**(7): 1285-1306.

Pizzorno G, Mini E, Coronnello M, McGuire JJ, Moroson BA, Cashmore AR, Dreyer RN, Lin JT, Mazzei T, Periti P and et al. (1988) Impaired polyglutamylation of methotrexate as a cause of resistance in CCRF-CEM cells after short-term, high-dose treatment with this drug. *Cancer Research* **48**(8): 2149-2155.

Possemato R, Marks KM, Shaul YD, Pacold ME, Kim D, Birsoy K, Sethumadhavan S, Woo HK, Jang HG, Jha AK, Chen WW, Barrett FG, Stransky N, Tsun ZY, Cowley GS, Barretina J, Kalaany NY, Hsu PP, Ottina K, Chan AM, Yuan B, Garraway LA, Root DE, Mino-Kenudson M, Brachtel EF, Driggers EM and Sabatini DM (2011) Functional genomics reveal that the serine synthesis pathway is essential in breast cancer. *Nature* **476**(7360): 346-350.

Prem veer Reddy G (1982) Catalytic function of thymidylate synthase is confined to S phase due to its association with replitase. *Biochemical and biophysical research communications* **109**(3): 908-915.

Qiu A, Jansen M, Sakaris A, Min SH, Chattopadhyay S, Tsai E, Sandoval C, Zhao R, Akabas MH and Goldman ID (2006) Identification of an intestinal folate transporter and the molecular basis for hereditary folate malabsorption. *Cell* **127**(5): 917-928.

Rabinowitz JD, Kim H, Ducker GS and Ghergurovich JM (2018) SHMT Inhibitors, Google Patents.

Racanelli AC, Rothbart SB, Heyer CL and Moran RG (2009) Therapeutics by cytotoxic metabolite accumulation: Pemetrexed causes ZMP accumulation, AMPK activation, and mTOR inhibition. *Cancer Research* **69**(13): 5467-5474.

Ratnam M, Marquardt H, Duhring JL and Freisheim JH (1989) Homologous membrane folate binding proteins in human placenta: cloning and sequence of a cDNA. *Biochemistry* **28**(20): 8249-8254.

Ravindra MP, Wilson MR, Tong N, O'Connor C, Karim MA, Polin L, Wallace-Povirk A, White K, Kushner J, Hou Z, Matherly LH and Gangjee A (2018) Fluorinated Substituted Pyrrolo[2,3-d]Pyrimidine Antifolates With Tumor-Targeting Via Cellular Uptake by Folate Receptor α and the Proton-coupled Folate Transporter and Inhibition of De Novo Purine Nucleotide Biosynthesis. *Journal of Medicinal Chemistry* **61**(9): 4228-4248.

Ray MS, Muggia FM, Leichman CG, Grunberg SM, Nelson RL, Dyke RW and Moran RG (1993) Phase I study of (6R)-5,10-dideazatetrahydrofolate: a folate antimetabolite inhibitory to de novo purine synthesis. *Journal of the National Cancer Institute* **85**(14): 1154-1159.

Raz S, Stark M and Assaraf YG (2016) Folylpoly-gamma-glutamate synthetase: A key determinant of folate homeostasis and antifolate resistance in cancer. *Drug Resistance Updates* **28**: 43-64.

Reddy JA, Haneline LS, Srour EF, Antony AC, Clapp DW and Low PS (1999) Expression and functional characterization of the β-isoform of the folate receptor on CD34+ cells. *Blood* **93**(11): 3940-3948.

Renwick SB, Snell K and Baumann U (1998) The crystal structure of human cytosolic serine hydroxymethyltransferase: a target for cancer chemotherapy. *Structure (London, England : 1993)* **6**(9): 1105-1116.

Rich MA, Bolaffi JL, Knoll JE, Cheong L and Eidinoff ML (1958) Growth inhibition of a human tumor cell strain by 5-fluorouracil, 5-fluorouridine, and 5-fluoro-2'-deoxyuridine; reversal studies. *Cancer Research* **18**(6): 730-735.

Rosowsky A (1999) PT523 and other aminopterin analogs with a hemiphthaloyl-L-ornithine side chain: exceptionally tight-binding inhibitors of dihydrofolate reductase which are transported by the reduced folate carrier but cannot form polyglutamates. *Current medicinal chemistry* **6**(4): 329-352.

Rosowsky A, Bader H, Wright JE, Keyomarsi K and Matherly LH (1994) Synthesis and biological activity of N omega-hemiphthaloyl-alpha,omega- diaminoalkanoic acid analogues of aminopterin and 3',5-dichloroaminopterin. *Journal of Medicinal Chemistry* **37**(14): 2167-2174.

Rossi ML, Rehman AA and Gondi CS (2014) Therapeutic options for the management of pancreatic cancer. *World Journal of Gastroenterology* **20**(32): 11142-11159.

Rothbart SB, Racanelli AC and Moran RG (2010) Pemetrexed indirectly activates the metabolic kinase AMPK in human carcinomas. *Cancer Research* **70**(24): 10299-10309.

Sato S and Itamochi H (2016) Profile of farletuzumab and its potential in the treatment of solid tumors. *OncoTargets and Therapy* **9**: 1181-1188.

Schimke RT (1988) Gene amplification in cultured cells. *Journal of Biological Chemistry* **263**(13): 5989-5992.

Schmidt A, Wu H, MacKenzie RE, Chen VJ, Bewly JR, Ray JE, Toth JE and Cygler M (2000) Structures of three inhibitor complexes provide insight into the reaction mechanism of the human methylenetetrahydrofolate dehydrogenase/cyclohydrolase. *Biochemistry* **39**(21): 6325-6335.

Scotti M, Stella L, Shearer EJ and Stover PJ (2013) Modeling cellular compartmentation in one-carbon metabolism. *Wiley Interdisciplinary Reviews: Systems Biology and Medicine* **5**(3): 343-365.

Senft AP, Dalton TP and Shertzer HG (2000) Determining glutathione and glutathione disulfide using the fluorescence probe o-phthalaldehyde. *Analytical Biochemistry* **280**(1): 80-86.

Sessa C, de Jong J, D'Incalci M, Hatty S, Pagani O and Cavalli F (1996) Phase I study of the antipurine antifolate lometrexol (DDATHF) with folinic acid rescue. *Clinical Cancer Research* **2**(7): 1123-1127.

Shane B (1989) Folylpolyglutamate synthesis and role in the regulation of one-carbon metabolism. *Vitamins and hormones* **45**: 263-335.

Shih C, Chen VJ, Gossett LS, Gates SB, MacKellar WC, Habeck LL, Shackelford KA, Mendelsohn LG, Soose DJ, Patel VF, Andis SL, Bewley JR, Rayl EA, Moroson BA, Beardsley GP, Kohler W, Ratnam M and Schultz RM (1997) LY231514, a Pyrrolo[2,3-d]pyrimidine-based Antifolate That Inhibits Multiple Folate-requiring Enzymes. *Cancer Research* **57**(6): 1116-1123.

Shimizu T, Nakagawa Y, Takahashi N and Hashimoto S (2016) Thymidylate synthase gene amplification predicts pemetrexed resistance in patients with advanced non-small cell lung cancer. *Clinical Translational Oncology* **18**(1): 107-112.

Shin M, Bryant JD, Momb J and Appling DR (2014) Mitochondrial MTHFD2L is a dual redox cofactor-specific methylenetetrahydrofolate dehydrogenase/methenyltetrahydrofolate cyclohydrolase expressed in both adult and embryonic tissues. *Journal of Biological Chemistry* **289**(22): 15507-15517.

Shin M, Momb J and Appling DR (2017) Human mitochondrial MTHFD2 is a dual redox cofactor-specific methylenetetrahydrofolate dehydrogenase/methenyltetrahydrofolate cyclohydrolase. *Cancer Metabolism* **5**(11).

Sierra EE, Brigle KE, Spinella MJ and Goldman ID (1997) pH dependence of methotrexate transport by the reduced folate carrier and the folate receptor in L1210 leukemia cells. Further evidence for a third route mediated at low pH. *Biochemical Pharmacology* **53**(2): 223-231.

Sirotnak FM and Tolner B (1999) CARRIER-MEDIATED MEMBRANE TRANSPORT OF FOLATES IN MAMMALIAN CELLS. *Annu Rev Nutr* **19**(1): 91-122.

Stork LC, Matloub Y, Broxson E, La M, Yanofsky R, Sather H, Hutchinson R, Heerema NA, Sorrell AD, Masterson M, Bleyer A and Gaynon PS (2010) Oral 6-mercaptopurine versus oral 6-thioguanine and veno-occlusive disease in children with standard-risk acute lymphoblastic leukemia: report of the Children's Oncology Group CCG-1952 clinical trial. *Blood* **115**(14): 2740-2748.

Stubbs M, McSheehy PMJ, Griffiths JR and Bashford CL (2000) Causes and consequences of tumour acidity and implications for treatment. *Molecular Medicine Today* **6**(1): 15-19.

Tedeschi PM, Scotto KW, Kerrigan J and Bertino JR (2016) MTHFD2- a new twist? *Oncotarget* **7**(7): 7368-7369.

Tedeschi PM, Vazquez A, Kerrigan JE and Bertino JR (2015) Mitochondrial Methylene Tetrahydrofolate Dehydrogenase (MTHFD2) Overexpression is Associated with Tumor Cell Proliferation and is a Novel Target for Drug Development. *Molecular Cancer Research* **13**(10): 1361-1366.

Thirion P, Michiels S, Pignon JP, Buyse M, Braud AC, Carlson RW, O'Connell M, Sargent P and Piedbois P (2004) Modulation of fluorouracil by leucovorin in patients with advanced colorectal cancer: an updated meta-analysis. *Journal of Clinical Oncology* **22**(18): 3766-3775.

Tibbetts AS and Appling DR (2010) Compartmentalization of Mammalian folate-mediated one-carbon metabolism. *Annu Rev Nutr* **30**: 57-81.

Titus SA and Moran RG (2000) Retrovirally mediated complementation of the glyB phenotype. Cloning of a human gene encoding the carrier for entry of folates into mitochondria. *Journal of Biological Chemistry* **275**(47): 36811-36817.

Touroutoglou N and Pazdur R (1996) Thymidylate synthase inhibitors. *Clinical Cancer Research* **2**(2): 227-243.

Tse A, Brigle K, Taylor SM and Moran RG (1998) Mutations in the reduced folate carrier gene which confer dominant resistance to 5,10-dideazatetrahydrofolate. *Journal of Biological Chemistry* **273**(40): 25953-25960.

Tse A and Moran RG (1998) Cellular Folates Prevent Polyglutamation of 5,10-Dideazatetrahydrofolate: A NOVEL MECHANISM OF RESISTANCE TO FOLATE ANTIMETABOLITES. *Journal of Biological Chemistry* **273**(40): 25944-25952.

Tucker EJ, Hershman SG, Kohrer C, Belcher-Timme CA, Patel J, Goldberger OA, Christodoulou J, Silberstein JM, McKenzie M, Ryan MT, Compton AG, Jaffe JD, Carr

SA, Calvo SE, RajBhandary UL, Thorburn DR and Mootha VK (2011) Mutations in MTFMT underlie a human disorder of formylation causing impaired mitochondrial translation. *Cell Metabolism* **14**(3): 428-434.

Varela-Moreiras G and Selhub J (1992) Long-term folate deficiency alters folate content and distribution differentially in rat tissues. *Journal of Nutrition* **122**(4): 986-991.

Vergote I and Leamon CP (2015) Vintafolide: a novel targeted therapy for the treatment of folate receptor expressing tumors. *Therapeutic Advances in Clinical Oncology* **7**(4): 206-218.

Visentin M, Unal ES, Zhao R and Goldman ID (2013) The membrane transport and polyglutamation of pralatrexate: a new-generation dihydrofolate reductase inhibitor. *Cancer chemotherapy and pharmacology* **72**(3): 597-606.

Visentin M, Zhao R and Goldman ID (2012) The Antifolates. *Hematology/oncology clinics of North America* **26**(3): 629-648.

Walko CM and Lindley C (2005) Capecitabine: a review. *Clinical therapeutics* **27**(1): 23-44.

Wall M, Shim JH and Benkovic SJ (2000) Human AICAR transformylase: role of the 4-carboxamide of AICAR in binding and catalysis. *Biochemistry* **39**(37): 11303-11311.

Wang L, Cherian C, Desmoulin SK, Polin L, Deng Y, Wu J, Hou Z, White K, Kushner J, Matherly LH and Gangjee A (2010) Synthesis and antitumor activity of a novel series of 6-substituted pyrrolo[2,3-d]pyrimidine thienoyl antifolate inhibitors of purine biosynthesis with selectivity for high affinity folate receptors and the proton-coupled folate transporter over the reduced folate carrier for cellular entry. *Journal of Medicinal Chemistry* **53**(3): 1306-1318.

Wang L, Cherian C, Kugel Desmoulin S, Mitchell-Ryan S, Hou Z, Matherly LH and Gangjee A (2012) Synthesis and biological activity of 6-substituted pyrrolo[2,3-d]pyrimidine

thienoyl regioisomers as inhibitors of de novo purine biosynthesis with selectivity for cellular uptake by high affinity folate receptors and the proton-coupled folate transporter over the reduced folate carrier. *Journal of Medicinal Chemistry* **55**(4): 1758-1770.

Wang L, Desmoulin SK, Cherian C, Polin L, White K, Kushner J, Fulterer A, Chang M-H, Mitchell S, Stout M, Romero MF, Hou Z, Matherly LH and Gangjee A (2011) Synthesis, biological and antitumor activity of a highly potent 6-substituted pyrrolo[2,3-d]pyrimidine thienoyl antifolate inhibitor with proton-coupled folate transporter and folate receptor selectivity over the reduced folate carrier that inhibits β-glycinamide ribonucleotide formyltransferase. *Journal of Medicinal Chemistry* **54**(20): 7150-7164.

Wang L, Wallace A, Raghavan S, Deis SM, Wilson MR, Yang S, Polin L, White K, Kushner J, Orr S, George C, O'Connor C, Hou Z, Mitchell-Ryan S, Dann CE, 3rd, Matherly LH and Gangjee A (2015) 6-Substituted Pyrrolo[2,3-d]pyrimidine Thienoyl Regioisomers as Targeted Antifolates for Folate Receptor alpha and the Proton-Coupled Folate Transporter in Human Tumors. *Journal of Medicinal Chemistry* **58**(17): 6938-6959.

Wang N and McCammon JA (2016) Substrate channeling between the human dihydrofolate reductase and thymidylate synthase. *Protein Science* **25**(1): 79-86.

Wang TT, Chandler CJ and Halsted CH (1986) Intracellular pteroylpolyglutamate hydrolase from human jejunal mucosa. Isolation and characterization. *Journal of Biological Chemistry* **261**(29): 13551-13555.

Wang Y, Cherian C, Orr S, Mitchell-Ryan S, Hou Z, Raghavan S, Matherly LH and Gangjee A (2013) Tumor-Targeting with Novel Non-Benzoyl 6-Substituted Straight Chain Pyrrolo[2,3-d]pyrimidine Antifolates via Cellular Uptake by Folate Receptor α and

Inhibition of de novo Purine Nucleotide Biosynthesis. *Journal of medicinal Chemistry* **56**(21): 10.1021/jm401139z.

Webb BA, Chimenti M, Jacobson MP and Barber DL (2011) Dysregulated pH: a perfect storm for cancer progression. *Nature Reviews Cancer* **11**(9): 671-677.

Weitman SD, Weinberg AG, Coney LR, Zurawski VR, Jennings DS and Kamen BA (1992) Cellular Localization of the Folate Receptor: Potential Role in Drug Toxicity and Folate Homeostasis. *Cancer Research* **52**(23): 6708-6711.

Wilson MR, Hou Z, Yang S, Polin L, Kushner J, White K, Huang J, Ratnam M, Gangjee A and Matherly LH (2016) Targeting Nonsquamous Nonsmall Cell Lung Cancer via the Proton-Coupled Folate Transporter with 6-Substituted Pyrrolo[2,3-d]Pyrimidine Thienoyl Antifolates. *Molecular Pharmacology* **89**(4): 425-434.

Witschel M, Stelzer F, Hutzler J, Qu T, Mietzner T, Kreuz K, Grossmann K, Aponte R, Hoeffken HW, Calo F, Ehrhardt T, Simon A and Parra Rapado L (2013) Pyrazolopyrans having herbicidal and pharmaceutical properties, Basf Se.

Witschel MC, Rottmann M, Schwab A, Leartsakulpanich U, Chitnumsub P, Seet M, Tonazzi S, Schwertz G, Stelzer F, Mietzner T, McNamara C, Thater F, Freymond C, Jaruwat A, Pinthong C, Riangrungroj P, Oufir M, Hamburger M, Maser P, Sanz-Alonso LM, Charman S, Wittlin S, Yuthavong Y, Chaiyen P and Diederich F (2015) Inhibitors of plasmodial serine hydroxymethyltransferase (SHMT): cocrystal structures of pyrazolopyrans with potent blood- and liver-stage activities. *J Med Chem* **58**(7): 3117-3130.

Wong SC, Proefke SA, Bhushan A and Matherly LH (1995) Isolation of human cDNAs that restore methotrexate sensitivity and reduced folate carrier activity in methotrexate

transport-defective Chinese hamster ovary cells. *Journal of Biological Chemistry* **270**(29): 17468-17475.

Wu M, Wanggou S, Li X, Liu Q and Xie Y (2017) Overexpression of mitochondrial serine hydroxyl-methyltransferase 2 is associated with poor prognosis and promotes cell proliferation and invasion in gliomas. *OncoTargets and Therapy* **10**: 3781-3788.

Wykoff CC, Beasley NJ, Watson PH, Turner KJ, Pastorek J, Sibtain A, Wilson GD, Turley H, Talks KL, Maxwell PH, Pugh CW, Ratcliffe PJ and Harris AL (2000) Hypoxia-inducible expression of tumor-associated carbonic anhydrases. *Cancer Research* **60**(24): 7075-7083.

Xing R, Zhang H, Yuan J, Zhang K, Li L, Guo H, Zhao L, Zhang C, Li S, Gao T, Liu Y and Wang L (2017) Novel 6-substituted benzoyl and non-benzoyl straight chain pyrrolo[2,3-d]pyrimidines as potential antitumor agents with multitargeted inhibition of TS, GARFTase and AICARFTase. *European Journal of Medicinal Chemistry* **139**(Supplement C): 531-541.

Yang M and Vousden KH (2016) Serine and one-carbon metabolism in cancer. *Nature Reviews Cancer* **16**(10): 650-662.

Ye J, Fan J, Venneti S, Wan YW, Pawel BR, Zhang J, Finley LW, Lu C, Lindsten T, Cross JR, Qing G, Liu Z, Simon MC, Rabinowitz JD and Thompson CB (2014) Serine catabolism regulates mitochondrial redox control during hypoxia. *Cancer discovery* **4**(12): 1406-1417.

Yin K (2015) Positive correlation between expression level of mitochondrial serine hydroxymethyltransferase and breast cancer grade. *OncoTargets and Therapy* **8**: 1069-1074.

Yoshioka A, Tanaka S, Hiraoka O, Koyama Y, Hirota Y, Ayusawa D, Seno T, Garrett C and Wataya Y (1987) Deoxyribonucleoside triphosphate imbalance. 5-Fluorodeoxyuridine-induced DNA double strand breaks in mouse FM3A cells and the mechanism of cell death. *Journal of Biological Chemistry* **262**(17): 8235-8241.

Zhang D, Ochi N, Takigawa N, Tanimoto Y, Chen Y, Ichihara E, Hotta K, Tabata M, Tanimoto M and Kiura K (2011) Establishment of pemetrexed-resistant non-small cell lung cancer cell lines. *Cancer Letters* **309**(2): 228-235.

Zhang L, Chen Z, Xue D, Zhang Q, Liu X, Luh F, Hong L, Zhang H, Pan F, Liu Y, Chu P, Zheng S, Lou G and Yen Y (2016) Prognostic and therapeutic value of mitochondrial serine hydroxyl-methyltransferase 2 as a breast cancer biomarker. *Oncology reports* **36**(5): 2489-2500.

Zhao R (2009) A Role for the Proton-coupled Folate Transporter (PCFT-SLC46A1) in Folate. **284**(7): 4267-4274.

Zhao R and Goldman ID (2003) Resistance to antifolates. *Oncogene* **22**(47): 7431-7457.

Zhao R and Goldman ID (2007) The molecular identity and characterization of a Proton-coupled Folate Transporter--PCFT; biological ramifications and impact on the activity of pemetrexed. *Cancer and Metastasis Reviews* **26**(1): 129-139.

Zhao R, Matherly LH and Goldman ID (2009) Membrane transporters and folate homeostasis: intestinal absorption and transport into systemic compartments and tissues. *Expert reviews in molecular medicine* **11**: e4.

Zhao R, Min SH, Qiu A, Sakaris A, Goldberg GL, Sandoval C, Malatack JJ, Rosenblatt DS and Goldman ID (2007) The spectrum of mutations in the PCFT gene, coding for an intestinal

folate transporter, that are the basis for hereditary folate malabsorption. *Blood* **110**(4): 1147-1152.

Zhao R, Qiu A, Tsai E, Jansen M, Akabas MH and Goldman ID (2008) The proton-coupled folate transporter: impact on pemetrexed transport and on antifolates activities compared with the reduced folate carrier. *Molecular Pharmacology* **74**(3): 854-862.

Zhao R, Russell RG, Wang Y, Liu L, Gao F, Kneitz B, Edelmann W and Goldman ID (2001) Rescue of embryonic lethality in reduced folate carrier-deficient mice by maternal folic acid supplementation reveals early neonatal failure of hematopoietic organs. *Journal of Biological Chemistry* **276**(13): 10224-10228.

Zhao RD-B, Ndeye; Visentin, Michele; Goldman, David I. (2011) Mechanisms of Membrane Transport of Folates into Cells and Across Epithelia. *Annu Rev Nutr* **31**(1): 177-201.

Zheng Y, Lin TY, Lee G, Paddock MN, Momb J, Cheng Z, Li Q, Fei DL, Stein BD, Ramsamooj S, Zhang G, Blenis J and Cantley LC (2018) Mitochondrial One-Carbon Pathway Supports Cytosolic Folate Integrity in Cancer Cells. *Cell* **175**(6): 1546-1560.e1517.

ABSTRACT

THERAPEUTIC DUAL-TARGETING OF CYTOSOLIC AND MITOCHONDRIAL ONE-CARBON METABOLISM

by

AAMOD SANJEEV DEKHNE

August 2019

Advisor: Dr. Larry H. Matherly

Major: Cancer Biology

Degree: Doctor of Philosophy

One-carbon metabolism (1CM) is compartmentalized in the mitochondria and cytosol and generates a host of metabolites critical to tumor propagation. Although drug-targeting of cytosolic 1CM remains a clinically-relevant mainstay, development of clinically-useful agents targeting mitochondrial 1CM remains elusive. Of particular pharmacological interest is the mitochondrial 1CM enzyme, serine hydroxymethyltransferase2 (SHMT2). SHMT2 expression correlates with the oncogenic phenotype in lung, colon, breast, glioma, and liver cancer and, overall, is the fifth-most differentially expressed metabolic enzyme in cancer cell versus normal tissue. Despite the unequivocal oncogenic importance and therapeutic potential of SHMT2, *there are no clinically relevant (i.e. active* in vivo*) inhibitors of this enzyme*.

In this dissertation work, we sought to design, synthesize, and characterize pharmacodynamics of our 5-substituted pyrrolo[3,2-*d*]pyrimidine antifolates synergistically dual-targeting mitochondrial SHMT2 and cytosolic 1CM, the latter specifically at the purine nucleotide biosynthesis enzymes glycinamide ribonucleotide formyltransferase (GARFTase) and/or 5-aminoimidazole-4-carboxamide ribonucleotide formyltransferase (AICARFTase). By depleting SHMT2-derived formate, these compounds potentiated their own inhibition of the

downstream formate-dependent GARFTase and AICARFTase. We generated these compounds (**AGF291, AGF320,** and **AGF347**) by melding structures of SHMT2 cofactor 5,10-methylene tetrahydrofolate with our previously reported purine inhibitors and confirmed enzyme targets with *in vitro* targeted metabolomics in H460 (large cell lung carcinoma), HCT-116 (colorectal carcinoma), and MIA PaCa-2 (pancreatic ductal adenocarcinoma) human tumor cell lines as well as *in vitro* cell-free assays. Transport assays revealed significant uptake by both the proton-coupled folate transporter (narrow physiological niche, but commonly expressed in many solid tumors) and the reduced folate carrier (major tissue folate transporter). Subcellular fractionation of MIA PaCa-2 and GlyB Chinese hamster ovary cells revealed **AGF347** to be heavily (>98%) polyglutamylated in both cytosol and mitochondria with mitochondrial uptake partially mediated by the mitochondrial folate transporter. Intracellular glycine depletion secondary to SHMT2 inhibition by all compounds also depleted cellular ROS scavenging capacity as reflected in decreased GSH/GSSG ratio. *In vivo*, **AGF347** demonstrated potent antitumor efficacy against MIA PaCa-2 xenografts in SCID mice with tumor growth delay (T-C) of 61 days *and one out of five treated mice tumor-free 120+ days after treatment. In vivo* metabolomics on these xenografts confirmed inhibition of purine biosynthesis. Collectively, the work in this dissertation establishes the exceptional therapeutic potential of dual-targeting mitochondrial and cytosolic 1CM.

AUTOBIOGRAPHICAL STATEMENT

EDUCATION

The University of Michigan, Ann Arbor 2010-2014

Honors Bachelor of Science: Biophysics

GRANTS

T32 Training Grant- National Institute of Health (NIH) 2017-2018

F30 Predoctoral Training Grant F30-CA228221 2018-2021